Master thesis in experimental nuclear physics

Automated XY-table for the characterisation of arrays of pixel sensors for photons and charge particles

by

Andreas Tefre Samnøy

Department of Physics and Technology
University of Bergen
June 2010

Acknowledgments

First of all I would like to thank my supervisor professor Dieter Röhrich for the opportunity to work with an interesting thesis. Thank you for all the help received and the interesting discussions.

I would also like to give many thanks to Njål Brekke, Dominik Fehlker and Hege Erdal for all the help received, I do not know how I would have done this without your help.

I would like to give a very special thanks to Sigrid for all the support you have given me, you have made all the hard times much easier.

Thanks to all my friends who are always there when I need you, and those of you who helped to correct my thesis.

At last I would like to thank my family who has always been there for me, and has encouraged me to study.

Summary

A variety of arrays of pixels sensors (pixel = picture elements) have been developed during the last 30 years for the detection of photons and charge particles. Pixel based semiconductor detectors are not only used for sensing position. The new pixel based Geiger mode APDs (G-APDs) are created to measure light intensities, or even to count single photons. There are several different G-APD designs with minor differences. The hope is that some of these new designs will replace the Photo Multiplier Tube (PMT) and the Avalanche PhotoDiode (APD) for reading out scintillation crystals. The properties of the G-APDs are still being tested, but the prospects look promising.

The motivation for this thesis was to build a setup that could test the response of a single G-APD pixel as part of an overall work to characterise G-APDs. Last year Hege A. Erdal delivered her master thesis (1) where she has characterised two types of G-APDs and Ph.d. student Njål Brekke is looking into Time of Flight (ToF) Positron Emission Tomography (PET) by the use of G-APDs. Even though the current focus is on G-APDs, any setup capable of testing single pixels should also be able to test position detectors in the future with some alteration.

The setup is based on an XY-table from the particle physics group at IFT. The XY-table mainly consists of three microstepper stages that can move a detector in all three dimensions with a microscope above for inspection. An automated system that can trigger every pixel on a G-APD has been implemented.

After developing programs to locate single pixels on G-APDs it was noticed that the microstepper stages were flawed and moved incorrectly. The microstepper stages of the XY-table have been characterised by the use of a fine calibration grid, and their fault has been quantified. After several failures to correct for this in software a program which uses pattern matching was successfully implemented. This has been the most time consuming part of the thesis.

In order to trigger single pixels without triggering neighbouring pixels, they must be struck by a narrow, fast light pulse. The pixels are triggered by focusing light pulses from a LED through the microscope. This has proven to be an effective way of triggering pixels.

The reproduceability of this setup has been tested by comparing several series of measurements of the same G-APD. Between each series, parts have been dismantled and then reassembled again. These tests has shown that the setup's reproducibility is within the specification when determining e.g. the gain of the G-APD.

Two types of MPPCs have been tested: The first measurements of the response of the MPPC indicate that there are no dead pixels, one of the detectors have a uniform gain across the pixels, while the other show a distinct gain pattern across the pixels.

Contents

List of Figures

Chapter 1

Introduction

A variety of arrays of pixels sensors (pixel = picture elements) have been developed during the last 30 years for the detection of photons and charge particles. Pixels can have dimensions down to 5×5 μm, and an array can contain several million sensors. There are several reasons for building particle detectors. Different kinds of detectors are used in health and industry, such as the positron emission tomography (PET), gamma densitometer, and even modern digital cameras. Most of these result from particle and nuclear physics experiments that endeavour to give us a better understanding of the universe.

The goal of this thesis was to build a system that could test single pixels in pixel based detectors, both for position sensing (vertex detectors), and for reading scintillation light for energy measurements (calorimeters). The system has been used to characterise pixel Geiger-mode Avalanche Photo-Diodes (G-APDs), which are used for reading out scintillation light. The G-APDs are an important part of the current activities at the detector laboratory at the department of physics and technology (IFT). Both pixel vertex detectors and G-APDs will be presented in chapter 3.

To better understand the principles of the different detectors it is important to have an understanding of how photons and particles interact with matter. It is also important to understand the properties of the materials that are used for particle detection. The detectors described in this thesis are based on semiconductors, more specifically, they are based on silicon. An introduction to semiconductors and their radiation detection properties are given in chapter 2.

This chapter gives a brief introduction to how energetic particles interact with matter.
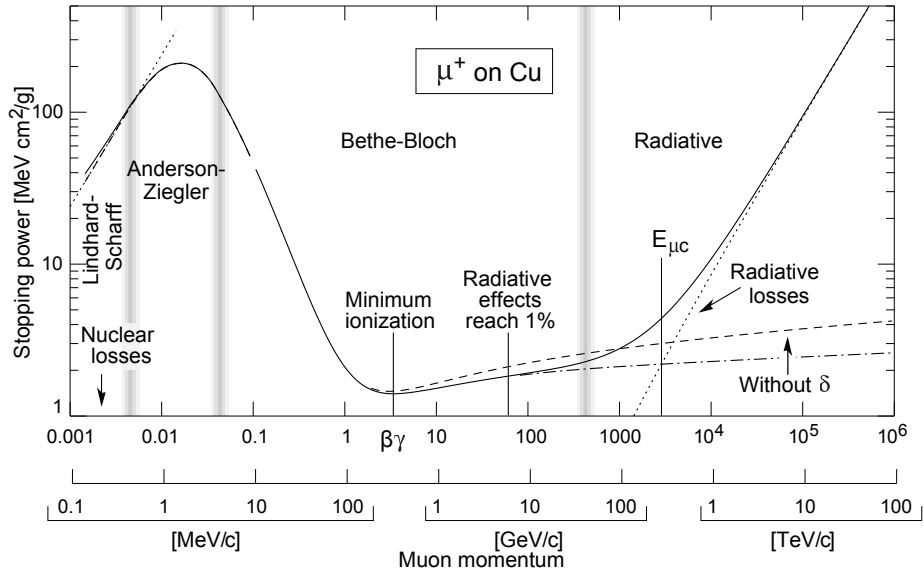
Figure 1.1: The Bethe-Bloch curve for muons in copper. The figure is taken from (3).

1.1 Interaction of charged particles with matter

When a charged particle hits matter it will lose its energy through different processes. We do however split the charged particles into two groups with respect to their energy loss; heavy particles and light particles. By heavy particles one refers to particles with large mass than electrons, like muons and protons. The different ways charged particles interact with matter (2):

1. Inelastic collision with the atomic electrons

2. Elastic collision with nuclei

3. Inelastic collision with nuclei (nuclear reaction)

4. Cherenkov radiation

5. Bremsstrahlung

1.1.1 Heavy particles

When a heavy particle enters matter the main energy loss process is inelastic collision with the atomic bound electrons in the matter, causing the atoms to be ionized. An incoming particle will mostly feel the electrons' Coulomb field, which leads to an inelastic collision with the atom's electrons. The mass and the binding energy of the atomic bound electrons will however be too small to actually deflect it in any extent that matters. The only way

to deflect the incoming particle is through an interaction with the atom's nuclei since their weight is about the same order of magnitude. The incoming particle can be deflected by the nucleus though an elastic collision, but an inelastic collision will seldom occur. The mean energy loss by ionization for a heavy particle with the velocity $v = c\beta$, where c is the velocity of light, per distance x is calculated by the Bethe-Block formula (2):

$$-\frac{dE}{dx} = 4\pi N_0 r_e^2 m_e c^2 z^2 \rho \frac{Z}{A} \frac{1}{\beta^2} \left[\frac{1}{2} ln \left(2m_e c^2 \beta^2 \gamma^2 \frac{T_{max}}{I^2} \right) - \beta^2 - \frac{\delta(\beta\gamma)}{2} - \frac{C}{Z} \right],$$
$$(1.1)$$

where,

- m_e is the electron mass

- r_e is the classical electron radius

- z is the charge of the incident particle in units of electron charge, q_e

- Z is the number of protons in the nuclei

- A is the atomic mass in units of g/mol

- N_0 is Avogadro's number

- δ is the density correction, which is important for high energies and dense material

- C is the shell correction, which is important at low energies

- T_{max} is the maximum energy transferal of a single collision

- I is the mean excitation potential for the material

- γ is the Lorentz factor

The maximum energy transferal in a single collision, T_{max}, occurs in a head-on collision is given by (2),

$$T_{max} = \frac{2m_e c^2 \beta^2 \gamma^2}{1 + \frac{m_e}{m} \sqrt{1 + \beta^2 \gamma^2} + \frac{m_e}{m}},$$
$$(1.2)$$

where m is the mass of the incoming particle.

1.1.2 Light particles: electrons and positrons

Since electrons and positrons are very light particles they will easily deflect in an electric field. When a charged particle is deflected it will radiate photons, this is called bremsstrahlung (3; 4; 2). The amount of energy a charged particle will radiate depends on the curvature of it's trajectory and
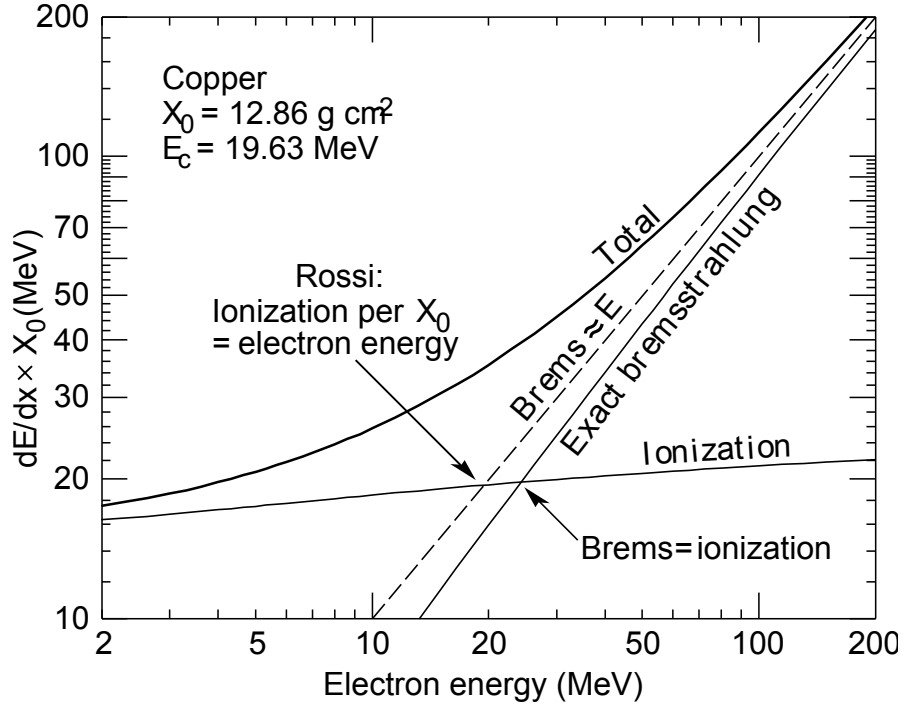
Figure 1.2: Energy loss from both ionization and bremsstrahlung. Critical energy, E_c is at the point where the energy loss from ionization is equal to bremsstrahlung. The figure is taken from (3).

the momentum of the particle. Since the radius depends on the mass of the particle, the energy loss due to bremsstrahlung is dependent on the mass and the kinetic energy of the particle.

Electrons and positrons will also ionize atoms when they pass through matter. This is the main contribution to energy loss at small and mid ranged energies. The energy loss of electrons and positrons can therefore be split into two parts; one for ionization and one for bremsstrahlung:

$$\left(\frac{dE}{dx}\right)_{tot} = \left(\frac{dE}{dx}\right)_{brems} + \left(\frac{dE}{dx}\right)_{ion}. \tag{1.3}$$

The point where the energy loss from ionization equals the loss from bremsstrahlung is called the critical energy, E_c. From figure 1.2 it can be seen that due to the fast rising bremsstrahlung loss curve the bremsstrahlung will dominate completely above the critical energy, and ionization will dominate below.

The ionization formula for electrons is a modified Bethe-Bloch formula than the one for heavy ions. This is because one has to take into account that the electron mass is small and will be deflected after a collision with maximum energy transferred $T_{max} = T_e/2$. Since the electrons are identical, the two electrons colliding will be indistinguishable from each other. It will

therefore be impossible to tell which of the electrons were the incident one. Taking this into account the Bethe-Block formula for electrons and positrons are (2):

$$-\left(\frac{dE}{dx}\right)_{ion} = 2\pi N_0 r_e^2 m_e c^2 \rho \frac{Z}{A} \frac{1}{\beta^2} \left[ln \frac{\tau^2(\tau+2)}{2(I/m_e c^2)^2} + F(\tau) - \delta - 2\frac{C}{Z} \right],$$
(1.4)

where τ is the kinetic energy of the electron in units of $m_e c^2$.
For electrons,

$$F(\tau) = 1 - \beta^2 + \frac{\frac{\tau^2}{8} - (2r+1)ln2}{(\tau+1)^2},$$
(1.5)

for positrons,

$$F(\tau) = 2ln2 - \frac{\beta^2}{12}\left(23 + \frac{14}{\tau+2} + \frac{10}{(\tau+2)^2} + \frac{4}{(\tau+2)^3}\right).$$
(1.6)

The energy loss from bremsstrahlung is given by a unit called the *radiation length*, X_0. The radiation length is defined as the length it takes an electron to lose all but $1/e$ of its energy to brehmsstrahlung, and is predominantly dependant on the material. The radiation length is given as (3):

$$\frac{1}{X_0} = 4\alpha r_e^2 \frac{N_0}{A} \left[Z^2(L - f(Z)) + ZL' \right],$$
(1.7)

where $\alpha = 1/137$ is the fine-structure constant and $f(Z)$ is a correction of the Born approximation (2; 3):

$$f(Z) \simeq a^2[(1+a^2)^{-1} + 0.020206 - 0.0369a^2 + 0.0083a^4 - 0.002a^6], \quad (1.8)$$

where $a = Z/137$.
L_{rad} and L'_{rad} is given as (3),

$$L_{rad} = ln(184.15Z^{-1/3}) \qquad\qquad L'_{rad} = ln(1194Z^{-2/3}), \qquad (1.9)$$

for elements with $Z > 4$.

A good approximation of the radiation length, which shows its material dependence, is (2):

$$X_0 = \frac{716.4g/cm^2 A}{Z(Z+1)ln(287/\sqrt{Z})},$$
(1.10)

where Z is the atomic number and A is the weight of the material. Finally, the energy loss due to radiation is approximately given as (3):

$$\left(\frac{dE}{dx}\right)_{brems} \approx \frac{E}{X_0}$$
(1.11)
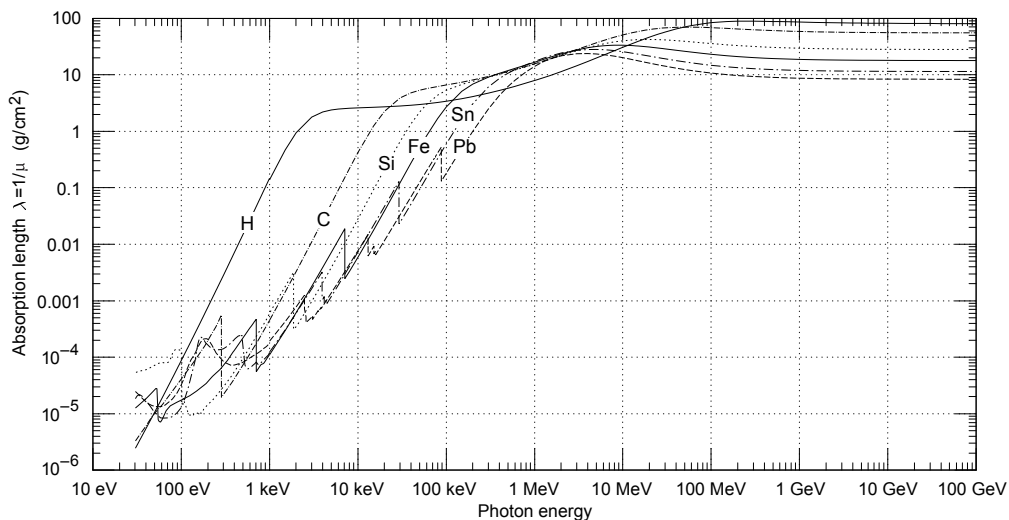
Figure 1.3: The absorption length λ for different materials at different energies. The absorption length is the inverse of the absorption coefficient, $\lambda = 1/\mu$. The figure is taken from (3).

As mentioned earlier the critical energy is given when $\left(\frac{dE}{dx}\right)_{ion} = \left(\frac{dE}{dx}\right)_{brems}$. The critical energy is also heavily dependant on the atomic number, shown by the approximation (2):

$$E_c \simeq \frac{800\text{MeV}}{Z + 1.2}. \tag{1.12}$$

1.2   Interaction of photon with matter

Photons do not lose energy in the same manner as charged particles. Since they have no charge their interaction cross section will be much smaller. When a beam of photons traverses a material approximately all of the photons coming through will have the same energy as they had when they entered, but the intensity of the beam will be weakened. The reason for this is that the most probable result when a photon interacts with matter is that the photon will vanish. The photon can also lose some of its energy through scattering, but since lower photon energy generally leads to a larger cross section, the scattered photon will most likely vanish as well. The mechanisms behind photon interaction are explained in the following sections.

The intensity of a photon beam I after passing through a material of thickness x is (2):

$$I(x) = I_0 e^{-\mu x}, \tag{1.13}$$

where I_0 is the intensity before entering the material, and μ is the absorption

coefficient. The absorption coefficient is made up by the interaction cross section of the photons and the material it traverses, and is therefore both material and energy dependant. The absorption length is the inverse of the absorption coefficient, and is often used in literature concerning the matter. The absorption length is shown in figure 1.3 as a function of energy for several materials. The formula for the absorption coefficient:

$$\mu = \sigma \left(\frac{N_0 \rho}{A} \right), \tag{1.14}$$

where N_0 is Avogadro's number, ρ is the density of the material and A is the molecular weight. The total cross section σ can be split into several parts, where each part represent the cross section of one distinct energy loss process. The three main energy loss processes a photon goes through are the following:

1. Photoelectric effect

2. Compton Scattering

3. Pair production

Their cross sectional dependency on energy is shown in figure 1.4

1.2.1 Photoelectric effect

Photoelectric effect is when the photon is absorbed by an atomic bound electron. If the photon energy, E_γ, is higher than the binding energy, B, the electron will be free with the energy

$$E = E_\gamma - B. \tag{1.15}$$

Because of momentum conservation, a free electron can not absorb a photon since nothing can receive the recoil momentum. When the electron is bound in an atom the nucleus receives the recoil momentum. Figure 1.4 shows that the cross section, $\sigma_{p.e.}$, will decrease with increasing energy, with the exception of a few edges at the beginning of the curve. These edges coincides with the binding energy of different shells in the atom. A photon is therefore more likely to be absorbed if its energy resonate with the binding energy of one of the atomic shells. A single mathematical equation for the photoelectric effect cross section is hard to derive, but according to (5) an approximation of the cross section after the K shell is given as:

$$\sigma_{ph} = \frac{32\pi}{3}\sqrt{2}Z^5\alpha^4\frac{1}{\epsilon^{7/2}}r_e^2 \qquad , for \qquad \epsilon_k < \epsilon < 1, \tag{1.16}$$

$$\sigma_{ph} = 4\pi r_e^2 Z^5 \alpha^4 \frac{1}{\epsilon} \qquad , for \qquad \epsilon >> 1, \tag{1.17}$$

where $\epsilon = E_\gamma/m_e c^2$ and $\epsilon_k = E_{Kshell}/m_e c^2$.
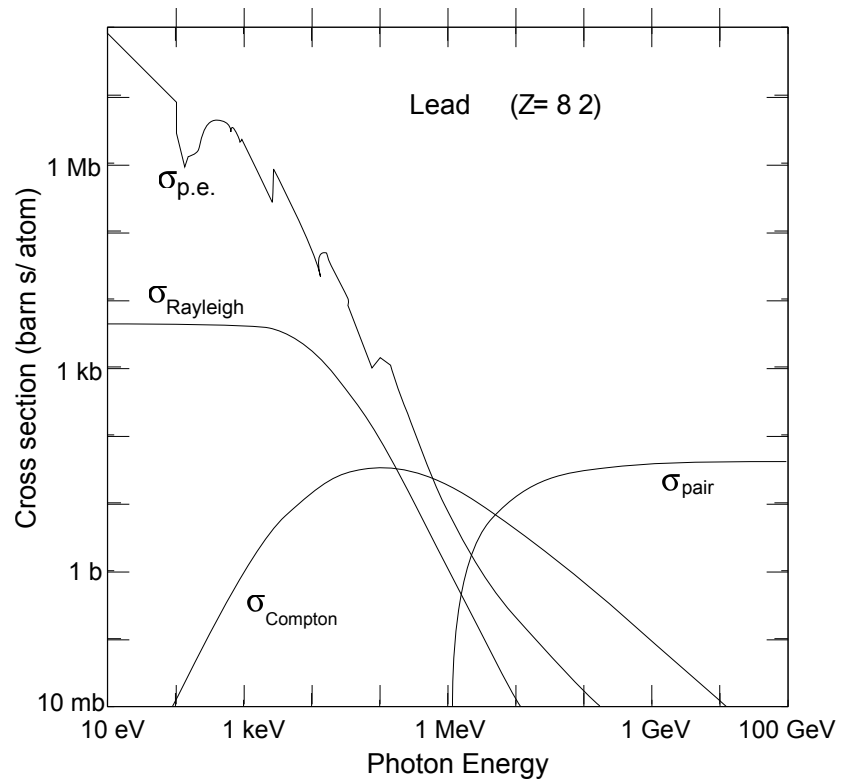
Figure 1.4: Cross section for photoelectric effect, Compton scattering and pair production in lead. Rayleigh scattering is an elastic scattering which will not lead to energy loss and is therefore not described further. The figure is taken from (3).
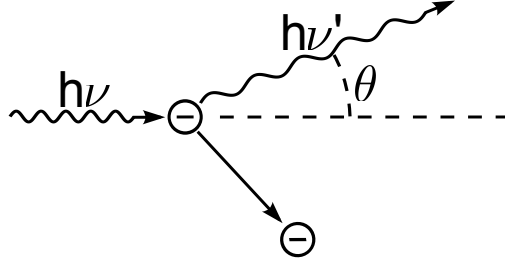
Figure 1.5: Compton scattering.

1.2.2   Compton scattering

A photon can also collide with a semi-free electron and this way transfer energy to it. This is known as Compton scattering and is shown in figure 1.5. Seeing that the energy transferred to the electron is normally much higher than the binding energy of atomic electrons, the bound electrons are considered free when Compton scattered. By detecting the scattering angle the following equation for energy transferal can be derived through momentum and energy conservation,

$$T = h\nu - h\nu' = h\nu \frac{\epsilon(1 - cos\theta)}{1 + \epsilon(1 - cos\theta)}. \tag{1.18}$$

The cross section for Compton scattering is calculated by using the Klein-Nishina formula which according to (2) is:

$$\sigma_c = 2\pi r_e^2 \left[\frac{1 + \epsilon}{\epsilon^2} \left(\frac{2(2 + \epsilon)}{1 + 2\epsilon} - \frac{1}{\epsilon} ln(1 + 2\epsilon) \right) + \frac{1}{2\epsilon} ln(1 + 2\epsilon) - \frac{1 + 3\epsilon}{(1 + 2\epsilon)^2} \right]. \tag{1.19}$$

The recoil energy spectrum of the electron can also be calculated by the Klein-Nishina formula (2),

$$\frac{d\sigma}{dT} = \frac{\pi r_e^2}{m_e c^2 \epsilon^2} \left[2 + \frac{s^2}{\epsilon^2(1 - s)^2} + \frac{s}{1 - s} \left(s - \frac{2}{\epsilon} \right) \right], \tag{1.20}$$

where $s = T/h\nu$. Figure 1.6 shows the distribution of the recoil energy of the scattered electron for several incident photon energies. The maximum energy transferred, T_{max}, in a collision occurs when the scattering angle of the incoming photon is 180°. By inserting this into equation 1.18,

$$T_{max} = h\nu \frac{2\epsilon}{1 + 2\epsilon}, \tag{1.21}$$

this is known as the *Compton edge* and is clearly seen in 1.6 as the sharp drop at the end of each curve.
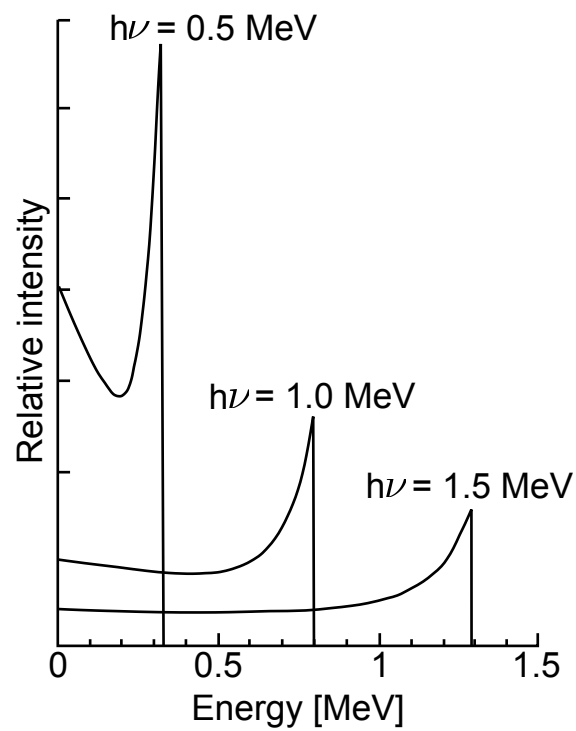
Figure 1.6: Distribution of the electrons recoil energy after Compton scattering. The maximum at the sharp drop at the end of the curve is known as the *Compton edge*. Figure is taken from (2).

1.2.3 Pair production

A high energy photon can turn into an electron-positron pair if the energy is above the rest mass of the pair (1.022 MeV). The process usually happens next to a nucleus since a third body is needed to receive the recoil momentum. If the photon energy is high enough this third body member can also be an electron. The cross section equations for pair production given here are not exact for high Z or low energies. According to (5) the two following approximations are valid:

for $2 << \epsilon << 137Z^{-1/3}$,

$$\sigma_{pair} = 4Z^2\alpha r_e^2 \left[\frac{7}{9}ln2\epsilon - \frac{109}{54} \right],$$ (1.22)

for $\epsilon >> 137Z^{-1/3}$,

$$\sigma_{pair} = 4Z^2\alpha r_e^2 \left\{ \frac{7}{9}ln \left[\frac{183}{Z^{1/3}} \right] - \frac{1}{54} \right\}.$$ (1.23)

An easier way of looking at it is to define the mean free pathway for pair production, which is the mean distance a photon travels before pair production occurs,

$$\lambda_{pair} \simeq \frac{9}{7}X_0$$ (1.24)

1.3 Electromagnetic shower

When a high energy electron or photon hits matter, the dominant way of losing energy will be pair production and bremsstrahlung. An incident photon will turn into an electron-positron pair which will produce more photons through bremsstrahlung, which again will undergo pair production. This will result in a shower of photons, electrons and positrons that continues until the shower has reached the critical energy. The remaining particles will then lose their energy through ionization. In a simple model an incident photon with energy E_0 will turn into an electron-positron pair after one radiation length with approximately $E_0/2$ of energy each. After another radiation length the electron-positron pair will radiate a photon each, resulting in 4 particles. After one more radiation length each of the electron/positron will spawn yet another photon, and the previous photons will turn into a electron-positron pair, giving a sum of 8 particles. This easy model from (2) gives

$$N \simeq 2^t$$ (1.25)

numbers of particles after t radiation lengths, each with an average energy of

$$E \simeq \frac{E_0}{2^t}.$$ (1.26)

If it is assumed that the shower stops when each of the particles reach the critical energy, the maximum number of particles and the length of the shower will be:

$$N_{max} \simeq \frac{E_0}{E_c} \qquad (1.27)$$

and

$$t_{max} \simeq \frac{ln(E_0/E_c)}{ln2}. \qquad (1.28)$$

This is however a very simple model, and to get a more exact model, Monte Carlo simulations are needed. The shower profile is very uncertain since it is dependant on bremsstrahlung. It therefore varies how deep the first particles go before the shower initiates, and it differs in character whether it is set off by a photon or an electron. According to (2) a more precise fit is attained through a gamma distribution,

$$\frac{dE}{dt} = E_0 b \frac{(bt)^{a-1}e^{-bt}}{\Gamma(a)}, \qquad (1.29)$$

where a and b are material constants. The depth where the maximum numbers of particles appear is:

$$t_{max} = \frac{a-1}{b} = 1.0 \times (ln\frac{E_0}{E_c} + C_i), \qquad i = e, \gamma \qquad (1.30)$$

where C_i differs if the shower is set off by an electron or a photon, $C_e = -0.5$ and $C_\gamma = +0.5$.

The shower will also gain in its transverse direction as it develops. This is due to the angle between the electron and positron in pair production, multiple scattering and the angle with which bremsstrahlung is emitted. The unit for measuring the transverse dimension is called the Moliere radius, defined as (2),

$$R_M = X_0 \frac{E_s}{E_c} \qquad (1.31)$$

where $E_s = m_e c^2 \sqrt{4\pi/\alpha} = 21.2$ MeV. The Moliere radius scales roughly independently of material type, and 90% of the shower will be contained within $2R_M$.

1.4   Hadron shower

When hadrons energies reaches above 5 GeV inelastic scattering with nuclei becomes an important part of its energy loss (5). The inelastic scattering will produce new hadrons like pions and kaons, which will ionize and inelastically collide with other nuclei. This way a cascade of hadrons will appear, called

a hadron shower. The scale of how far a hadron goes before undergoing a nuclear reaction is called the nuclear absorption length and is given by (5):

$$\lambda = \frac{A}{\sigma_i N_0 \rho},$$ (1.32)

where A is the mass of one mole of the material, σ_i is the cross section for inelastic scattering, N_0 is Avogadro's number and ρ is the density of the material.

Chapter 2

Semiconductors

Semiconductors have become the material of choice when designing vertex detectors and photon counters. Silicon based strip and pixel detectors are used as vertex detectors in both the ATLAS and the ALICE experiment at CERN. Semiconductor based scintillation light detectors such as the avalanche photon detector (APD) and the even newer pixel based Geiger-mode avalanche photodiodes (G-APD) are taking over for the photo multiplicator tubes (PMT).

This chapter will explain the basics of semiconductors, and the properties which makes them excellent detector materials.

2.1 Band Structure

The electrons in a crystalline material can only inhabit certain energy states, and there can be only one electron in each of these states at a given time according to the Pauli principle. The electron energy states within the lattice of the crystal are so close that they can be considered a continuum, referred to as an energy band. The outermost electrons in an atom that makes up the covalent bindings between the lattice atoms are called the valence electrons. The energy states that these electrons can inhabit are called the valence band. Above the valence band is the conduction band where the electrons are not bound to any one atom, but are free to roam around the lattice. The valence band and the conduction band are often separated by an *energy gap* where there are no states for the electrons to inhabit. Roughly, materials are categorised by the size of their energy gap into three groups; insulators, semiconductors and conductors. The insulators have the largest energy gap, and is usually above 5 eV, the semiconductor have a gap of a few eV, while in a conductor the valence and conduction band overlap. This is shown in figure 2.1 (4; 2).

Electrons in insulators seldom reach the conduction band, while conductors will always have many electrons in the conduction band. Semiconduc-
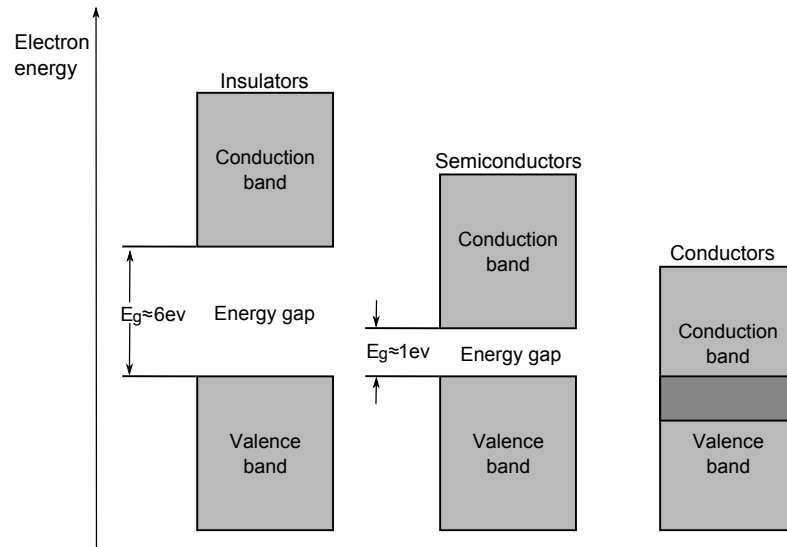
Figure 2.1: Electron energy band structure in insulators, semiconductors and conductors.

tors will mainly have their valence band filled, but there are always some that get excited into the conduction band through thermal movement and radiation. That electrons can be excited into the conduction band is what makes semiconductors great radiation detectors. If an electric field is applied all the electrons in the conduction band will be swept away in the opposite direction of the electric field.

2.2 Charge carriers

At the temperature 0 K and with no radiation present, all the electrons in a semiconductor will be in the valence band, binding the lattice firmly together. At higher temperatures some of the valence electrons will always be excited into the conduction band. When an electron gets excited it leaves behind a hole in the lattice. It is then easy to see that the number of electrons in the conduction band, n_i, is the same as the number of holes, p_i,

$$n_i = p_i. \tag{2.1}$$

When an electron has been excited into the valence band a neighbouring valence electron can move into this hole and leave a hole behind it, as shown i figure 2.2. This way the holes appears to be moving, and it behaves like a positively charged particle. The hole will only disappear when it coincides with an electron from the conduction band.

At temperatures above $T = 0$ K some electrons will always get thermally excited into the conduction band, even with no radiation present. There will
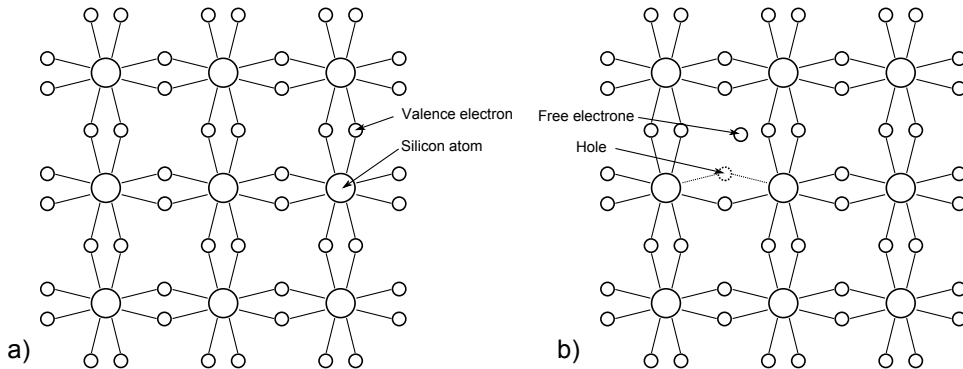
Figure 2.2: (a) Lattice at 0 K and no radiation present; all the electrons are in the valence band. (b) One electron has been excited into the conduction band and has left behind a hole.

also be some electrons and holes that recombine. At any given time there will be some free electrons and holes within the lattice. An approximation of this number is given by (2):

$$n_i = \sqrt{N_c N_v} e^{\frac{-E_g}{2kT}} = A T^{3/2} e^{\frac{-E_g}{2kT}}, \tag{2.2}$$

where the different characters are:

- N_c is the number of states in the conduction band

- N_v is the number of states in the valence band

- E_g is the energy of the energy gap at temperature 0 K

- T is the temperature of the semiconductor

- k is the Boltzmann constant

- A is a material constant

At 300 K this would result in 2.5×10^{13} cm^{-3} electron-hole pairs in germanium and 1.5×10^{10} cm^{-3} pairs in silicon. For comparison, the amount of atoms in silicon and germanium is in the order of 10^{22} atoms/cm^3.

After the electron-hole creation both of them will start to drift randomly around in the lattice. This results in a diffusion away from the point of origin, and the diffusion can be characterised with a Gaussian distribution. The standard deviation of the distribution is the probable distance the charge carriers has diffused away from the point of origin after a certain time, t. According to (4) the standard deviation is given by:

$$\sigma = \sqrt{2Dt}. \tag{2.3}$$

D is the diffusion coefficient and can be estimated by the relation:

$$D = \mu \frac{kT}{e},\qquad(2.4)$$

where μ is the mobility of the electron or the hole, k is the Boltzmann constant, T is the absolute temperature and e is the electron charge.

If an electric field is applied through the semiconductor, all the charge carriers will start to drift parallel to the field. The drift velocity is proportional to the field, E, and the mobility of the charge carrier (2):

$$\nu_{e,h} = \mu_{e,h}E.\qquad(2.5)$$

The charge carrier mobility, μ, depends on both the temperature and the electric field. The velocity of the charge carriers in silicon will vary linearly with the field strength when it is below 1000 V/cm. The velocity reaches its maximum above the order of 10^4 V/cm, reaching a velocity of 10^7 cm/s (2). Above this field strength the charge carriers will experience such an amount of collisions within the lattice that the collective average velocity will seize to increase. Between 100 and 400 K μ will approximately vary like T^{-1} (2). The charge carriers will also diffuse transversely with respect to the electric field lines. According to (4) the diffusion can be approximated by:

$$\sigma = \sqrt{\frac{2kTx}{eE}},\qquad(2.6)$$

where x is the distance the charge carriers have drifted along the field lines. This can somewhat reduce the resolution of position detectors.

2.3   Crystal impurities

The semiconductor discussed so far have been pure semiconductors, called *intrinsic semiconductors*. These are relatively easy to describe in theory, but for silicon and germanium, which are the most commonly used semiconductors, they are virtually impossible to achieve (4). Recombination of electron-hole pairs in intrinsic semiconductor can only happen when the hole and the electron has the exact right energy and momentum values, and is therefore a quite rare process. By calculating the time it would take for an electron-hole pair to recombine in intrinsic semiconductors, the average time would be as large as almost a second. When measuring the recombination time in semiconductors, the recombination time will range from as low as nanoseconds to as much as a few hundred microseconds (2).

The main mechanism for recombination is through impurities in the lattice. The alien atoms within the lattice can create energy states in the middle of the energy gap where electrons and holes can be captured. These trapping and recombination centres are shown in figure 2.3. When electrons
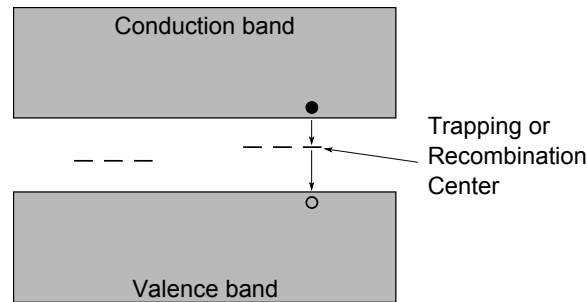
Figure 2.3: Energy states in the energy gap which leads to trapping and recombination of charge.

or holes are captured in these unwanted states they are either held for a period of time, or they recombine with a nearby charge carrier of opposite type. Both impose a problem in detectors. If the charge carrier is trapped longer than the collection time of the detector it will not be counted, leading to a deterioration of the detector resolution. Recombination of several electron-hole pairs further deteriorates the resolution (4). Some impurities will only trap one kind of charge for a certain period of time. If this time is below the collection time it will not be an issue for detector use.

Other kinds of defects in semiconductors are point defects and dislocation. Point defects are vacancies in the lattice, and dislocation are displacement of entire lines of lattice atoms. Point defects are a common problem in radiation damage, which will be presented in chapter 3.

2.4 Doping

Trapping and recombination centres are unwanted energy states close to the centre of the energy gap, but not all impurities are unwanted. In fact, practically all silicon detectors are made with a controlled level of non-silicon atoms to create wanted extra energy states. This is referred to as doping. In silicon, which has 4 valence electrons, the dopants will either be atoms with 3 valence electrons, *p-type*, or with 5 valence electrons, *n-type*. If arsenic or phosphorus are added, which has 5 valence electrons, an "extra" electron will be placed within the lattice. This electron will barely be bound to its host atom and will therefore create an energy states near the conduction band in the energy gap, as shown in figure 2.4 (a). Atoms with 5 valence electrons are called donor impurities. Seeing that it takes so little to excite the "extra" valence electron from the donor impurities, a large amount of free electrons will roam around in the lattice (4; 2).

Similarly, if the silicon is doped with a material that has 3 valence electrons, there will be a "missing" electron to complete the lattice. This will result in an energy state right above the valence band in the energy gap,
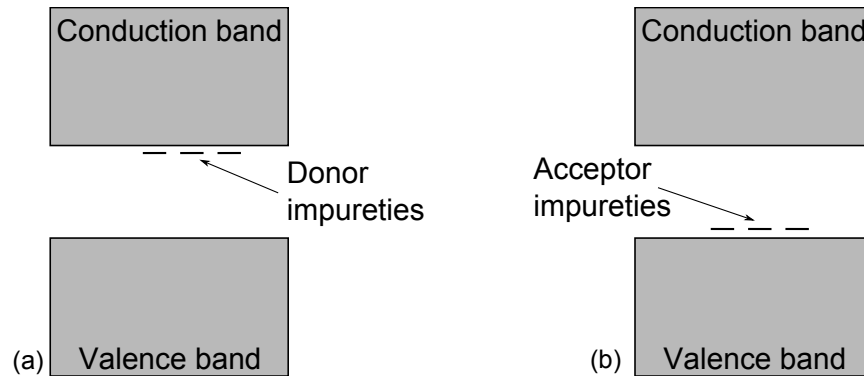
Figure 2.4: (a) Added atoms with an "extra" valence electron, called donor impurities. (b) Added atoms with one "missing" valence electron, called acceptor impurities.

which a valence electron can easily fill, as shown in figure 2.4 b. This kind of doping is called acceptor impurities and creates a majority of holes in the lattice (4; 2).

With the presence of dopants, formula 2.1 is no longer valid. A piece of n-type silicon will have more electrons in the conduction band than holes. This is because the electrons from the donor impurity will not leave behind a hole, and it takes less energy than normal to excite them into the conduction band. Furthermore, since there will be several more electrons than holes, the holes that normally form will be filled much faster by an electron. This way there will be an even larger electron-hole ratio. This will be similar for a piece of p-type silicon, where the concentration of holes will be the *majority carrier* and the electron the *minority carrier*. In a piece of either p- or n-type silicon n denotes the number of electrons in the conduction band, p denotes the number of holes, and the number of holes and electrons in the conductive band of intrinsic silicon is denoted n_i and p_i. According to (4) the following relation is valid:

$$np = n_i p_i. \tag{2.7}$$

Typical electron-hole pair concentration in intrinsic silicon is of the order 10^{10}cm^{-3}, and typical acceptor or donor impurities are 10^{13}cm^{-3} or more (2). If N_D is the number of donor impurities and N_A the number of acceptor impurities, then it follows that (4)

$$\begin{aligned} n &\cong N_D & \text{for n-type silicon,} \\ p &\cong N_A & \text{for p-type silicon.} \end{aligned} \tag{2.8}$$

This gives several orders of magnitude more charge carriers in doped silicon than in intrinsic silicon.
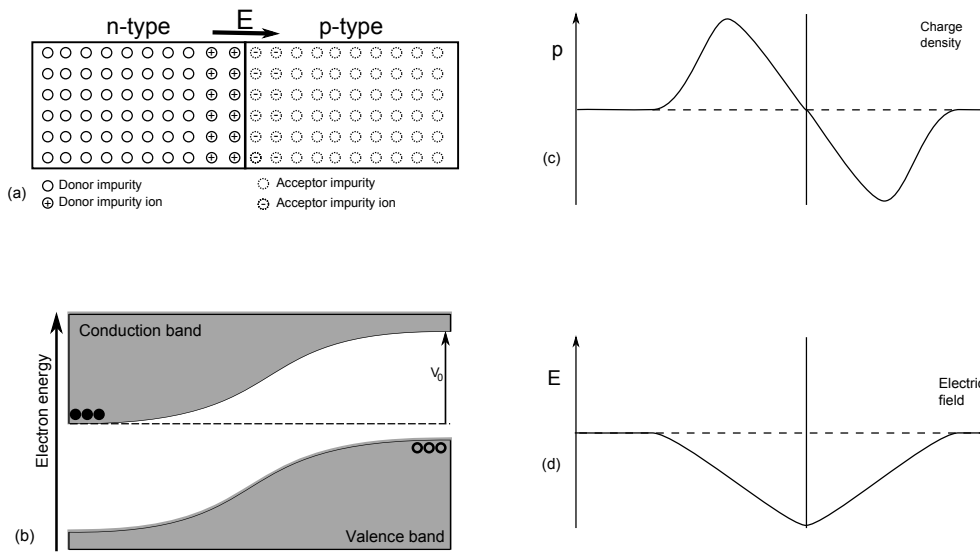
Figure 2.5: (a) The distribution of ions in a pn-junction. (b) The electron energy distribution with the presence of junction potential. (c) Charge distribution or ion distribution. (d) Electric field intensity.

If silicon gets a very large amount of doping, up to 10^{20} cm^3, it is called heavy doping, and it is highly conductive. Heavily doped n-type is denoted n^+ and heavily doped p-type is denoted p^+. Layers of heavily doped silicon is used in detectors as electrical contacts for readout (4).

2.5 The pn-junction

Almost all of the present day semiconductor detectors which are in use are based on a *pn-junction*, except for scintillation crystals (2). This is done by taking a piece of silicon and doping one side into n-type and the opposite side into p-type, such that the two doped regions are in close vicinity.

In the n-type semiconductor lots of electrons are free to move around the lattice, as holes are in the p-type. When a pn-junction is formed, some of the electrons close to the junction will diffuse over to the p-side where they will be captured by a hole. This will create negatively charged ions in the p-type. Similarly some of the holes will diffuse over to the n-type side and create positively charged ions in the n-type semiconductor. This formation of ions creates an electric field in the direction from the n-type towards the p-type, as is shown in figure 2.5. The electric field will grow until an equilibrium is formed that hinders any more holes to diffuse over to the n side, and any more electrons over to the p-side (4; 2). The potential

of this electric field is given by the Poisson equation,

$$\nabla^2 V = \frac{\rho(\overrightarrow{r})}{\epsilon},$$
(2.9)

where V is the potential, $\rho(\overrightarrow{r})$ is the charge density and ϵ is the dielectric constant of the semiconductor. The electric field can be found by integrating the equation above, which gives:

$$E = -\nabla V = \frac{1}{\epsilon} \int \rho(\overrightarrow{r}) d\overrightarrow{r}.$$
(2.10)

This region of ions is called the depletion zone, and has very favourable radiation detection properties. The depletion zone stretches from the beginning of the positive ions to the end of the negative ions, this length is called the *depletion depth*. The depletion depth can be calculated by solving the Poisson equation in one dimension. If radiation creates an electron-hole pair anywhere but the depletion zone, the electron hole pair will recombine after a short while. If the pair is however created within the depletion zone the electron and the hole will be swept away in opposite directions due to the electric field, and can then be detected (2; 4).

The depletion depth and the potential difference in the region can be calculated by equation 2.9 by using equation 2.8 to set the charge concentration. The potential difference V_0 are calculated to be (2):

$$V_0 = \frac{e}{2\epsilon}(N_D x_n^2 + N_A x_p^2),$$
(2.11)

where x_n is how far the depletion region stretches into the n-type region, while x_p is how far it is extended into the p-type region. These can according to (2) be calculated by:

$$\begin{array}{rcl} x_n & = & \left(\frac{2\epsilon V_0}{eN_D(1+N_D/N_A)}\right)^{1/2}, \\ x_p & = & \left(\frac{2\epsilon V_0}{eN_A(1+N_A/N_D)}\right)^{1/2}. \end{array}$$
(2.12)

The entire depletion depth can then be found from:

$$d = x_n + x_p = \left(\frac{2\epsilon V_0(N_A + N_D)}{eN_A N_D}\right)^{1/2}.$$
(2.13)

The naturally created electric field formed by the pn-junction is far from optimized for radiation detection. The electric field is rather small with a potential of about 1 V (2), which is not an efficient way of moving the charge. The depletion depth is also small, which causes three problems. First, small depletion zone gives a small area where radiation can be detected. Fewer of the electron-hole pairs created in the semiconductor then gets detected.

Secondly, the velocity of the charge carriers is small. This gives a higher transit time through the semiconductor, which results in a higher probability of recombination or trapping. Third, as the detector is part of an electric circuit the pn-junction has the properties of a capacitance, and a large capacitance that comes from a small depletion zone introduces much noise in the circuit. The capacitance is given by

$$C = \epsilon \frac{A}{d}, \tag{2.14}$$

where A is the area of the depletion zone.

2.6   Reversed bias pn-junction

The three problems presented above when using the pn-junction for radiation detection can be overcome by applying an external electric field. By applying positive voltage at the end of the n-type semiconductor, and a negative voltage at the p-type, the natural electric field from the junction will be enhanced, as shown in figure 2.6 a. This applied potential will force the free electrons from the n-type semiconductor through the depletion zone where they will be captured by holes, similarly the holes will be forced away from the p-type semiconductor. This makes the depletion zone grow which results in a smaller capacitance and a larger effective detector (4).

The amount of electron-hole pairs created by a passing particle is proportional to the energy deposited in the semiconductor, i.e. the energy loss of the particle. Ideally the depletion zone should extend throughout the semiconductor in order to gather all this charge (2; 4).

The enhanced electric field also gives the charge carriers a larger drift velocity, which lowers the probability of recombination and shortens the collection time. If the electric field is very large the charge carriers can receive enough kinetic energy between two collisions so that secondary charge carriers are released due to ionization, referred to as *impact ionization* (6). This way an avalanche of charge is created, yielding a larger signal. If the electric field is even higher one would enter what is known as the *Geiger mode*. Here, for every ionizing particle that gets absorbed, a complete breakdown of the detector is observed no matter the amount of energy deposited. This creates a sort of yes/no detector. Detectors that utilise this will be presented in the next chapter.

The problem with a very high bias voltage is that it needs a very high resistivity semiconductor. If the resistivity is not high enough the detector will break down and start to conduct, which often destroys the detector (2).
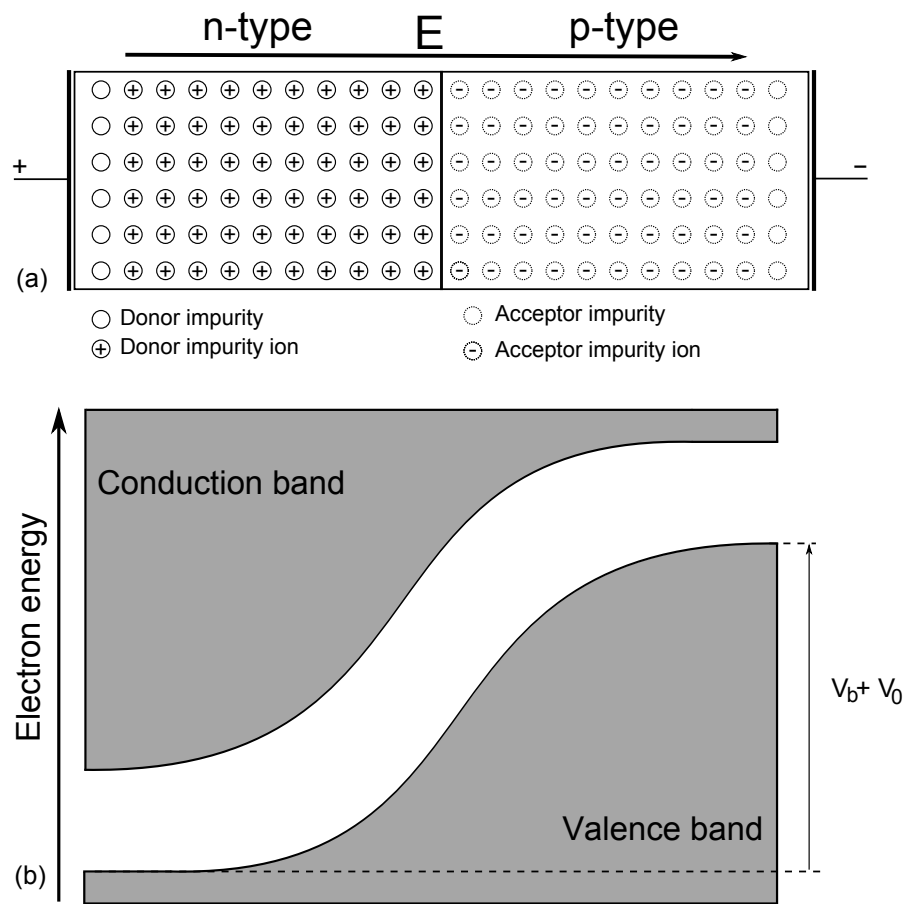
Figure 2.6: (a) Depletion zone with applied bias voltage. (b) Electron energy distribution with an applied bias voltage, roughly the same height as the applied bias voltage.

Chapter 3

Silicon pixel detectors

Almost all electrical detectors made of semiconductor materials today are silicon based. Some are also made by germanium, but due to germanium's small energy gap it needs cooling to avoid an overwhelming amount of thermal noise (4). In mass, silicon is also the second most abundant material in the world after oxygen (7). However, silicon is not necessarily a cheap substance to use since it needs to be highly purified in order to get a sufficiently high resistivity if one wants to apply a large bias voltage. Other substances, such as GeAs, SiC and diamonds, are being studied to replace silicon as detector material (8).

Vertex detection in particle and nuclear collisions are mainly done by silicon detectors. Silicon is also being more and more used to create sensors for reading out scintillation crystals. Examples are the silicon strip detectors and the avalanche photodiode (APD). To achieve higher resolution in both position (vertex) and energy (scintillation light) readout, different kinds of pixel based silicon detectors are being developed.

3.1 Pixel vertex detectors

In large particle and heavy ions experiments there are usually several layers of detectors. The detectors are created to measure different parameters, like position, momentum and energy of secondary particles. These layers usually surround a point where two particle beams collide with each other, or one beam collide with a fixed target of some sort. The point where the collision takes place is referred to as the *interaction point* (IP). When particles collide at the IP several new secondary particles are produced, and it is these new particles that are of interest.

The vertex detectors are usually the detector layers closest to the IP. In both the ATLAS and ALICE experiment at the large hadron collider (LHC) each of the six vertex detector layers lies like a cylinder around the IP. When a new particle is produced at the IP the vertex detector senses where the
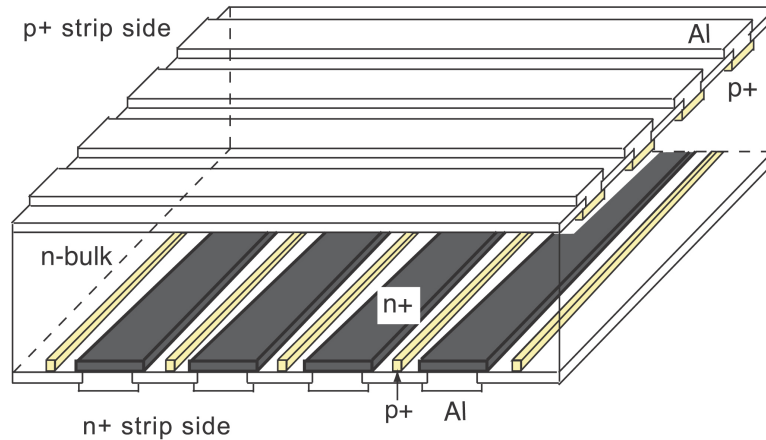
Figure 3.1: Principle drawing of a double sided silicon strip detector, taken from (9).

particle passes through it.

Pixel detectors have always been the golden way of achieving very high position information in nuclear and particle physics experiments. Since reading out every pixel at high rates requires fast computers and an extreme amount of readout channels, silicon strip detectors were developed as a more sophisticated solution to this problem. Silicon strip detectors are normally created on a n-type substrate where thin, heavily doped p-type strips with electrodes on top are formed atop of the substrate. When radiation creates electron-hole pairs the p-strip reads out that it has been struck, gaining one of two dimensions. To get the other dimension charge division or double sided strip detectors are employed (6). An example of a double sided strip detector is shown in figure 3.1.

Problems arise when the particle flux through the silicon strip detector gets too high. If two particles passes through one electrode with very little time difference, they might get registered as one hit with a coordinate where none of them hit. This is not an obstacle for pixel detectors.

In addition to solving this problem pixel detectors also gives higher granularity and lower capacitance. There are many different designs of pixel detectors, though the main difference is how they are read out. Different pixel detectors will be discussed below, after the radiation damage section.

3.1.1   Radiation damage

Since the vertex detectors are the closest detectors to the IP they have to withstand a tremendous amount of radiation. The two layers of pixel detectors at the ALICE experiment in LHC are positioned around the IP at radii 3.9 and 7.6 cm. The innermost layer will be radiated to a fluence of the

order of 10^{12} neutrons/cm^2 in 10 years without suffering any large radiation damage (10). The mechanisms of radiation damage has to be understood in order to develop the most radiation hard detectors. The most important ways radiation affect the efficiency of pixel detectors are presented here. The two main types of radiation damage is bulk damage and surface damage.

Bulk and surface damage

Radiation damage known as bulk damage is the most important form of radiation damage. As energy loss normally produces electron-hole pairs it can also displace atoms, creating a *primary knock on atom* (PKA). The PKA leaves its place in the lattice and gets lodged between other lattice atoms. This vacancy and the interstitial atom is known as a *Frenkel pair*. Both the lattice hole and the lodged atom creates point defects in the silicon. The threshold for this process is ~ 25eV, but if the PKA receives a recoil energy above ~ 5KeV it will create a cluster of defects at the end of the PKA track (11).

The surface of silicon detectors is covered with silicon dioxide (SiO$_2$) which forms naturally on pure silicon in oxygen, and is placed there purposely to protect the detector silicon (6). Since the SiO$_2$ layer at the surface already has a distorted atomic lattice, bulk damage does not affect it in any crucial way. Even though the SiO$_2$ layer is not an efficient detector material, it does produce electron-hole pairs when struck by radiation. Since the electrons have a larger mobility than holes they escape the surface layer into the detector material where they get collected. The holes, on the other hand, get stuck in the surface layer creating a set of fixed, positive charges. This hole trapping seem to reach a saturation when radiated to ~ 1 KGy, reaching a hole concentration of about 3×10^{12}holes/cm^2 (8).

Crystal damage and leakage current

The crystal defects, which is the most destructive, comes from radiation damage in the silicon bulk, and creates unwanted energy states in the energy gap. These new energy states work as generation/recombination centres within the silicon, and is a source for increasing leakage current, charge loss by trapping and recombination, change in effective dopants concentration and increased resistivity of the undepleted bulk (8).

According to (8) the leakage current is dependant on the fluence, Φ, and can be expressed as

$$J(\Phi) = \alpha \Phi J_{Intrinsic}, \tag{3.1}$$

where $J(\Phi)$ and $J_{intrinsic}$ is the volume density leakage current in the detector after radiation and in intrinsic silicon. α is a damage constant which relies both on the temperature and the time after radiation has finished.

The mechanism where leakage current changes after radiation has finished, is called *annealing*, and has currently no complete physical explanation (8).

Effective doping

When detector silicon gets radiated its effective doping will change. As the fluence increases more acceptor states arises, and possibly lowers the number of donor states making the substrate heavier p-doped as it is irradiated. According to (12) the effective doping is characterised by:

$$N_{eff}(\Phi, T, t) = N_{eff,0} + N_A(\Phi, T, t) + N_C(\Phi) + N_Y(\Phi, T, t). \qquad (3.2)$$

The $N_{eff,0}$ term in equation 3.2 is the effective doping concentration before it gets radiated. $N_A(\Phi, T, t)$ is called the short term or beneficial annealing term,

$$N_A(\Phi, T, t) = \Phi \sum_i g_{a,i} e^{-\frac{t}{\tau_{a,i(T)}}}. \qquad (3.3)$$

It behaves as a series of exponential terms which converges towards zero, and at higher temperature fewer parts are detectable.

The second term, $N_C(\Phi)$, is called the stable damage term because of its lacking time variable, and is given by:

$$N_C(\Phi) = N_{C0}(1 - e^{-c\Phi})g_c\Phi. \qquad (3.4)$$

The stable damage term is not affected by temperature either, so it can not be manipulated by changing room temperature. $N_Y(\Phi, T, t)$ is the final term of equation 3.2, and the most important at large fluences. It is called the "reverse annealing" or "anti-annealing" term, and is given by:

$$N_Y(\Phi, T, t) = g_y \Phi \left(1 - \frac{1}{1 + t/\tau}\right). \qquad (3.5)$$

To lengthen the lifespan of the detector within a normal doping concentration it is therefore usual to design the detector with a n-type bulk. The effective doping concentration will then diminish with fluence in the beginning, and will start to increase when the bulk has effectively changed into p-type. Thus it will take longer for a n-type bulk to become heavily doped in a radiation environment than a p-type.

Accumulation layer

As mentioned there is a buildup of positive charge in the surface Si0$_2$ layer of the detector. This positive layer will attract electrons in the silicon bulk, and this way induces a negative layer in the bulk called an accumulation layer. The accumulation layer can compromise the isolation between pixels on the n-side of the sensor and shorten the n-layer (8). The formation of the

accumulation layer can also degrade the resistivity of the sensor and increase the total capacitance of the detectors, decreasing the signal to noise ratio (SNR). To prevent the formation of the accumulation layer two methods have been developed, the P-stop (13) and P-spray (14) techniques.

The P-stop is created by making some sort of p-type structure around each electrode in the n-type substrate preventing the formation of an accumulation layer. Several types of P-stop structures has been tested, and several effectively hinders this accumulation layer, but they are expensive and hard to create.

P-spray is generally thought to be a better solution and is the one chosen in the ATLAS pixel detector (15). The P-spray technique is simply to grow a thin p-type silicon layer at the top of the substrate, which forms a secondary pn-junction at the top. As the substrate is radiated, and holes forms in the SiO_2 layer it will cancel out the electric field from the pn-junction created by the P-spray, making it close to intrinsic.

3.1.2 Different kinds of pixel detectors

As mentioned at the beginning of this section, the main difference of the various pixel detectors is how they are read out. The pixel detectors will also differ in material budget, which should be as low as possible to avoid multiple scattering, as well as readout speed and cost.

The principle of the sensitive area of a pixel detector are mostly the same. Normally this means starting with a lightly doped n-type silicon substrate with heavier doped n-type and p-type on the bottom and top layer to created the wanted pn-junction. One of these layers of heavier doping are formed into separate regions, pixels, and connected to electrodes. This is called a *planar sensor*.

Charge coupled devices (CCDs)

A principle sketch of how charge coupled devices (CCDs) works is shown in figure 3.2. When a CCD is struck by radiation the resulting charge carriers, usually electrons because of their high mobility, will gather under the closest electrode. Since there is a layer of insulating material between the electrode and the substrate they do not get collected at these electrodes. Instead a sequential shifting of the potential on these electrodes moves the rows of charges downwards into a register, which again is sequentially shifted towards a collection node on the right where they are read out.

The advantage of CCDs is that their simple design allows very small pixels, which is already used in digital cameras. According to (16) this should also be possible to do in a vertex detector CCD by creating "fine pixel CCDs" with a pixel size of 5μm. This way very high resolution is achieved as well as avoiding the problem with many hits on one pixel before
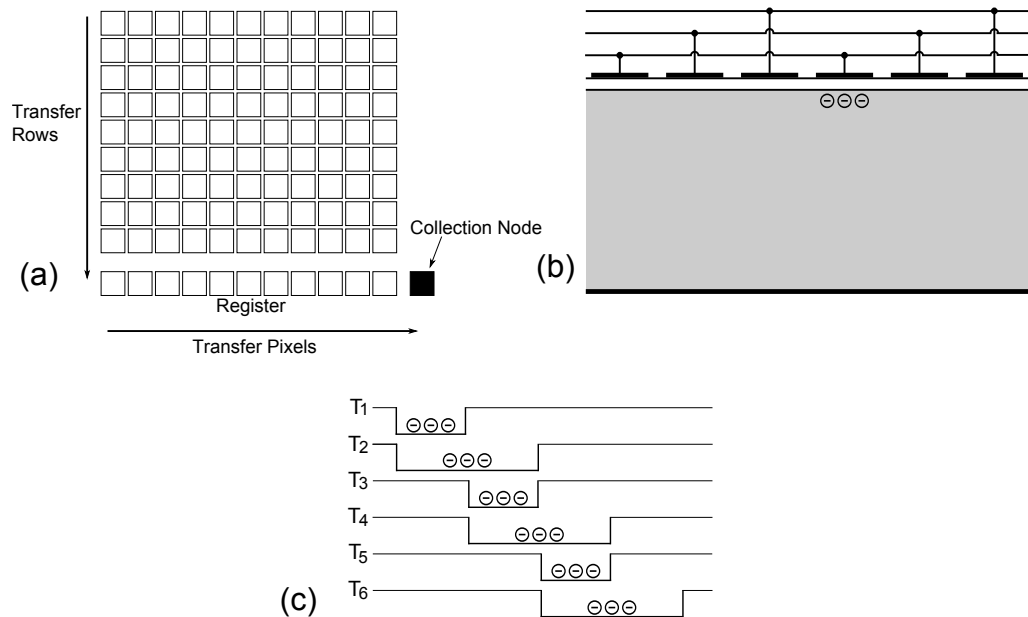
Figure 3.2: The principle operation of a 3-phased CCD chip. All the rows are moved down one step by periodically changing the potential under each pixel. The row at the bottom goes into the registry, and are then sequentially transferred into the collection node the same way as the rows get moved.

readout, gaining low *occupancy.*

The material budget is extremely low for CCDs, with only 0.6% of X_0 per layer in the SLD detector at Stanford Linear Collider (SLC) (17).

The serial readout is a slow process since there is an upper limit of how fast it is possible to move a group of electrons from one electrode to another. To speed it up, it is possible to have one collection node for each row. It is also possible to create a 2-phased CCD, opposed to what is shown in figure 3.2, where a sinusoidal clock is used. This way it is possible to get a clock frequency of 50MHz (18).

Even though newer CCDs can be made fast, it might not be enough in a collider experiment. Camera CCDs have shutters, so when the CCD is read out it will not get hit by light. If there is a collision inside a collider while the CCD were read out, it would create electron-hole pairs in the CCD while the sequential moving of charge where taking place. The tracks coming from the readout period would then be registered at the wrong position. To avoid this the CCD should be read out in between collisions.

Hybrid pixel detectors

Hybrid pixel detectors are the most used pixel detectors in modern collider detectors, and are used in both the ALICE and ATLAS experiment as the
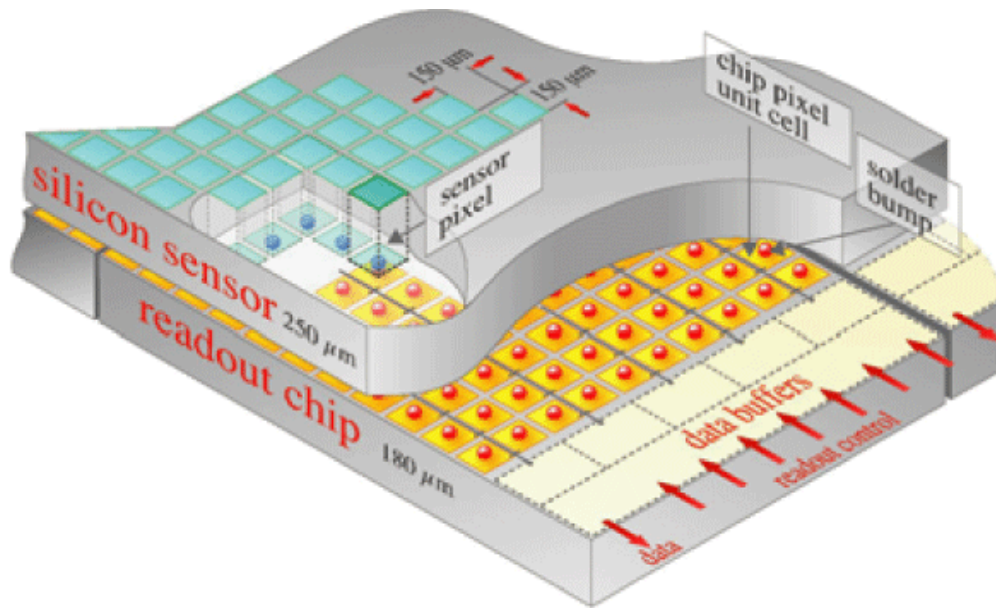
Figure 3.3: Hybrid pixel detector, where the planar sensor is bump-bonded to the readout chip. Figure is taken from (19).

innermost layers. Hybrid pixels are perhaps, conceptually, the simplest kind of pixel detectors, and are shown in figure 3.3. Basically the sensor is a lightly doped substrate with squares of higher dopants and electrodes on top like a checker board. Each of these squares are electrically isolated from each other. To read out these pixels each of them are soldered to their own readout electronics and amplifier through a soldering process called *bump bonding* (6).

In most of the other pixel detectors the readout electronics and the sensor are inseparable; one cannot change one of them without changing the other. This is not the case in hybrid pixel detectors, which is both its advantage and disadvantage. Since readout electronics and the sensor are separable, one can be altered without changing the other, making optimization of both readout and sensory properties easier. In other pixel detectors, where the sensor and readout is combined in the same device, the material budget would however most probably be smaller. This is because the hybrid pixel detector has one layer of sensory silicon then another layer of silicon based electronics, and in the case of the ALICE pixel detector, 25μm bump bonding between them (20). According to (21) all these layers results in a material budget of 1% of X_0 with support and cooling in the ALICE pixel detector.

Seeing that each of the pixels are connected to their own readout it is the readout electronics that determines how fast the entire matrix is read out, unlike the CCDs. In the ALICE experiment the readout time of the
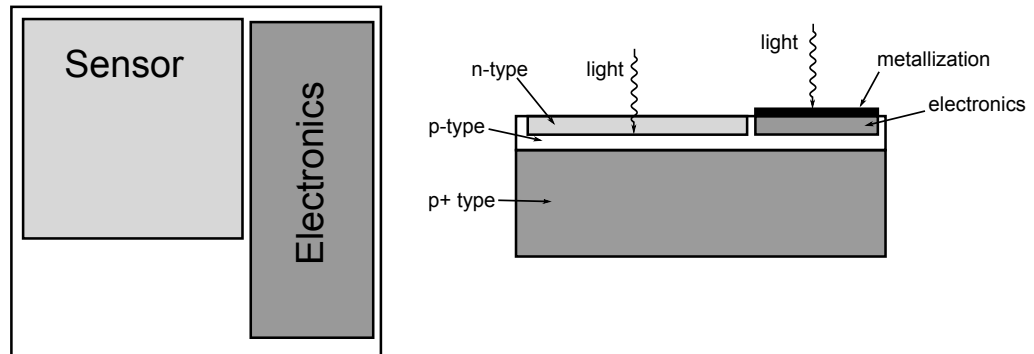
Figure 3.4: A CMOS imager pixel, the electronics and sensor is separated. The readout and amplification electronics are connected to the sensor through a metallization layer. This metallization layer also prevents light to penetrate the circuits. The left side shows the pixel from above and the right shows the different layers of the device.

entire pixel detector is 256μs (21).

Monolithic detectors

The principle behind a monolithic detector is to have the pixel sensor and the readout electronics on the same silicon wafer. This should be possible as both the sensor and the electronics, integrated circuits (IC), are silicon based. This is already done in most commercial hand held digital cameras, but has proven more difficult to do in detectors. Detectors require highly purified, high resistivity silicon in order to get a good signal and a large depletion region. If typical silicon for electronics were used the depletion depth would be quite shallow, and the distorted lattice would capture too many charge carriers to get a good signal. Since visible light only penetrates $0.5 - 7\mu$m, sensors have been developed for light, called *CMOS imagers* and are shown in figure 3.4. In the CMOS imagers the readout and amplification circuitry are separated and connected through a metallization layer. The metallization layer covers all of the circuitry and shields it from incoming light (6).

It is quite clear that a different approach than that of CMOS imagers has to be used to create monolithic detectors for collider experiments. Since it is not possible to shield electronics from high energetic particles, and dead space is unwanted the IC should be put on top of the sensor element. Several types of monolithic designs exists, e.g:

- Silicon-on-insulator (SOI)

- Depleted field effect transistor (DEPFET)
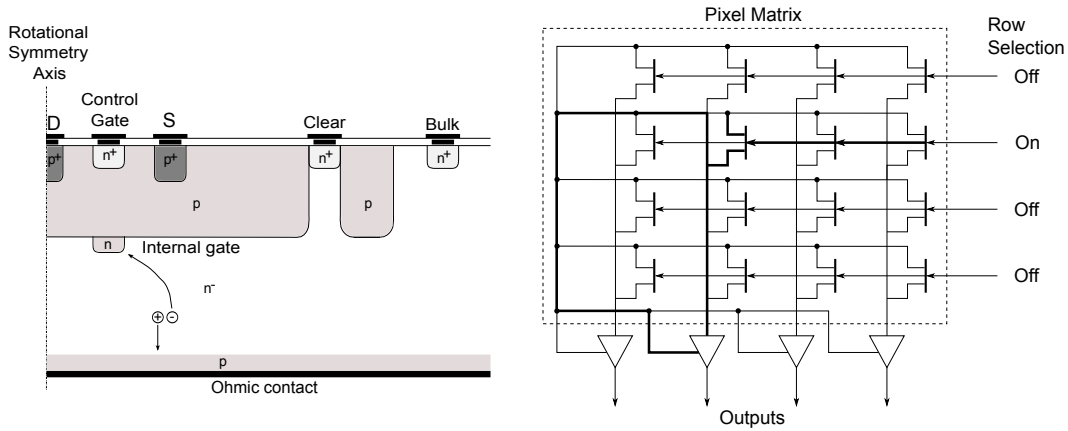
Figure 3.5: DEPFET device principle drawing.

- Monolithic Active Pixel Sensor (MAPS)

Since a full understanding of monolithic detectors require a good understanding of ICs and transistor technology, which is beyond the scope of this thesis, only a short description of the DEPFET device will be presented here.

DEPFET

The DEPFET device is basically a matrix of connected transistors on a detector grade silicon substrate, as shown on the right in figure 3.5. The transistors can either be MOSFET (Metal Oxide Semiconductor Field Effect Transistor) or JFET (Junction gate Field Effect Transistor). A JFET device is shown on the left of figure 3.5, but a MOSFET is just as easy in principle. When radiation forms electron-hole pairs in the detector grade substrate, the holes go to the back of the detector on the p^+ layer while the electrons gather at the internal gate, which is a potential well about 1 μm under the gate control. When a potential is applied at the control gate current flows between the source (S) and drain (D) of the transistor with or without electrons at the internal gate. However, when there are electrons present at the internal gate the current in the transistor will be modulated, making the current roughly proportional to the number of electrons. Therefore one pixel can be read out several times without removing the charge carriers at the pixel, called nondestructive readout. To remove the charge from the internal gate a positive potential is applied to the clear node (22).

Unlike the CCD each pixel can be read out individually. All the control gates in a row are connected in parallel, and all the drains and sources in a column share a readout line. When a pixel is read out the control gates in the pixels row is bussed. Then the source and drains of the pixels column is connected to the output channel.
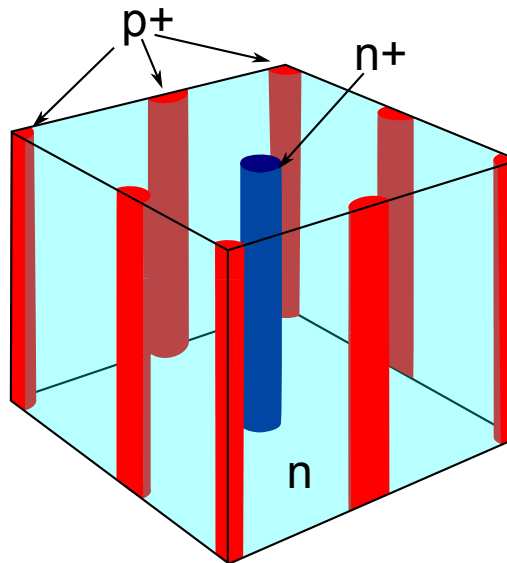
Figure 3.6: A 3D detector pixel. N-type substrate with a n+ column in the middle, surrounded by p$^+$ columns. The electrons will be collected at the n+ column, while the holes get collected at the p$^+$ columns.

Since the transistor is the first step in an amplifier circuit, the DEPFET device is a combined amplifier and detector, which results in noise reduction. The capacitance is also very low for each pixel, gaining even lower noise (6).

According to (23) the DEPFET detector should meet the requirements of the vertex detector at the ILC.

3D silicon detector

A relatively new sensory pixel design called a 3D detector is shown in figure 3.6. The pixel design should be able to be integrated in a monolithic design or bump bonded to existing pixel readout electronics (24). A bump bonded version is being tested and considered for the pixel upgrade in the ATLAS experiment (25).

The sensory design, which can be seen in figure 3.6, consists of a n-type substrate with a matrix of n$^+$ and p$^+$ type silicon, shaped as thin columns through the entire substrate. Even though the substrate of the detector can be as thick as 300 μm the collection distance can be as small as 50 μm, according to (26). This leads to a signal strength as strong as the normal 300 μm planar sensor, but with smaller collection distance and thus shorter collection time. Shorter collection time gives both better time resolution and smaller chance of recombination and trapping. Since radiation damage increases the chance for trapping and recombination, the shortened collection time in 3D detectors will make them more radiation

hard. The electrode configuration of the 3D detectors also allow *active edge*, which is sensitive edges on the detector, unlike the planar devices. The short distance between the n^+ and p^+ columns also decreases the depletion voltage which reduces the power dissipation.

The geometrical shape of the 3D detector also leads to higher capacitance than the planar device, which gives more noise. 3D detectors are also more expensive than the planar device. According to (27), 3D detectors in ATLAS will be about 2-3 times more expensive than the planar pixel detectors.

3.2   Pixel scintillation light detectors

When designing silicon detectors for visible light other considerations than that for position detectors has to be made. The detectors described in this section are used for reading out, or detecting the light from scintillation crystals. Unlike the high energetic particles that pass through the entire pixel detectors creating thousands of electron-hole pairs, the visible photons will be absorbed after a very short distance, and only create one electron-hole pair. These detectors should therefore have little or no dead space at the entrance, low noise and contain some sort of intrinsic amplification in their design.

Traditionally, Photo Multiplier Tubes, PMTs, has been used to read out scintillation crystals, but their high operating voltage, sensitivity to magnetic fields and low quantum efficiency has created room for newer technologies. Avalanche photodiodes, APDs, have also been developed for light detection, but their low gain makes them less than perfect.

3.2.1   Avalanche photodiodes (APD)

The Avalanche PhotoDiode (APD) employ impact ionization as a built in amplification, see section 2.6. The electric field in an APD is high enough to accelerate the charge carriers to such high velocities that they will ionize the silicon, creating secondary particles. The secondary charge carriers will also be accelerated and further ionize the silicon which results in an avalanche of free electrons and holes. The probability for a charge carrier to produce a secondary ionization depends strongly on the size of the energy gap of the semiconductor and the strength of the electric field. The number of secondary charge carriers created per unit length by an incident electron or hole is called the impact ionization coefficient and differs greatly between the two in silicon, as seen in figure 3.7. According to (28) the impact ionization
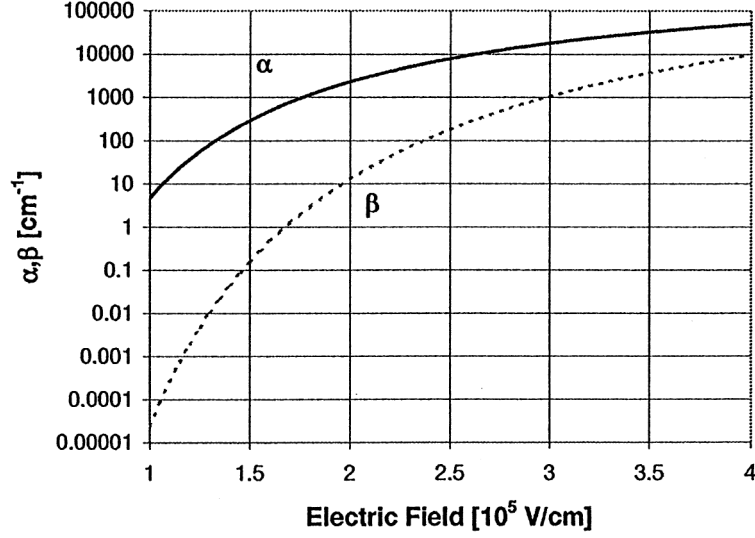
Figure 3.7: The impact ionization coefficients for electrons, α, and holes, β in silicon. The figure is from (28).

coefficients in silicon is given as:

$$\alpha(E) = 2300 \exp\left[-6.78\left(\frac{2 \times 10^5}{E[\text{V/cm}]} - 1\right)\right] \qquad \text{for e,} \qquad (3.6)$$

$$\beta(E) = 13 \exp\left[-13.2\left(\frac{2 \times 10^5}{E[\text{V/cm}]} - 1\right)\right], \qquad \text{for h.} \qquad (3.7)$$

In silicon, the electrons will clearly dominate the avalanche process, especially for lower E-field.

The multiplicity, M, denotes how many charge carriers that gets created per absorbed photon, and is dependent on the impact ionization coefficients. According to (28) the multiplicity is given as:

$$M(x) = \frac{\exp[\int_0^x (\alpha(x') - \beta(x'))dx']}{1 - \int_0^L \{\alpha(x') \exp[-\int_0^{x'} (\alpha(x'') - \beta(x''))]dx''\}dx'}. \qquad (3.8)$$

Since the avalanche is a statistical process M is an approximate number of charge carriers released by an absorbed photon. The output current of the APD will therefore be proportional to the number of photons absorbed in the APD, called *proportional mode*. Typical gains of an APD is between 50 and 200, and is therefore dependant on low noise amplifiers (29).

The ratio $\beta/\alpha = \kappa$, called the *k-factor*, affects the *multiplication noise* (30). Normally one would want as large electric field as possible, gaining a large M, but since this also increases the k-factor, which increases multiplication noise, it should not be done.
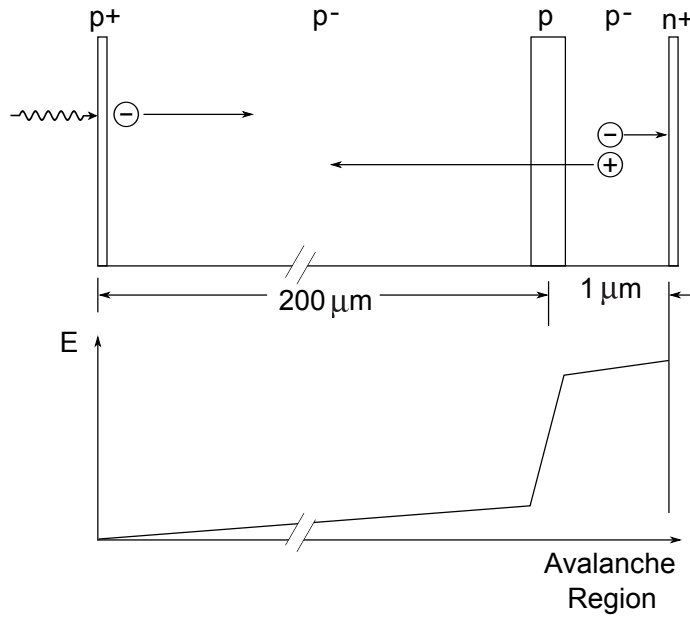
Figure 3.8: Doping configuration and field in an APD. Figure is taken from (6).

Figure 3.8 shows an optimized design of an APD. The avalanche region is designed to be far from the entrance window through a series of different p-doped layers. The holes are collected at the p$^+$ side while the electrons get collected at the n$^+$ side. This way only the electron, with its higher impact ionization coefficient, drifts into the avalanche region, reducing multiplication noise. The long drift region also deepens the detector, making the capacitance smaller.

Geiger mode APD

If the reverse bias voltage is increased beyond the proportional mode, exceeding the *breakdown voltage*, holes will also participate in the avalanche by impact ionization. This leads to a lasting and growing current from the diode. Mathematically it can be seen that the denominator of equation 3.8 will reach zero. The multiplicity will then diverge to infinity and there will be a continuous creation of electron-hole pairs. The current, I, will increase until the voltage drop across the diodes internal resistance, R, halts the current growth:

$$U_{breakdown} = U_{bias} - IR. \qquad (3.9)$$

This leads to a steady state current through the diode after a time period of the order RC, where C is the diode capacitance (31). Operating the APD above the breakdown voltage is known as *Geiger mode*.

The two ways of stopping the current of the Geiger mode APD are called *active quenching* and *passive quenching* (31). In active quenching the current is somehow detected and the bias voltage is lowered below the breakdown voltage, bringing the current to a halt. In passive quenching a large series resistance, $R_S >> R$, is placed between the diode and the power supply. The time it takes the diode to reach the breakdown voltage and stop is of the order RC, while it takes the order of $R_S C$ to recharge it. If the R_S is too low the diode will be continuously recharged and never go below breakdown voltage, resulting in the steady current as portraited in equation 3.9. If R_S is very large the recharge time becomes significant. Photons that hit the detector before it is fully recharged will yield a lower signal than normal.

Seeing that the avalanche is quenched as soon as the voltage over the diode drops down to the breakdown voltage, it is possible to calculate the gain of these devices. Diodes have the properties of capacitors, so the charge released after a voltage drop is given by:

$$Q = C(V_{bias} - V_{breakdown}).$$
(3.10)

To calculate the gain, G, in number of charge carriers the total charge has to be divided by the charge of a single carrier, namely the electron charge:

$$G = \frac{Q}{q_e} = \frac{C}{q_e}(V_{bias} - V_{breakdown}).$$
(3.11)

This shows that a Geiger mode APD with a quenching mechanism will give a finite gain at a given voltage no matter the energy or the amount of photons which sets off the avalanche. This creates a sort of yes/no detector which leaves no information about what hit it, but with the ability to detect a single photon.

3.2.2   Pixel Geiger mode APD; G-APD

This section will deal with the different pixel based scintillation detectors. In short terms they work as a large amount of very small Geiger mode APDs, and two different designs will be presented below. The terminology can be a bit confusing as several names apply to similar devices. Each company that produces these devices has given them their own name, and 3 of the devices will be presented here:

1. Micro-pixel avalanche photodiode, MAPD, from Zecotek imaging systems.

2. Multipixel photon counter, MPPC, from Hamamatsu Photonics.

3. Silicon photo multiplier, SiPM, from MEPhI-PULSAR.
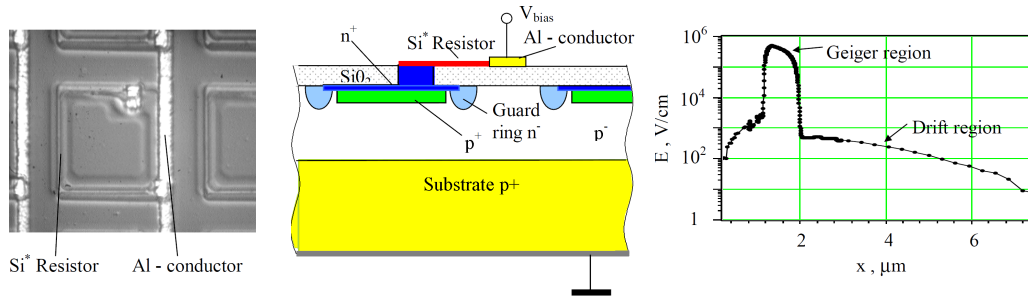
Figure 3.9: Images of a SiPM pixel. Left: Photographic image of the SiPM pixel. Middle: Topology of the pixel where a photon enters at the top through the SiO$_2$ layer. Right: Distribution of electric field strength where $x = 0$ starts at the top. Image is taken from (34).

In the general discussion concerning all these devices the term G-APD will be used in this thesis as this is the common term in newer articles concerning the matter.

Some of the reasons to develop the G-APD, and replace the APDs and PMTs:

- high gain

- low bias voltage

- insensitive to magnetic fields

- relatively cheap

- single photon detection capabilities

SiPM/MPPC

The first SiPM where developed in Russia by MEPHI-PULSAR, later the Japanese company Hamamatsu developed their MPPC upon the same principle (32; 33). Here SiPM will denote the principle design of both the Russian SiPM and the Japanese MPPC as this is mostly done in articles concerning the matter.

The SiPM is built on a low resistivity p$^+$ doped silicon substrate with a grown high resistivity epitaxy p$^-$ silicon layer on top. The lower resistivity p$^+$ layer serves as support structure for the detector. The pixels are formed by doping squared n$^+$ p$^+$ junctions upon the p$^-$ epitaxy layer, as shown in figure 3.9. While the common p$^-$ substrate defines the drift region of the detector, the electric field strength has a sudden rise at the n$^+$ p$^+$ junction making this the Geiger region where the avalanche takes place. This depletion zone is about 0.7 - 0.8 μm thin with a field strength of (3-5) $\times 10^5$ V/cm (34). Each pixel is electrically separated by a polysilicon

resistive strip and guard rings surrounding each pixel. The resistive strips are shown in the left image of figure 3.9 and are marked Si* resistor. The n^- guard rings help forming the electric field around each pixel.

The charge released from a pixel has to pass through the Si*-resistor strip that surrounds the pixel and onto the aluminium conductor to be read out, shown on the left of figure 3.9. This way the Si*resistor works as a passive quenching resistance. All the pixels are read out by a common aluminium conductor, so it is not possible to know where the charge came from, unlike for the pixel vertex detectors. The amount of charge collected by the SiPM divided by the charge released by a single pixel gives the number of fired pixels. The number of fired pixels should be coherent with the photon intensity that hit the detector.

If the photon is absorbed in the SiO_2 layer, or penetrates too deep and gets absorbed in the undepleted p^+ bulk, the electrons will not drift into the avalanche region and create a signal. The biggest issue with the SiPM design is still that there is a non-sensitive area between the pixels, *dead space*, which makes up a portion of the surface. The effective area is typically 25% to 65% of the total area (35; 33). This issue will be further elaborated in the *photo detection efficiency* section below. The gain of the SiPM devices are typically $10^5 - 10^6$ (36; 33). This makes the devices excellent for single photon counting.

MAPD

Instead of placing the pixels at the top with the drift region underneath them, like the SiPMs, the MAPD has buried micro-wells which define the pixels. This is shown in figure 3.10. The MAPD is formed on a low resistivity n-type silicon with a grown high resistivity epitaxy p-type layer on top. The micro-wells are formed as n^+ dots in the middle of the p-type epitaxy layer. This creates three pn-junctions, first a p-n junction between the top part of epitaxy layer and the micro-wells. Then a n-p junction between the micro-wells and the bottom part of the epitaxy layer, and at last a p-n junction between the epitaxy layer and the low resistivity n-type bulk silicon. This special p-n-p-n formation makes the first and the last p-n junction reversed biased, while the middle n-p junction will be forward biased. The result is a local minimum of 0.5-0.7V in the electric potential in the n-p junction right below the micro-wells (37). The avalanche takes place in the p-n junction above the micro-wells, and the released electrons from the cascade will stop at the local potential minimum after a few nanoseconds. This gathering of charge at the potential minimum will change the potential enough to quench the avalanche. A few tens of nanoseconds after the avalanche the accumulated electrons will drift down to the n-type silicon bulk due to leakage.

The two great advantages of the MAPDs are that there are no dead space
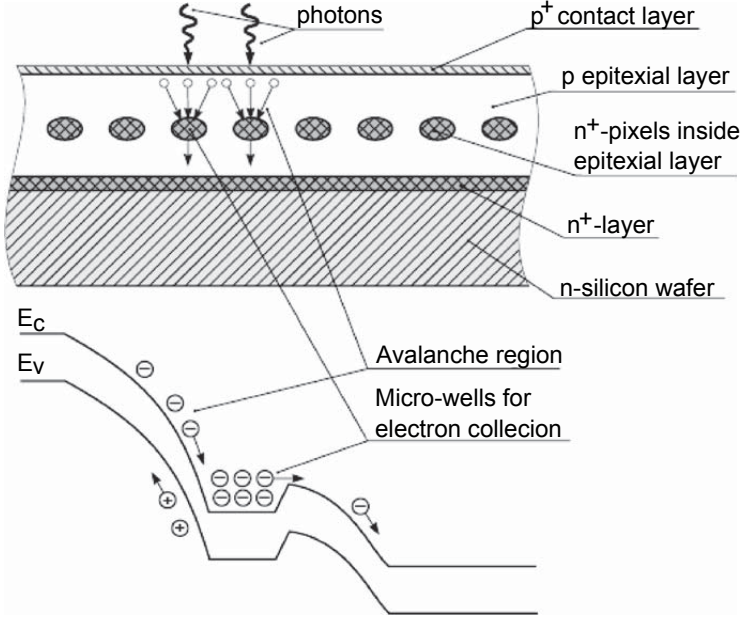
Figure 3.10: Topology and electric field configuration of a MAPD. Image is taken from (37).

between the pixels, giving a 100% effective area, and an immense amount of pixels. Whereas the SiPMs have maximum 1000-2000 pixels/mm^2, the MAPDs reaches pixel densities of 40000 pixels/mm^2 (37). MAPDs should therefore be linear at higher light intensities than the SiPM.

The gain of the MAPD is of the order 10^5, about an order of magnitude lower than the SiPM design. This makes MAPD the worse candidate for photon counting at low light intensities.

3.2.3 Properties of the Pixel Geiger mode APD devices

The different designs of the G-APDs give them some deviations in characteristics which should be taken into account when selecting one for a given task. This section presents some of the more important characteristics that needs to be considered.

Photon detection efficiency (PDE)

The photon detection efficiency, PDE, is the probability that a photon incident on the G-APD surface is detected. The PDE is defined as (29):

$$PDE = QE \times \epsilon \times P_{trigger}. \qquad (3.12)$$

QE is the *quantum efficiency*, which is the probability that the absorbed photon creates a photo electron in the active layer of the G-APD, and is
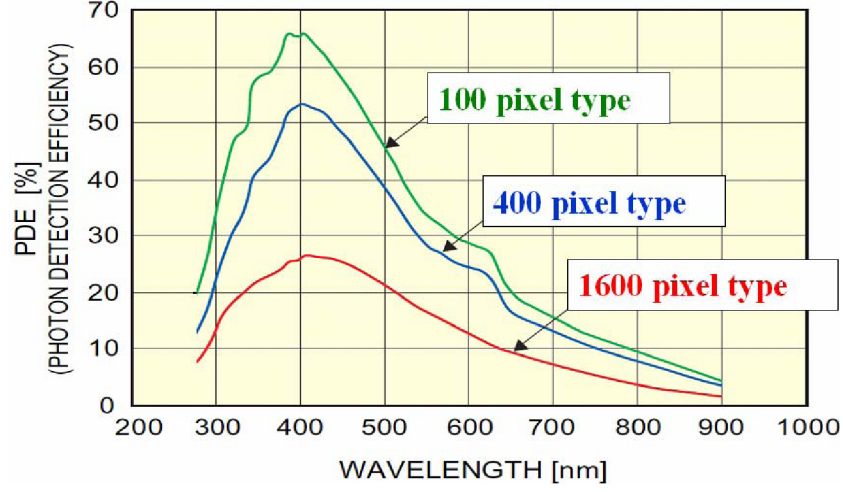
Figure 3.11: PDE of three different MPPC devices from Hamamatsu. The pixel type number refers to the pixel densities per mm of each device. The figure is taken from (33).

dependant on the photon wavelength. ϵ is the ratio of the active area of the detector, A_{pixels}/A_{total}. For MAPDs the active area is 100%, while it is about 25% - 65% for SiPM designs (35; 33). $P_{trigger}$ is the probability that the photo electron created in the active area initiates a breakdown. $P_{trigger}$ is dependent on the bias voltage and will increase by raising the voltage.

Figure 3.11 shows the PDE of three different MPPCs (SiPMs from Hamamatsu), which are clearly dependent on the photon wavelength. Since there is about the same amount of dead space between adjacent pixels, lower pixel densities means a larger active area. This leads to higher PDE for low pixel densities, as illustrated in figure 3.11.

Dynamic range

At low light intensities the probability is rather low for two individual photons to hit the same pixel within the pixels' recharge or dead time. In these conditions the G-APDs work as linear devices, though in reality they are strictly non-linear. If a detector is hit by a flash of light that lasts shorter than the dead time of the pixels the number of fired pixel will approximately be (38):

$$N_{fire} = N_{pixels} \left[1 - e^{-\frac{PDE \times N_{photons}}{N_{pixels}}} \right]. \tag{3.13}$$

$N_{photons}$ is the number of photons which is incident on the detector surface and N_{pixels} is the total number of pixels. With respect to the dynamic range it is clear that a high pixel density is an advantage, making the MAPD design

Figure 3.12: Principle of thermal excitation (left) and tunnelling in silicon (right).

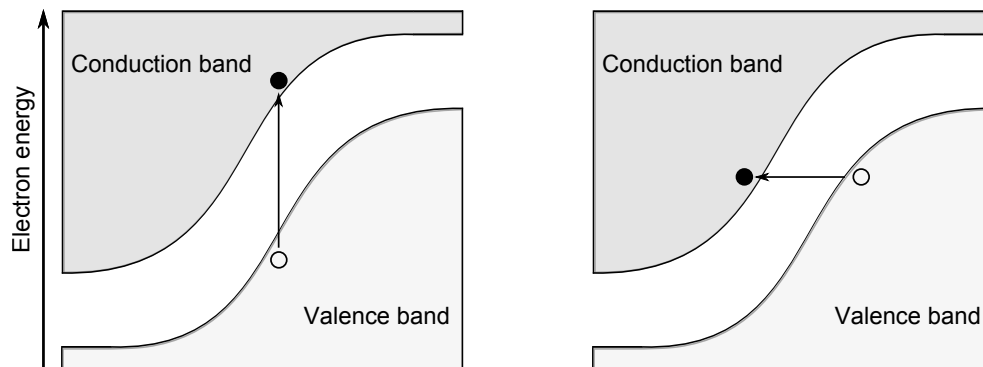superior to the SiPM when considering this aspect.

Dark rate

Every produced electron-hole pair in the active layer of a G-APD can trigger an avalanche. This means that it is not just the absorbed photons that trigger avalanches, but all other processes that create electron-hole pairs in silicon. The counts which do not come from photons are called dark rate, and are highly unwanted. The dark rate of a G-APD is of the order $10^5 - 10^6$Hz per mm^2 and are mainly the result of two processes: thermal excitation and tunnelling.

It is well known that silicon has a higher conductivity at higher temperatures, i.e. it has more electrons in the conductive band at higher temperatures. This is what makes silicon a great material for temperature sensors (thermistor), but it represents a problem in G-APDs. By cooling the detectors the amount of thermally excited charge carriers is reduced. For every 7-8 ℃ the temperature is reduced the thermally generated dark rate is lowered by 50% (38; 29).

At high electric field strengths tunnelling makes up a considerable part of the dark rate. There are two forms of tunnelling, band-to-band and trap-assisted tunnelling (39; 40). Band-to-band or direct tunnelling is when the electron tunnels directly from the valence band to the conductive band. This is very dependant on the electric field strength, and the dark rate from direct tunnelling can therefore be reduced by lowering the bias voltage, though this will also reduce gain and PDE. The trap-assisted tunnelling uses a nearby generation/recombination centre to tunnel an electron through to the conductive band. To lower the dark rate from trap-assisted tunnelling there has to be fewer impurities in the silicon.

The dark rate can be reduced immensely by setting a threshold on the
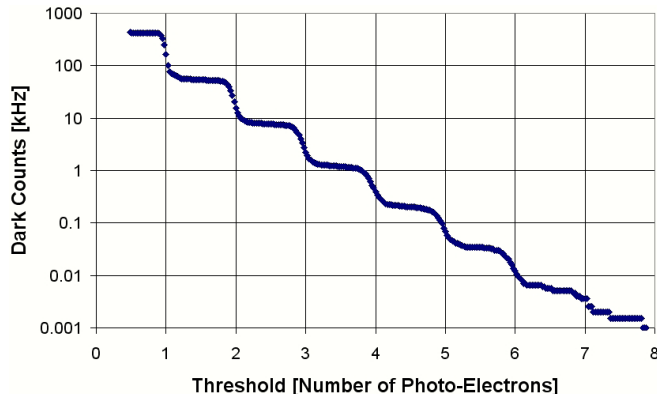
Figure 3.13: Reduction of dark rate by increasing the discriminator threshold. The X-axis gives the amount of fired pixels before a readout is triggered, while the Y-axis is the corresponding dark rate . The figure is taken from (29).

output charge of the G-APD before triggering a readout. Each time the threshold is increased equivalent to the yield of one breakdown, the dark rate is approximately reduced by one order of magnitude (35; 29). A plot of this is shown in figure 3.13.

Cross talk

During the avalanche in a pixel photons are emitted from the avalanche process itself with an energy above 1.14 eV, corresponding to the silicon gap energy. Approximately 3 photons per 10^5 secondary electrons produced are emitted from the avalanche (38; 29). The average energy of these emitted photon are 1.7eV with the characteristics of black body radiation at about 4000K (41). Some of these photons leave the pixel where they are produced and are absorbed in another pixel, usually a neighboring pixel, and start an avalanche there. This results in several more pixels fired then actually hit by incoming photons, and these are not possible to reduce by setting a higher threshold, like for the dark rate. To parametrize the probability of optical cross talk, α_x, with a continues dark rate in the background the following formula is used (38):

$$r_n = r_1 \alpha_x^{n-1}, \tag{3.14}$$

where r_n is the rate when there is a discriminator threshold n before a readout is triggered, and r_1 is the rate without any threshold.

Since the production of secondary photons is proportional to the number of electrons in the avalanche they can be reduced by lowering the bias voltage over the diode. This is unwanted since this reduces the PDE of the detector. Other possibilities is to optically insulate each pixel by etching

grooves or trenches between each pixel (29; 35). This is also not a method without drawbacks since this will increase the dead space between pixels, and therefore reduce the PDE.

Recovery time and afterpulsing

The recharge time in the SiPM is normally dependant on the capacitance of the pixel and the serial resistance connected to it. This gives a first order time constant $R_S C$. In the MAPD design, the recharge time will be the time it takes for the electrons to leave the micro-wells. The recovery time and pulse decay is measured in (42) for three different MPPC devices, and are presented in table 3.1.

The region inside the silicon where the avalanche takes place is raised to a few thousand degrees during the avalanche, coherent with the black body radiation described in the previous section. After such an avalanche many of the deep lying traps in the energy gap are filled. Since some of these can be released several hundreds nanoseconds after the breakdown, they can start a new avalanche after the original has finished, and the pixel has been recharged. This will further increase the noise (29).

Shorter afterpulses, which are released charge carriers during recharge time, will elongate the time it takes to fully recharge the diode. This results in pulses which are below normal breakdowns and longer recharge times.

Table 3.1: Measurement of three different MPPC devices with different pixel densities. Taken from (42).

Type	1600 px	400 px	100px
Bias voltage [V]	V_0+3.3	V_0+2.7	V_0+0.87
Recovery time [ns]	~ 4	~ 9	~ 33
Pulse decay time [ns]	~ 5	~ 11	~ 35

Chapter 4

Experimental setup

The purpose of this thesis is to make a setup for testing single pixels of pixel based detectors, both vertex detectors and G-APDs. The detector lab at IFT is currently focusing on characterisation and the application of G-APDs, and not pixel vertex detectors. Thus the work has mainly been focused on developing a setup especially suited for testing G-APDs. It should however also be able to test single pixel response of vertex detectors in the future with some alterations.

The experimental setup has been used to characterise two types of Hamamatsu MPPCs, one with 25×25 μm^2 pixels named 25C and one with 50×50 μm^2 named 50C. This thesis is in many ways a continuation of Hege A. Erdals master thesis (1) from 2009 to characterise G-APDs.

The heart of the thesis is a setup consisting of 3 stepper motor stages, the XY-table, which is used to move the detectors. These stages has proven faulty, and a pattern recognition system has been built in order to correct for the faulty stepping of the stages. The pattern recognition is done through a CCD camera on a microscope above the stages. To trigger the pixels of the MPPC a flash of light has been focused through the microscope and onto the pixels. A sketch of this is shown in figure 4.1.

4.1 The XY-table

To target single pixels a XY-table from 1999 was used. The XY-table belong to the particle physics group, and was last used by Lars G. Johansen in a master thesis (43) to probe silicon strip detectors for ATLAS. The XY-table has not been used since. The XY-table essentially consists of three stepping motors that can move a detector in all three directions with micrometer precision. Primarily the XY-table moves the Device Under Test (D.U.T.) in 2 dimensions, where the Z-stage is used to focus the D.U.T. when inspecting through the microscope. With the XY-table every pixel on a MPPC chip can be found and triggered automatically.
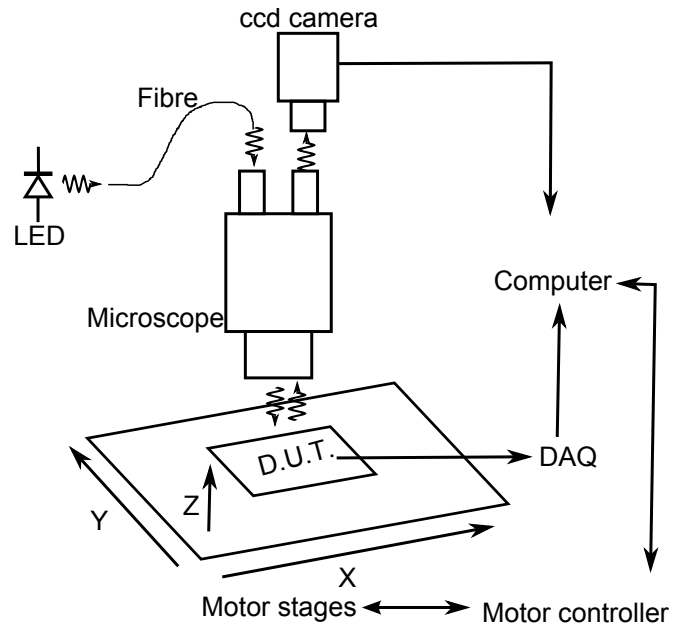
Figure 4.1: Sketch of the setup. The computer moves the stages through a motor controller. The computer can do pattern matching through a video stream from the CCD camera. The LED pulses the D.U.T., the data acquisition system (DAQ) gathers information from the D.U.T. and sends it to the computer for processing.
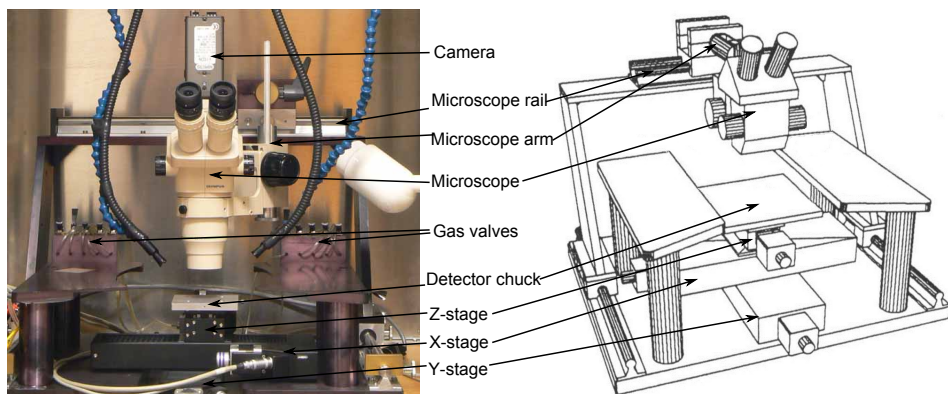

Figure 4.2: Photo and sketch of the XY table before changes. This setup was used for silicon strip detectors in 1999 by Lars G. Johansen.

The XY-table is shown in figure 4.2, and consists of:

- Light proof aluminium cabinet

- Detector chuck

- 3 stepping motor stages holding the detector chuck

- Motor controller

- Two platforms on either side of the detector chuck

- Microscope bridge with a microscope and a camera connected to the microscope

- Vacuum valves

The cabinet was placed on a wooden table with metal legs on wheels.

4.1.1 Light proof cabinet

All the equipment listed above is placed inside the light proof cabinet, except for the motor controller. The cables going into the cabinet were pulled through two black s-shaped tubes that works as a light lock. The tubes were also filled with black cloth to stop all light from coming through. The cables going to the stepping motors and the signal cables coming from the MPPCs were separated into different tubes. At first the signal cables shared a tube with some of the motor cables. This resulted in a periodical low frequency, high amplitude noise signal on the MPPC output signal from the motor cables.

Originally the cabinet were designed to be light proof, but when a light source was placed inside the cabinet one could clearly see light coming out through a gap around the doors. This was fixed by installing two new bolts, and placing new isolation rubber around the doors.

The inside of the cabinet was polished aluminium, creating a reflective surface for the light that might enter the cabinet through any unseen cracks. To absorb any light that might enter, the entire inside of the cabinet was covered with black plastic. Finally, all the edges and screw holes around the cabinet was covered with black electrical tape.

4.1.2 Stages and chuck

The X- and Y-stages are the rectangular boxes shown at the bottom in figure 4.2. Theses boxes contain rails on which a carriage are moved back and forth by turning a screw bolt at the centre of the box. The screw bolts are turned by stepping motors. The Y-stage is placed at the bottom whereas the X-stage is placed on top of the Y-stage carriage. The Z-stage is placed on top
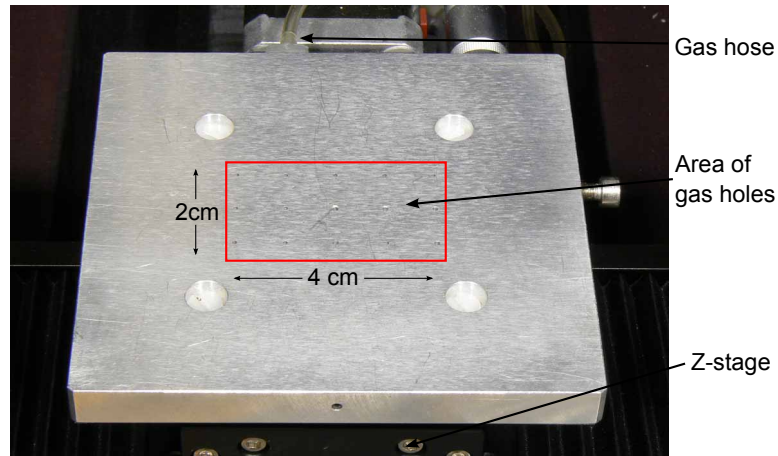
Figure 4.3: Photo of the chuck that holds the detector during scans.

of the X stage carriage. According to the manufacturers specifications, each of these stages should have a resolution of 0.5 μm.

The detector chuck is a 10×10 cm^2 aluminium table atop of the Z stage. It is shown in figure 4.3. It is designed to hold the detector firmly by applying a vacuum between the detector and the chuck. A vacuum hose can be connected at the back of the chuck and to the vacuum valves at the back of the cabinet. The vacuum channels inside the chuck comes up through a 2×4 cm^2 area of small holes at the surface of the chuck. The vacuum is created by a pump outside of the cabinet, and is used to firmly hold the MPPC and its readout electronics during scans.

The MPPC's readout electronics is placed inside an aluminium box, where the MPPC is connected at the front, and the bias voltage and signal output cables are connected to the back. The readout box can be seen in figure 4.4, and the electronics will be presented in the data acquisition section, 4.4.

4.1.3   Motor controller

The three stepping motors are managed by a motor controller positioned outside of the cabinet. The controller has three input channels:

- IE488/GPIB

- RS232

- Joystick interface

For some reason the GPIB interface did not work, but since the RS232 has worked flawlessly no time has been used to find the reason for the GPIB

Figure 4.4: Photo of the box that contains the readout electronics for the MPPC. It holds the MPPC, and supplies it with bias voltage.

malfunction. The joystick is a helpful feature when testing the stages and positioning the detector while looking through the microscope before scans.
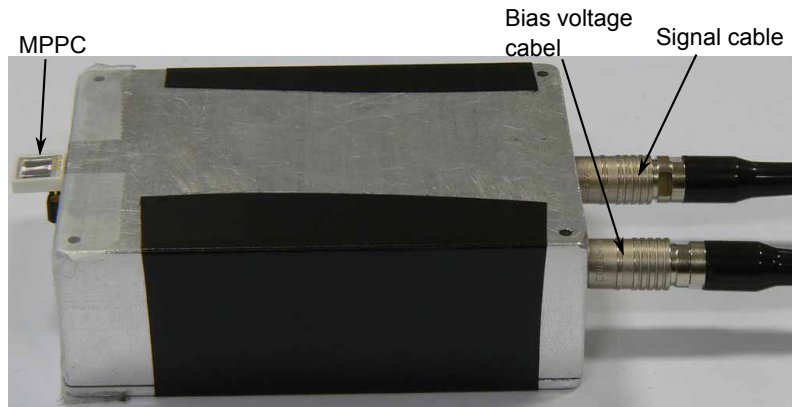
To communicate with the controller through the computer, different ASCII string commands are sent and received through the RS232 interface. The command language is called Venus 1, and contains a diversity of commands to move the stages and set different operation modes. Venus 1 is a high level programming language which does not need a compiler. The controller simply interprets the commands and executes the proper action. Examples are the command **pos** which makes the controller send back the coordinates of its current position, and **2_3_1_m** which moves the carriages of the stages to the coordinate (2,3,1).

4.1.4 Microscope and camera

Behind the XY-table is a microscope bridge holding a microscope[1], which is shown in figure 4.2. To achieve higher magnification an additional lens has been connected to the objective of the original microscope. This makes it able to get a clear view of a single MPPC pixel. Two rings with bright LEDs are taped around the lens to illuminate the MPPCs, which gives a very good contrast. The lens is shown in figure 4.5.

The microscope has two oculars and a third opening for mounting cameras. The left ocular is always open while there is a switch to choose whether the image is sent through the right ocular or to the camera slot. There is an adapter[2] for c-mount cameras in the camera slot.

There was originally an analogue Pal-B camera connected [3] to the mi-

---

[1]Olympus SZ 11, 11x zoom.
[2]Olympus SZ-CTV.
[3]Vicon VC2600 DSP.
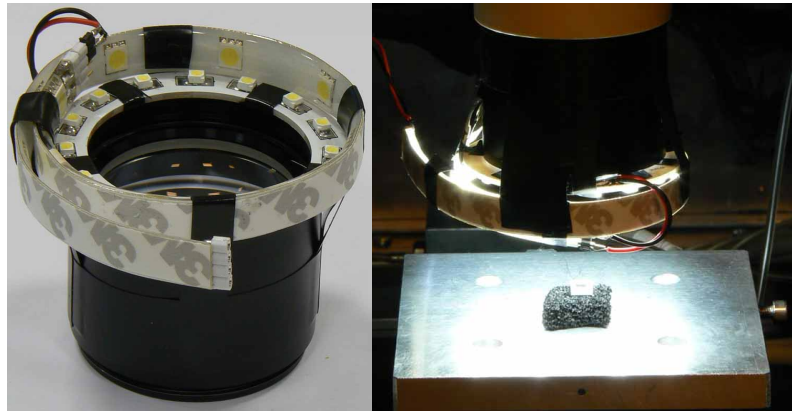
Figure 4.5: Photo of the additional microscope lens with LEDs connected to it. The ring of LEDs illuminates the MPPC under the microscope in order to get a higher contrast.

croscope. This camera can be seen mounted to the microscope in figure 4.2. A TV-card[4] had to be used in order to get the image onto the computer.

It was decided to buy a new camera for the microscope with a digital interface instead of using an analogue TV card. The old camera had a low resolution of 752x582, and LabVIEW only managed to receive a 320x240 resolution from it. The contrast was also not optimal, which made it hard to recognise the smallest pixels. The new camera[5] has a S800 FireWire interface (IEEE 1394b), 1288x964 resolution and a 12-bit color contrast.

4.1.5   Vibrations

As mentioned, the entire XY-table and its aluminium cabinet is placed on a 30mm thick wooden table with iron legs on wheels. This dose not give any real vibration dampening. When people walk where the XY-table is stationed the vibrations are clearly seen on the microscope camera. Other vibrations manifesting through the building, like slamming doors and machinery, are also seen.

Since that the microscope hangs from an extended arm it is more likely that the majority of the seen vibrations comes from vibrations in the microscope rather than vibrations in the detector fixed on the chuck. These vibrations can however be problematic when mounting a light source which shall trigger single MPPC pixels.

No attempt to reduce or remove the vibrations has been done in this thesis, even though they have given minor problems. To reduce the vibrations during scans of the MPPCs the scans have be done in the evenings

---

[4]Brookhaven bt878.

[5]Point Gray, Flea FL2G-13S2M/C.

and nights.

The most common way to reduce vibrations is to use a vibration dampening table. This could be done by using a heavy table plate made of steel to absorb most of the vibrations. A more sophisticated dampening table is made by lifting a thick steel plate by air pressure. This is called pneumatic dampening and is often expensive. A cheaper solutions might be to place the table on spikes, as done with loudspeakers.

4.2 Triggering the pixels

To test the single pixel response of the MPPCs a very narrow and fast flash of light has to trigger a single pixel several thousand times before moving onto the next pixel. Since the smallest pixel is 25×25 μm^2 the light spot hitting the pixels should not be bigger than this. The flash should also not last longer than a few nanoseconds, such that it is well below the recharge time of the pixels.

4.2.1 Laser

The original idea for this master thesis was to use a laser to trigger each pixel. The microscope arm is connected to a rail behind the XY-table, and a laser could be connected to the same rail with a similar arm. The microscope would then have to be tilted to a small angle to make room for a laser to be positioned above the MPPC, which did not represent any problem.

The only down side of using a laser to trigger the pixels was cost. The MPPCs are most sensitive to violet and blue light, as shown in figure 3.11. Laser emitting blue light is among the most expensive lasers. The laser would also be able to send a few nanosecond short pulse, and have a very narrow focus. The idea should work, but because of cost other options were considered.

4.2.2 Optical fiber

A less costly, but more technically difficult solution was to position a very narrow optical fibre right above the MPPC. As the light from a fibre is emitted at an angle the fibre should be positioned just a few μm above the MPPC. The fibre itself should also be as narrow as possible. The thinnest mass produced optical fibres are the single-mode fibres used in computer networking, with a diameter of 8-9 μm. The single-mode fibre that was tested has a big connector compared to the fibre thickness, called a ST-connector, and is shown in figure 4.6. The fibre had to be stripped and should have a clean cut at the end to avoid scars along the end of the fibre which would emit light. After careful consideration this approach was abandoned due to the complexity:
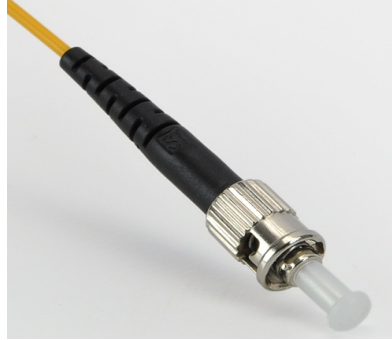
Figure 4.6: Photo of a ST connector. Common in single- and multi-mode fibres.
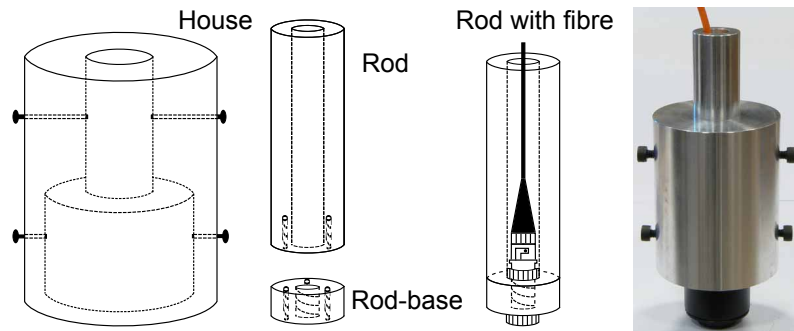
Figure 4.7: Sketch and photo of the fibre mount. The ocular goes into the large opening of the house, while the rod goes into the smaller opening. The rod-base has grooves for connecting a ST-coupler in order to connect a fibre. At the far right is a picture when it is assembled, and ready to be placed in the left ocular slot.

- Getting a clean cut. Normally zirconium knifes are used to cut fibres in order to get a clean cut. There are no zirconium knifes at IFT, and it is unknown if there are anything of equal sharpness at IFT.

- Positioning the fibre a few tens of μm above the MPPC, and keeping a consistent distance throughout a scan.

- Getting a clear view of the MPPC from the microscope for positioning while a fibre is mounted right above it.

- Getting enough light through a single-mode fibre in order to trigger a single pixel often enough to get good statistics.

4.2.3   Focus light through microscope

The oculars have seldom been used to inspect or position the MPPCs before scan. All of this is done through the camera, and since the left ocular is always open, a flash of light can be focused through the microscope and onto the MPPC to trigger the pixels.

To do this a mounting device, called the fibre mount, was built to hold a fibre directly above the left ocular. The fibre mount is shown in figure 4.7. The fibre mount house has two pairs of screws. The lower pair is used to hold the ocular tightly when inserted into the wide opening of the house. The upper pair is used to hold the rod when inserted into the narrow opening of the fibre mount house. The rod consists of two parts; the rod itself and the rod-base. The rod-base has threads in its centre hole, for holding the ST-coupler in place. When assembled, the fibre is fixed at the end of the rod, and the rod can be positioned at a wanted elevation relative to the ocular inside the house. Like this the rod is positioned at the elevation where the light from the fibre is focused through the microscope onto a single MPPC pixel.

As discussed earlier, vibrations in the XY-table will most likely affect the microscope, which again will affect the position of the light flash. The most severe effect is that vibrations can displace the point where the flash hits by a few tens of μm. This can make the flash hit the neighbouring pixel or in between pixels.

The fibre

The fibre mounted to the microscope is a standard multi-mode fibre with a 50 μm radius and a ST-connector. The fibre has a high luminosity blue LED connected to its other end, outside the cabinet. Blue light was used since the MPPC has a maximum quantum efficiency at these wavelengths. The LED can either be connected to a fast pulser or a power supply.

During measurements of the MPPCs the LED is connected to a fast pulser, built by Njål Brekke. The pulser is triggered on the falling edge of a step function provided by a signal generator. The pulse from the pulser has a full width at half maximum of 0.8 ns, the LED then emits a few photons.

When the LED is connected to the pulser it does not emit enough light to be seen through the microscope. In order to focus the LED light and to position it correctly the LED is connected to a power supply. The Z-stage is used to focus both the image of the pixels and the LED light coming though the microscope. An image of the focused LED light through the microscope is shown in figure 4.8, and the finished XY-table setup is shown in figure 4.9.
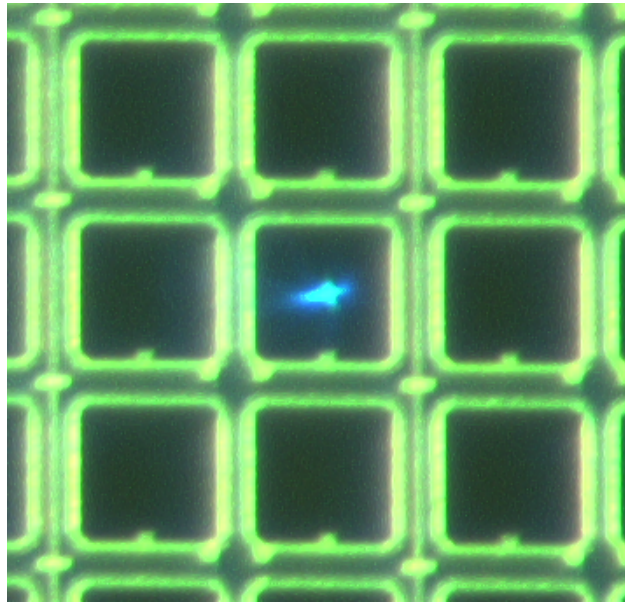
Figure 4.8: Image of the blue LED light shining through the microscope and onto a single MPPC pixel.

4.3   Positioning software

LabVIEW was used to create all the programmes that control the XY-table. LabVIEW has more than enough resources to control the XY-table, and because it has no need for compilation and a graphical interface it is very easy to use.

The columns and rows of the MPPC pixels will never be perfectly aligned with the X- and Y-axis of the XY-table. The MPPC will also never be perfectly horizontal, and since the image of the MPPC and the flash light goes severely out of focus when elevated or lowered about 0.3mm the Z-axis must correct the elevation during scan.

To fix this a simple 3×3 transform matrix, $\mathbb{A}$, can be implemented that should correct for an uneven placement of the MPPC:

$$\mathbb{A}\mathbf{x}'_{1,2} = \mathbf{x}_{1,2}, \tag{4.1}$$

where $\mathbf{x}'_{1,2}$ is the input vector and $\mathbf{x}_{1,2}$ is the output vector. The input vector is the coordinates the user of the program uses to find the wanted pixel, whereas the output vector is the actual coordinates sent to the XY-table controller.

The transform matrix is built by two vectors which forms a base for the new coordinate system. This base can be found by the vectors from the upper left pixel to both the upper right and the lower left pixel. This is illustrated in figure 4.10.

Figure 4.9: A photo of the finished XY-table setup.

Figure 4.10: The two vectors that spans out the transform matrix.

A LabVIEW program that makes use of a transform matrix was developed. First it demands the user to focus the LED light on the centre of the upper left pixel and select this as the origin.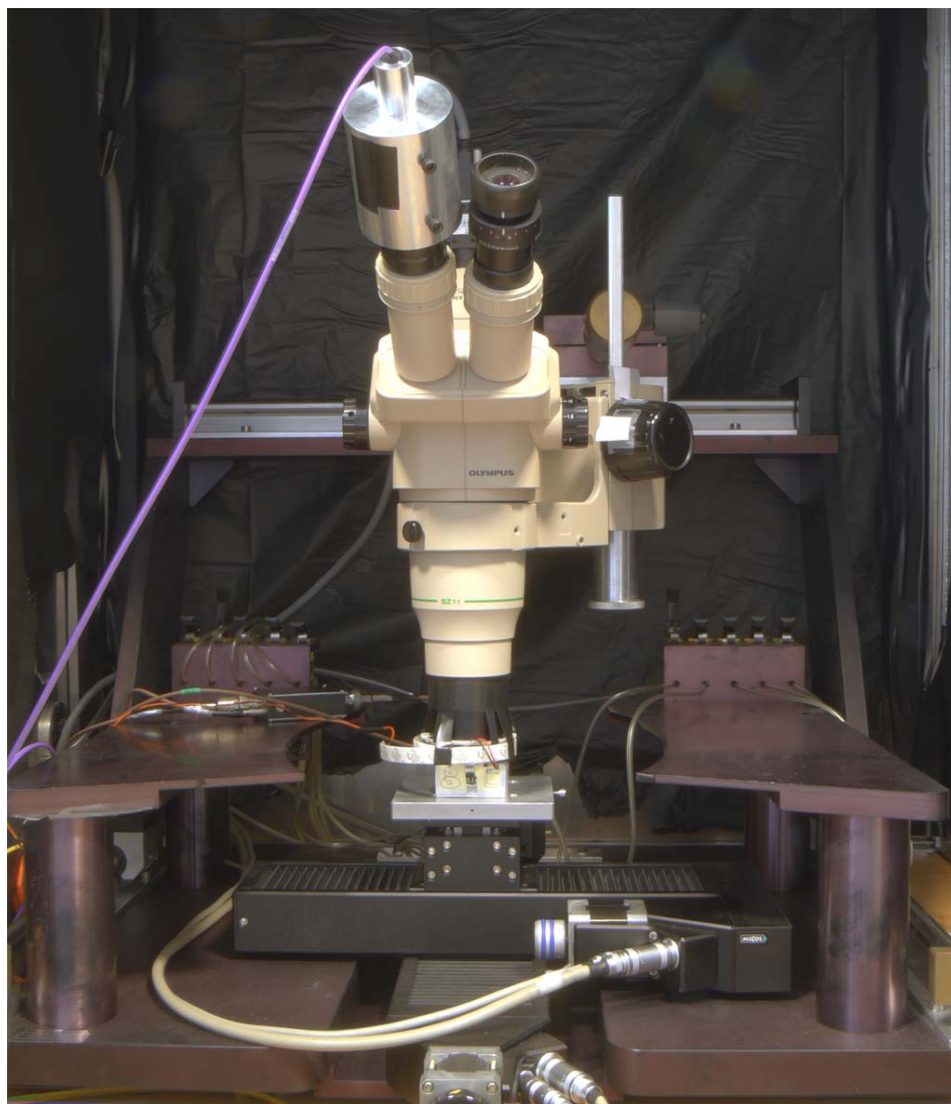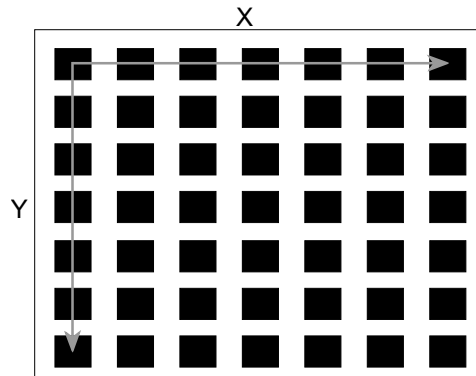 Then the user has to find and store the coordinates given by the motor controller of the upper right and the lower left pixel. It is important that the Z-stage is used to focus the LED light on all these coordinate so that the output vector has the correct Z-value. The user also has to enter the amount of pixels in each row and column. The program then makes a new two dimensional coordinate system where the coordinates x and y are integers in a matrix of pixels and the Z-stage automatically focuses the pixels. For example, if the MPPC consists of 60×60 pixels the corners would have the coordinates (0,0),(60,0),(0,60) and (60,60) in this new, transformed coordinate system.

The new coordinate system should find the centre of all the pixels on the MPPC. When moving the MPPC such that the LED light passes along the first row of the MPPC of a 3×3 mm^2, 60×60 pixel MPPC, from (0,0) to (60,0), the light oscillates around the centre of the pixels. It hits the centre of the pixel at the coordinates (0,0), (20,0), (40,0) and (60,0), and is furthest off in between these positions. The distance between these positions are 1 mm, which is the same distance the stage travels after one revolution of the stage's screw bolt. This leads to the assumption that the screw bolts are uneven and the program described above can not be used to locate all the pixels on a MPPC. The same happens with the Y stage.

An attempt was made to correct for this in software by adding sinus parts in the equation that should correct for the oscillation, but this approach was abandoned after several failures.

Even though this program did not work, the transform matrix is still used so the that the detector does not have to be perfectly aligned with the stages for optimal performance. The transform matrix sort of aligns the detector in software.

4.3.1 Pattern matching

Even though the program that solely depended on the transform matrix was not precise enough to find all the pixels it showed that the same coordinates hit the same place every time. This indicated that the repeatability was good enough to find back to a given pixel if its coordinate was stored in memory.

To find the correct coordinates of all the pixels a new program which automatically found all the pixels had to be developed. The only way to do this was through pattern matching. Three programs where made. The first positions the detector and creates a transform matrix that aligns the detector. The second uses pattern matching to create a lookup table of the pixels coordinates. The third verifies that the lookup table coordinates finds the centre of the pixels.

Position Flash.vi

This program is used to position the detector and creates a transform matrix. The first thing that should be done is to rotate the camera on the microscope so that the image is aligned with the MPPC. The reason for this is that upwards on the image given by the camera is also upwards in the new coordinate system given by the transform matrix. This is needed for the pattern matching sequence in "Place Coordinates.vi" described below. The user focuses the LED light at the upper left MPPC pixel, and selects it as origin. Then the "flash point" is set at the centre of the LED light. The flash point is now the camera pixel[6] where the LED light hits when it is in focus, and it is marked as a red pixel on the screen. The user then finds the upper right and lower left corner and focuses the LED light such that the flash point chosen coincides with the LED light, and stores the X- and Y-base respectively. These vector bases makes out the transform matrix. The front panel of this program is shown in figure 4.11.

When the bases have been found the program is closed, and the bases and the flash point are written to file.

Place Coordinates.vi

After the bases of the MPPC pixel matrix is found with "Position Flash.vi" the positions of the individual pixels must be determined. Place Coordinates.vi uses pattern matching in order to find the centre of the pixels and write their coordinates to file, creating a lookup table of the pixels coordinates. There are actually two of these programs, one for the 25C MPPC and one for the 50C. The differences are minor and are not of consequence when describing the programs.

---

[6]Not to be confused with a MPPC pixel. The camera has 1288×964 pixels.
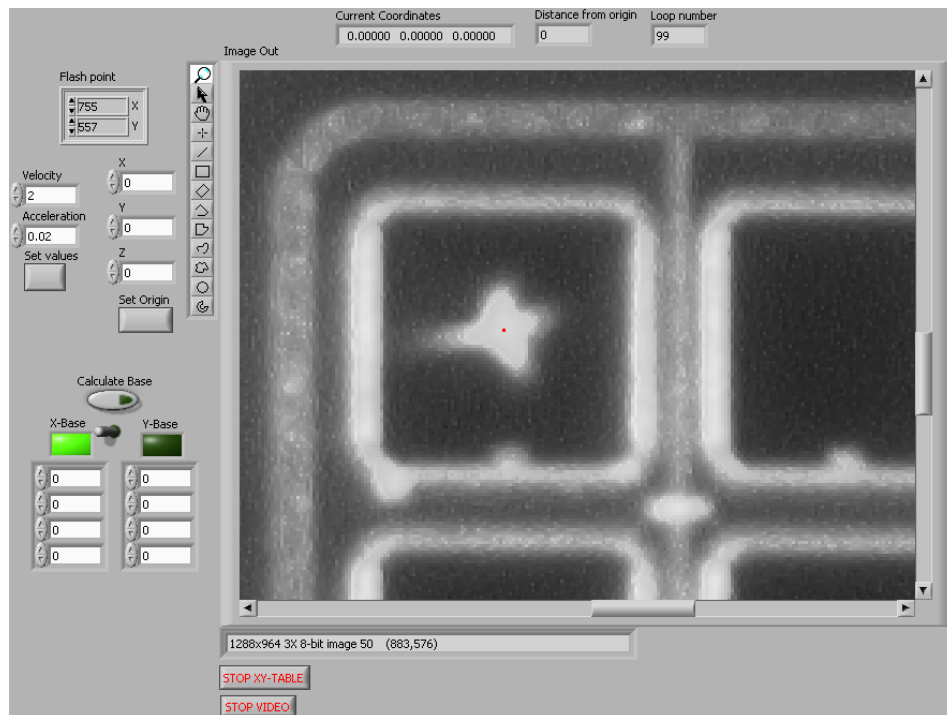
Figure 4.11: The front panel of the "Position Flash.vi". The little red dot is positioned at the centre of the LED light, marking its position for later use. The vectors forming the base of the transformed coordinate system are calculated by pressing "Calculate Base" when the LED light is positioned at the upper right corner (X-base) and lower left corner (Y-base). The light should be focused such that the flash point is at the centre of the LED light.
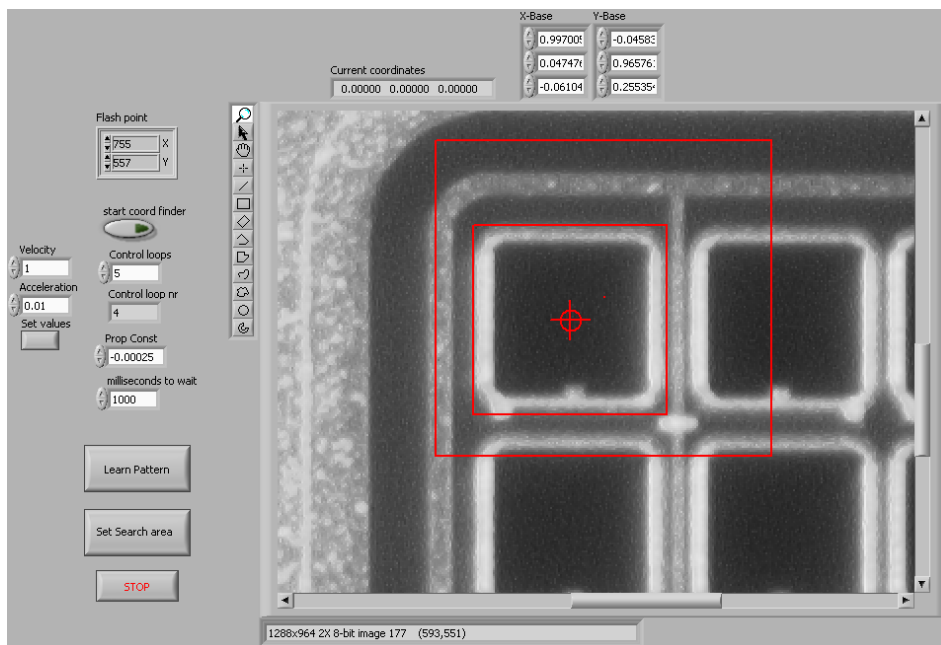
Figure 4.12: The front panel of the "Place Coordinates.vi". The outer red square in the camera window is the search area, while the smaller red square with a cross is a recognised pixel. The small, red dot is the flash point, it represents where the LED light will hit.

When running "Place Coordinate.vi" the LED light is turned off since the light would disturb the pattern matching sequence. Both the flash point and the bases previously written to file by "Position Flash.vi" are read as soon as the program starts. The flash point now indicates where the LED light will hit and should be near the centre of the upper left pixel which is selected as origin.

The user starts by drawing a square stretching well over the upper left pixel, where the flash point is, and presses "set search area". A red square will then appear. The "search area" square size should not be bigger than 2×2 pixels, and the flash point should be at its centre.

Then the user draws a new square which only covers the upper left pixel, and presses "Learn Pattern". The program has now memorised the image of the pixel, and will draw a red square around the recognised pixel with a cross in the middle of it. The program only searches for matching patterns inside the bigger "search area" square. The front panel of this program is shown in figure 4.12.

When the user now presses the "start coord finder" the program will start to move the XY-table such that the centre of the recognised pixel will move towards the flash point. This movement is done by a simple proportional controller, and without the transform matrix the movement would not have been in the right direction unless the MPPC was perfectly aligned with the stages. The controller moves the pixel-centre towards the flash point in five steps, and write down the coordinates of its current position, which should be near or at the flash point. The XY-table then moves over to the neighbouring pixel, and repeats the sequence. Without a transform matrix the program would not have known which direction the neighbouring pixel was. If the "search area" square is too big it can at some point contain two pixels giving two matching patterns. This is a problem for the controller and is avoided by using a smaller search area.

This way it finds the coordinate of all the pixels. When all the coordinates have been found the program stops.

Find Coordinates.vi

The "Find Coordinates.vi" is used to verify if the coordinates in the lookup table positions the MPPC pixels directly under the LED light. The LED is powered by the power supply, and the program goes through all the coordinates of the lookup table. The program shows where the LED light hits for each coordinate given so the user can determine if the coordinates are accurate enough.
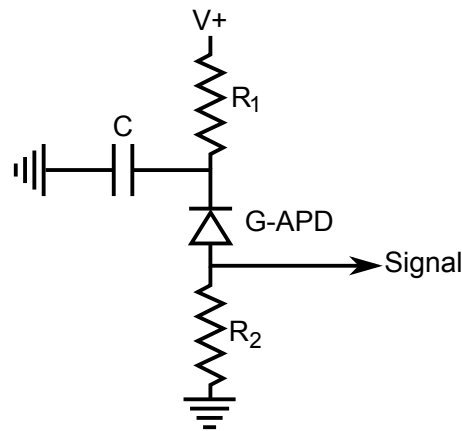
Figure 4.13: A general readout circuit for G-APDs.

4.4 Data acquisition system

The data acquisition system (DAQ) is more or less the same as used by Hege A. Erdal in her master thesis (1), where she determined characteristics of G-APDs. The LabVIEW programs she used were mostly made by Ph.D. student Njål Brekke. The Gain program written by Njål Brekke is used to gather data when the MPPC is triggered during measurement.

4.4.1 Readout circuit

The readout circuit for the MPPCs is shown in figure 4.13. The capacitor and the impedance R_1 works as a low pass filter that removes high frequency noise and ripple from the power supply, V+. The signal emitted from the MPPC is a charge which is read out as a voltage over R_2. After the signal leaves the MPPC it enters a fast preamplifier[7] with an internal impedance of 50 Ω. The impedance of R_2 is also 50 Ω, to match that of the preamplifier. The readout electronics is placed inside an aluminium box, the readout box, to avoid noise from surrounding electronics. The MPPC is attached to the readout box, and the readout box is fasten to the detector chuck. To avoid any serious distortion of the signal the preamplifier has a bandwidth of 100 kHz - 1.5 GHz.

4.4.2 DAQ

The entire experimental setup is illustrated in 4.14 and explained below:

- The LED pulser is precharged to 13-15 V by a power supply[8] which also powers the preamplifier with its 12 V.

---

[7]Philips scientific wide band amplifier, model 6954.
[8]TTi QL355TP power supply.
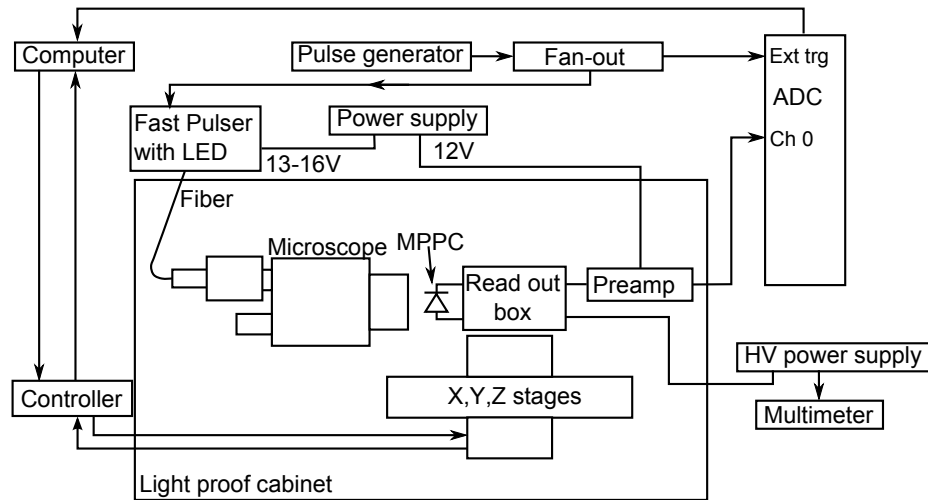
Figure 4.14: Schematic view of the experimental setup and its data flow.

- A power supply[9] sets the bias voltage over the MPPC to ~ 70 V. A multimeter[10] is used to find the real value.

- The signal generator[11] generates a 2000 kHz step signal with a 5 ns rise- and fall-time. The signal goes into a fan-out that distributes the same signal to both the external trigger on the ADC[12] and the LED pulser.

- On the falling edge of the step signal the pulser emits a few photons which are focused through the microscope onto the MPPC. The amount of photons emitted depends on the voltage supplied to the pulser.

- The MPPC outputs a charge signal which is read out as a voltage over a resistance. The voltage signal is amplified in the preamplifier, and sent to the ADC.

The LED emits a light flash every time it receives a pulse from the signal generator, but the ADC only reads out the resulting charge if it is ready. This means that only a fraction of the output from the MPPC is measured when it is triggered. The signal generator is not controlled by the computer and will send pulses continuously.

---

[9]Keithley 487 Picoammeter/Voltage Source.
[10]Keithley 2100 6 1/2 digital multimeter.
[11]Agilent 33250A - 80 MHz Function/ Arbitrary Waveform Generator.
[12]CAEN 4 Ch, 14 bit, 2 GHz ADC, model V1729A.

4.4.3 Gathering data

The program that does the MPPC measurements positions a pixel where the flash from the LED light will hit by use of the lookup table. Since the signal generator continuously sends pulses to the LED pulser, the LED will send light flashes at a constant rate. This leads to an avalanche within the pixel every time a photon is absorbed. The avalanche releases a charge which gives a voltage pulse over R_2. The voltage pulse is amplified by the preamplifier and sent to channel 0 on the ADC.

The ADC is a 2 GHz oversampling ADC. It continuously receives signals from the readout electronics and stores it in an analogue buffer memory When the signal generator sends a signal to the LED pulser it also sends a signal to the external trigger on the ADC. Whenever the ADC is triggered it reads out whatever signal is on channel 0 and sets the time it was triggered as t = 0. The ADC then sends the digitalised signal to the computer which is 1000 ns broad about t = 0. When the ADC digitalizes a signal it is busy, and will not start to digitalize a new signal even if it is triggered. This is the slowest part of the system.

The measurement program receives the signals from the ADC and plots them in two histograms. One of the histograms show the entire signal given by the ADC while the second histogram is defined by the user and will be explained further. The avalanche signal from the MPPC is about 50 ns long and should be located near t = 0 since the LED pulser and ADC it triggered at the same time. The second histogram in the program has a width and offset that can be adjusted by the user. This histogram should contain the entire avalanche signal from the MPPC and nothing more. The user can select the offset and width of the second histogram while measurements are running. The width and offset of the avalanche signal depends on the readout electronics and the detector. One of the detectors used in this thesis had a width of 50 ns and an offset of -17 ns during all the measurements. The signal that enters the second histogram is integrated, and the integrated signal is proportional to the charge emitted by the MPPC. The integrated signal is written to file.

The ADC does several thousand measurements for each pixel and all are written to file.

Chapter 5

Performance of the XY-table

The first LabVIEW program that made use of the transform matrix showed that there was either something wrong with the distance between the MPPC pixels or the stages were faulty. It was assumed that the fault lies in the stages since the distance between pixels seem to be consistent on the images captured by the camera. This chapter also shows the faulty stepping of the stages.

5.1   Intrinsic positioning performance

To test the overall performance of the XY-table a calibration grid was used. The grid has 1.5 μm thick lines with 10 μm spacing, and is shown in figure 5.1. The grid has black lines on milky white opaque glass.

   The grid was carefully aligned along the X- and Y- stages before commencing any measurements. A red dot was placed on screen, in the same way as the flash point. The red dot will always be on the same place on the camera image, and it is used as a reference of how much the grid moves relative to the camera. The red dot is therefore called the *reference point*.
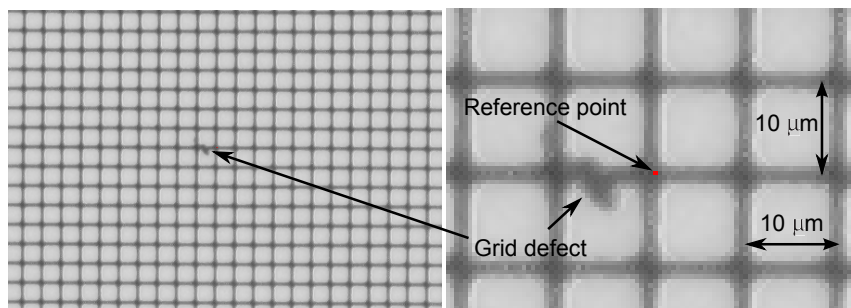

Figure 5.1: Picture of the target grid. The reference point (red pixel) was positioned close to a defect in the grid, this was also selected to be origin.

To check the alignment of the grid the joystick was used to scroll along the X- and Y-axis while seeing if the reference point followed the grid lines or went across them. When the grid had been reasonably adjusted it was noticed that the XY table had small, sudden increases inn Y-direction when scrolling along X. When scrolling back the Y seemed to decrease back the same way it earlier increased, implying that it was a systematic and not a random error. This did not happen when scrolling along the Y-axis.

In order to read distances on the MPPC and the grid the ratio between the screen/image pixels and the distance in reality had to be found. This was done by spanning out a rectangle on screen and find its size in image pixels and comparing it to the grid on screen. When the rectangle spanned over 250 μm by 210 μm on the grid the rectangle was 518 pixels by 442 pixels. This shows that 1 μm in reality equals 2.1 images pixels in X- and Y-direction.

The depth of the microscope focus is quite small i.e. a small change in the distance between microscope and grid causes the grid to become unfocused. When the grid is perfectly focused one can change the Z-elevation by +/- 0.1 mm and it will still be quite clear, but a bit unfocused. When elevating the Z-stage by 0.2 mm the reference point moved $\sim$ 7 μm in X-direction.

To get a better understanding of how the XY-table stepped incorrectly two types of test were applied with the grid; a reproducibility test and a distance test.

5.1.1   Reproducibility

The reproducibility was tested by positioning the reference point at a cross point in the grid and selecting it as origin. A cross point next to a small defect in the grid was selected as origin to not get lost in an identical grid. A LabVIEW program then moved the grid along one axis a given distance, and then back to origin. The grid went back and forth like this and an image was taken every tenth or fiftieth time it was at origin. This way it would be seen how the reference point would move relative to the cross point. Five sets of images were made, two along the X- and Y-axis and one along the Z-axis. Along the X- and Y-axis a long test were performed, where the stages went forth and back 5mm; and a short test where the stages went back and forth 20 μm. 1000 measurements were done in the long test and 5000 in the short test. Images where taken every tenth time in the long test and every fiftieth time in the short test, resulting in 101 images per test. In the Z-stage test the Z-stage was elevated 3mm and then back to origin again 1000 times with an image every tenth time. To present these images 12 of the 100 images from each test were selected and the grid from each of the images where put on top of each other while the reference point shined through them. This way one can see the reference point moving relative to the grid. This is shown in figure 5.2 and presented in table 5.1.
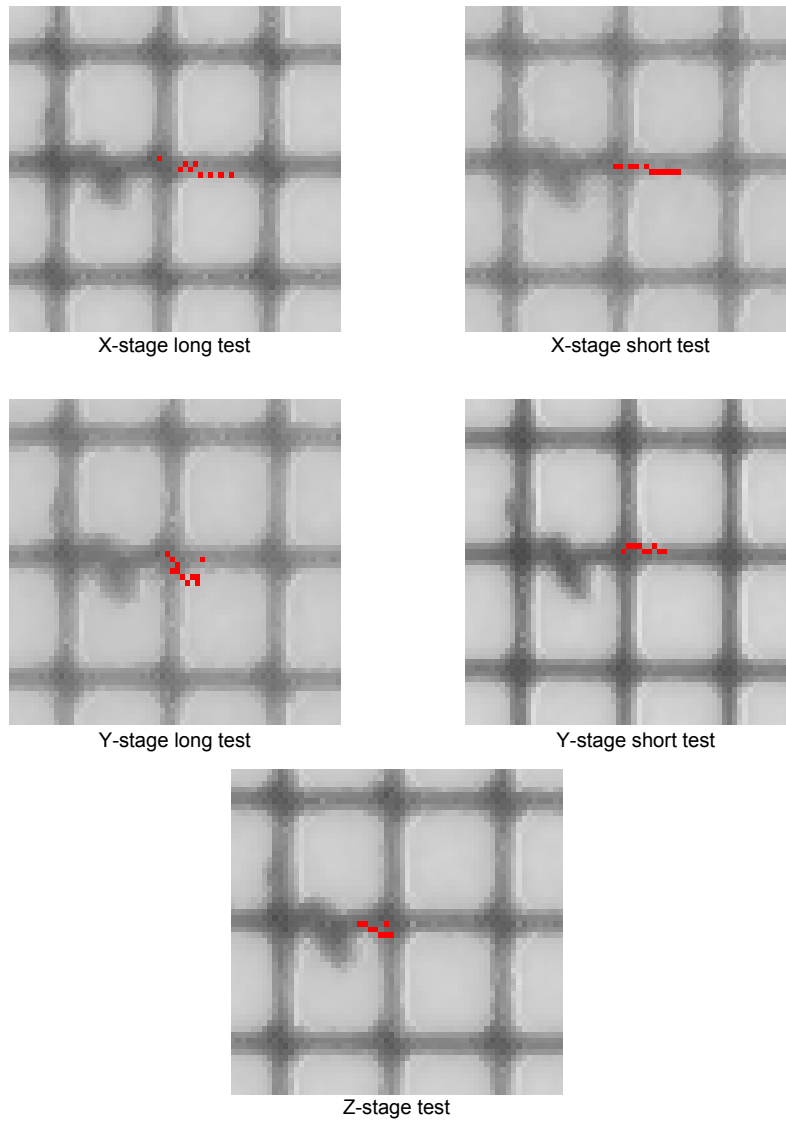
Figure 5.2: The repeatability test of the XY table. The stages has moved forth and back from origin a number of times, and images has been taken at origin to see how the reference point moves relative to the grid. (note :table ref)

Table 5.1: The deviation show how much the reference point has moved relative to the grid at the end of the reproducibility measurements. The X- and Y-deviation are given in μm while the distance and Z-deviation is given in mm.

Test	Distance	Repetitions	X-deviation	Y-deviation	Z-deviation
X-long	5.00 mm	1000	7.5 μm	1.5 μm	0 mm
X-short	0.02 mm	5000	6.5 μm	0.5 μm	0 mm
Y-long	5.00 mm	1000	0 μm	3 μm	-0.1 mm
Y-short	0.02 mm	5000	0 μm	0 μm	-0.1 mm
Z	3.00 mm	1000	μm um	-1 μm	-0.1 mm

The relative movement of the reference point and the grid in table 5.1 is read from the images taken. The Z-deviation was found by refocusing the image by adjusting the Z-stage after the sets of measurements were taken. The Z-deviation is very uncertain since it relies on when the image is in focus, and is therefore given in mm range. The Z-deviation is also given by the motor controller which gives erroneous position information as will be seen in the next section. The position error given by the motor controller is in the μm range for the X- and Y-stages. If it is the same for the Z-stage the motor controller gives good enough information in mm range. Movement in the Z-direction also moves the grid in the X-direction which also had to be taken into account when making the table. From the table it can be seen that the Y- and Z-stages adjust the Z-stages over time, but not the X-stage. The X-stage is however the stage with the worst reproducibility in the XY-plane, seen by the a rather large shift in X-direction.

5.1.2   Distance

The biggest problem with the XY-table is that the stages does not seem to move the distance given to the motor controller. Both the X- and Y-stages were tested by moving the grid 50 μm at a time and reading the position given by the controller each 50 μm for 3mm. Since a pattern emerged for every mm a second plot was made by moving the grid 20 μm a time for one mm. The difference in position from the motor controller and the one measured by the grid is plotted along the X-axis, and the distance travelled according to the grid, the real distance, is plotted along the Y-axis in figure 5.3 and 5.4.

The plots show two components; the axis oscillates around the real value, and there is a steady increase in the motor controller position relative to the real position. The oscillating part was described in section 4.3 in relation with the first transform matrix program made. This might originate from an uneven screw bolt that drives the stage carriage. It can also be an error in the motor controller, but this is doubtful.
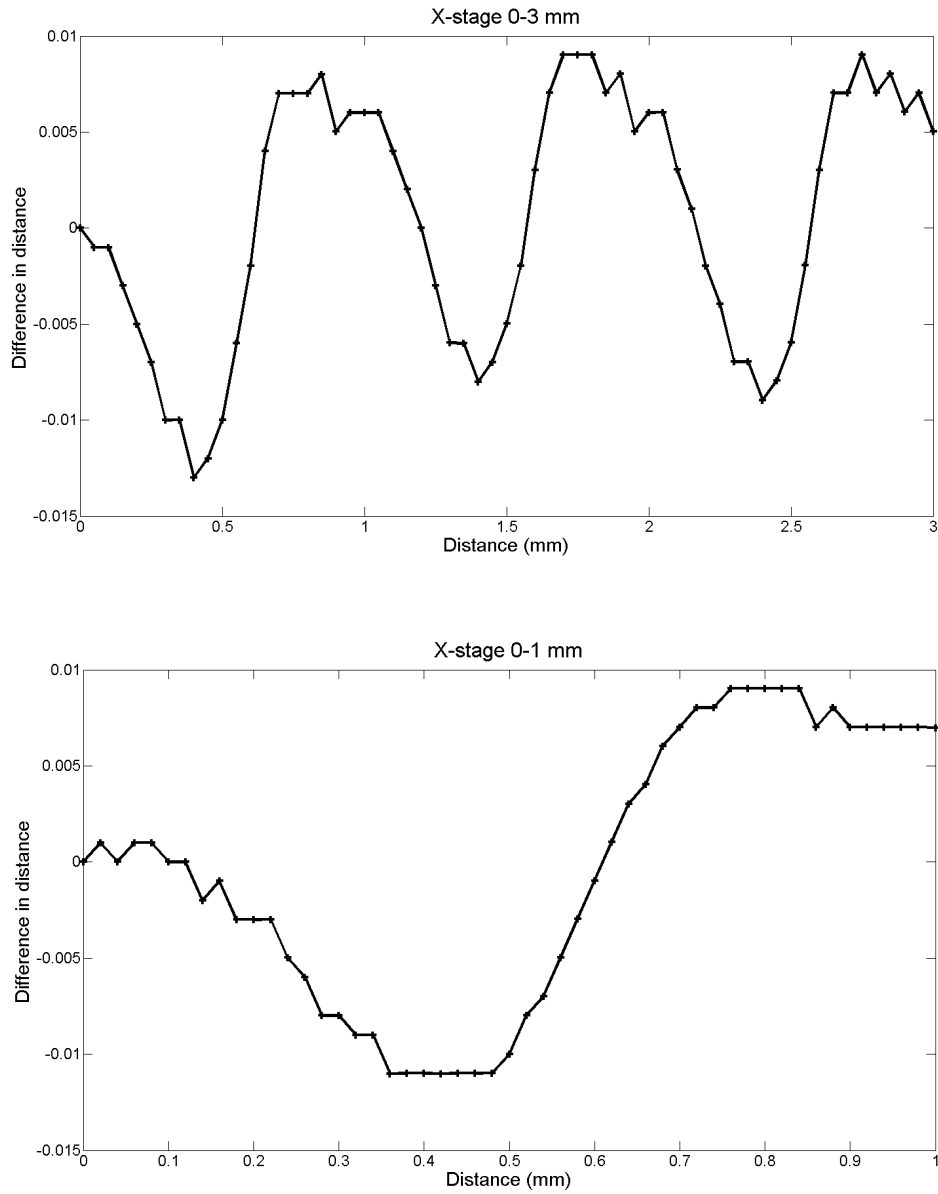
Figure 5.3: Controller distance vs. grid distance (real distance).
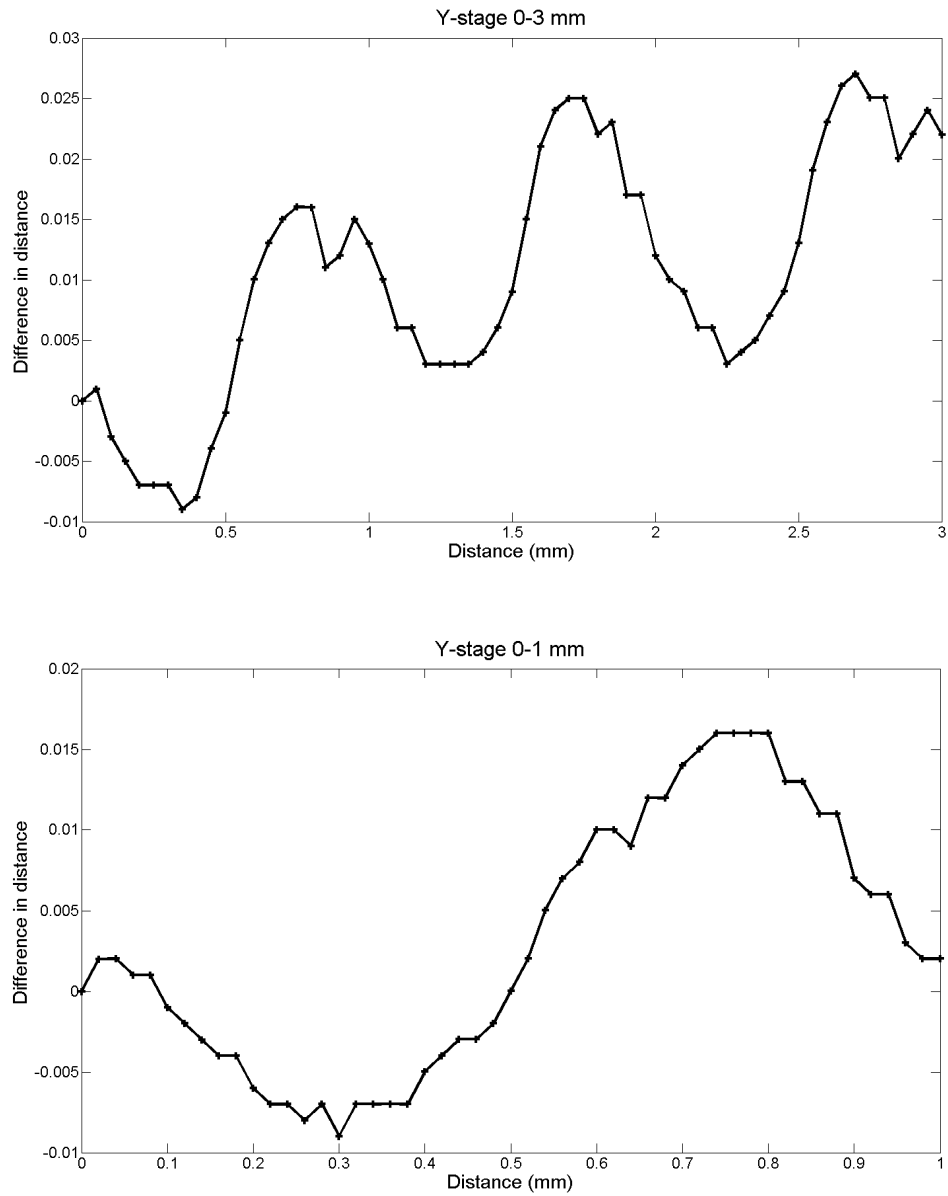
Figure 5.4: Controller distance vs. grid distance (real distance).

The steady increase in the position given by the motor controller has currently no explanation. The X-position increases by about 1.7 μm per mm travelled, while the Y-position increases about 7 μm per mm travelled.

These measurements make it clear that any form of linear transform matrix can not be used alone to locate the MPPC pixels.

5.2 Calibration

Since any linear transform matrix cannot locate the MPPC pixels correctly pattern recognition was used to create a lookup table of coordinates for the MPPC pixels. In the program "Place Coordinates.vi" there is a proportional controller that finds the coordinate to the pixel centre. The amount of steps the controller uses to find the pixel centre can be changed on the front panel. The more steps the controller takes the more accurate it finds the centre. As seen by the reproducibility test many steps can make the entire coordinate system shift. Too many steps from the controller might therefore shift the coordinate system during the pattern recognition routine. This could make the first coordinates in the lookup table miss the MPPC pixel while the last would hit correctly.

To test the accuracy of the lookup table two sets of coordinates were found on a 25C MPPC. One where the proportional controller made 5 steps and one where it made 15 steps. There is no point using more then 15 steps since it will not find the pixel centre more precise. The 25C MPPC was chosen since it has the smallest pixels, making it easier to see any deviation. It took 25 minutes to create the lookup table with 5 control steps, and 62 minutes with 15 control steps.

After the lookup tables were found the program "Find Coordinates.vi" moved the MPPC through the coordinates while the LED light shined on the pixels. The LED light hit each of the MPPC pixel as accurately in the 5 step coordinate set as in the 15 step set. Three images where taken from each run showing how the LED hit at the first, middle and bottom column. They are shown in figure 5.5.

5.3 Initiation procedure

After the first few measurements were analysed two anomalies where discovered. The LED light hitting the pixel had sometimes moved relative to the MPPC during measurements, drift, and the peaks in the plots generated moved from pixel to pixel.
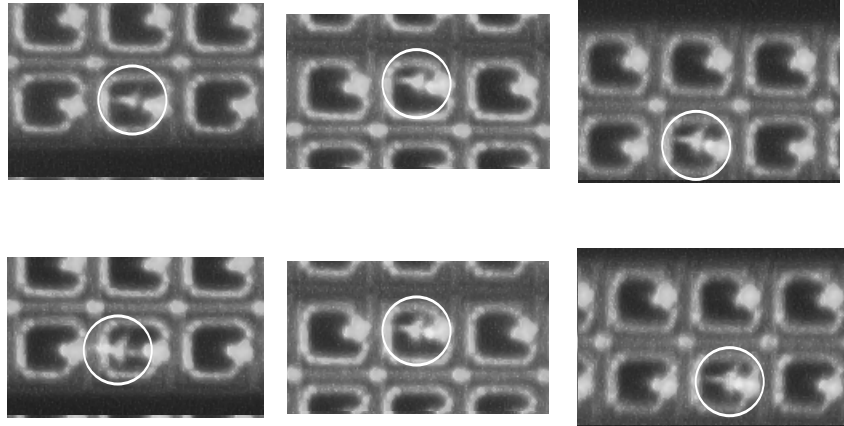
Figure 5.5: Images that shows how well the LED light hit after the coordinate have been found. The top line is after 5 control steps and the lower is after 15 steps. The images are representative of how well the LED light hits the pixels throughout the MPPC.

5.3.1 Drift

When either the MPPC or the fibre mount had recently been adjusted before test it often resulted in a movement of the LED light relative to the MPPC during scan. It was noticed that right after the coordinates had been mapped out the LED hit the correct pixel. It had, however, shifted during testing, such that the coordinates did not place the LED light at the correct coordinates after testing. This might be because the fibre mount and the MPPC where slowly "falling" into their lowest position. After this was observed the equipment got to rest for one till two hours before commencing a test.

5.3.2 Peak shift

When no avalanche is present at the MPPC, and the DAQ gathers data from the readout electronics the signal will be as shown in figure 5.6. This peak is called the *pedestal peak*. It is the integrated noise from the readout electronics and is distributed as a Gaussian. The pedestal peak marks the channel number when no signal is detected. Other peaks that comes when the MPPC is triggered are calculated relative to the pedestal peak.

When the first measurements of the 50C MPPC were taken it was noticed that the peaks in the histogram shifted as the MPPC test went on. In some measurements the first few pixels the pedestal peak where centred around channel number 1000, then it gradually sank down to channel number -1000. The other peaks also shifted such that the distance between peaks were approximately the same. When it had measured about 30 pixels the
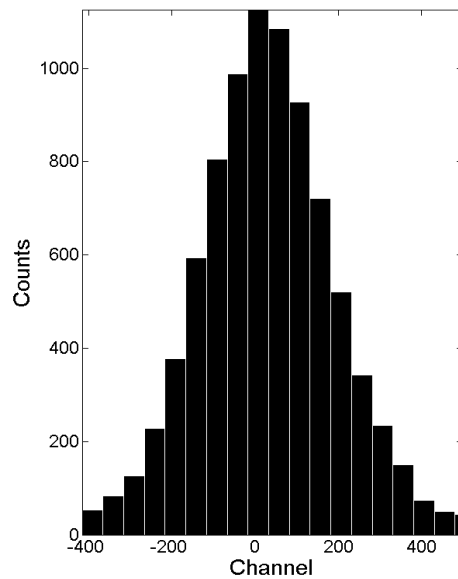
Figure 5.6: The integrated signal when no avalanches takes place in a MPPC, referred to as the pedestal peak.

pedestal peak where centred around -1000 throughout the test.

First it was assumed that this was because the MPPC had not been left in the dark long enough before the test was initiated. Several of the traps between the conduction and valence band would then be filled, and this would lead to noise in the first measurements that could move the peaks to higher then normal channel numbers. The MPPC was then left in the dark with applied bias voltage for 30 minutes in an attempt to remove the peak shift. The result was that the pedestal peak started at about 0 and moved down to -1000 after a few pixels; leaving the MPPC in the dark was half the solution. To get the other half correct the preamplifier also had to be powered a while before commencing a test. The reason for this is unknown.

Before a test is ran the MPPC is biased and left in the dark, and the preamplifier is powered up. The MPPC and preamplifier stays like this for 20 minutes before the test commences. This ensures that the pedestal peak do not move considerably during testing.

Chapter 6

Results

After the "Place Coordinates.VI" has mapped out the coordinates of all the pixels, the LED is powered by the power supply. The program "Find Coordinates.VI" then moves the XY-table to all the coordinates previously written to file. The camera now shows if the LED light hits the correct MPPC pixel or not, as a preliminary indication whether the correct pixel will be pulsed during testing. Two detectors has been tested here, the MPPC S10362-33-050C serial number 339, referred to as the 50C and the MPPC S10362-11-025C serial number 739, referred to as the 25C.

When testing the 50C, which has 60×60 pixels and about $50 \times 50 \mu\text{m}^2$ pixel size, the LED light has normally drifted a bit off the pixel centre during test. This is not a problem since the pixels are so large that the entire LED light is contained within one pixel, as shown in figure 4.8.

When testing the 25C, which has 40×40 pixels and about $25 \times 25 \mu\text{m}^2$ pixel size, the LED light will often not be entirely contained within one pixel. Even though the LED light is not contained within one pixel, it will seldom hit the neighbouring pixel. If the neighbouring pixel should be triggered once in a while during testing it will not likely be a problem.

6.1 Measurements

When the microscope is set to a minimum zoom, and somewhat unfocused, the LED light will hit several pixels on the MPPC. At the top of figure 6.1 a plot where several pixels has been hit is shown. The histogram contains several peaks. The first peak is the charge when no pixels are triggered; the integrated signal when no avalanche takes place in the MPPC. It is called the *pedestal peak*. The second one is the first photon peak (1.p.e.) and represent the charge emitted when one pixel is triggered. The third peak is when two pixels are triggered, and so on. The mean charge emitted by one breakdown event in a single pixel is the mean charge difference between these peaks. The top figure with the multiple peaks has 1 000 000 measurements, which
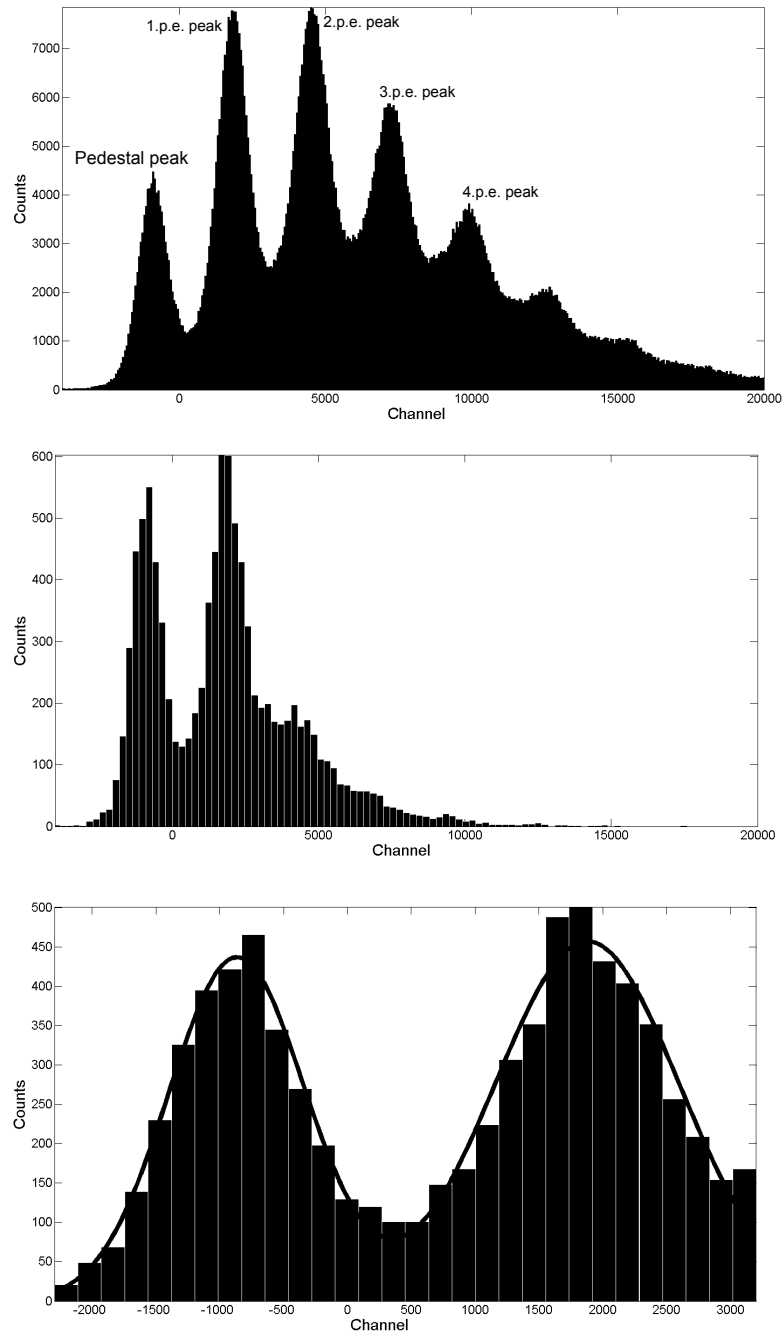
Figure 6.1: Top: Histogram of several hit pixels. Middle: Single pixels triggered. Bottom: Single pixel triggered; the X-range is narrower, and a double Gaussian curve fitting is applied. The ADC channel number along X is proportional to the charge emitted. The middle and bottom histogram is based on the same data. The three histograms are from the 50C MPPC.

gives quite a good resolution. The measurements took about 25 minutes.

The middle histogram in figure 6.1 is a plot when the flash hits only one pixel. The bottom histogram is of the same data as the middle one, but with a more narrow charge range, and an applied Gaussian curve fitting. The gain from a single pixel plot is the difference in channel number from the 1.p.e. peak and the pedestal peak.

10 000 measurements were used to create the middle and the bottom histograms, which takes about 16 s. This obviously gives a lower resolution than the top histogram, and a more uncertain curve fitting. Seeing that there are 60×60 pixels in the 50C MPPCs it takes about 16 hours to finish testing of the entire MPPC. 16 hours is convenient in the way when the test can be started at 16:00, and finished at 08:00 the next day. This way vibrations are avoided by avoiding common work hours at IFT.

6.1.1   Noise

The width of the peaks gives the noise in the system. The pedestal peak width is generally only dependant on the noise in the readout electronics. This is true if no avalanche signal is present in the integration window at all. But due to the extensive dark rate, specially for the 50C, there will occasionally be starting and ending avalanche signals in the integration window that will widen the pedestal peak. Since the 50C has over an order of magnitude more dark rate than the 25C (1), and a larger integration window the pedestal peak is wider for the 50C than the 25C. The pedestal peak width is more or less the same for all the measurements in the 25C, and in the 50C. The pedestal std. of the 25C is typically 150 ADC counts, while it is a little over 500 for the 50C.

The width of the 1.p.e. peak is a combination of any variation in the charge output from the MPPC and the noise in the DAQ system, quantified by the pedestal peak. The charge output standard deviation (std.) from the MPPC can be calculated from the following formula:

$$\sigma_{charge} = \sqrt{\sigma_{1.p.e.} - \sigma_{pedestal}} \tag{6.1}$$

Where $\sigma_{1.p.e.}$ is the std. of the 1.p.e. curve and the $\sigma_{pedestal}$ is the std. of the pedestal peak. Gaussian fits for a for both a 25C and a 50C pixel is shown in figure 6.2. The 1.p.e. curve std. is about 3-4 times higher in the 50C than in the 25C.

6.1.2   1.p.e. curve height

The ratio of the area under the pedestal peak and the area under the 1.p.e. peak is proportional to the probability that the MPPC is triggered when the LED is pulsed. Since the position and the std. of the two peaks vary

little the height of the curves is strongly correlated to the number of times the pixel has been triggered from the 10 000 measurements.

The height of the curve depends on the probability that the pixel is triggered each time the LED is pulsed. As mentioned earlier, the voltage supplied to the LED pulser decides how many photons that are emitted from the LED each time it is pulsed. The amount of photons that hit the surface of the MPPC pixel depends on pulser voltage, LED position with respect to fibre entrance, attenuation through the microscope and the microscope focus. During measurement all these parameters are considered static, and it is therefore assumed that the same amount of photons hits the MPPC surface each measurement. There are several reasons why some pixels can get fewer counts:

- The LED light might fall partly inside a pixel and partly on the dead area between the pixels.

- The surface above the pixels might be dirty and let less light pass through.

- The PDE might be lower for some pixels.

The 25C MPPC seems to have a larger variation in the 1.p.e. peak height than the 50C. This is probably because the LED light can easily miss part of the pixels, due to their small size.

6.1.3 Uniformity of the MPPC

When all the pixels in the MPPC has been measured the gain, 1.p.e. std. and 1.p.e. curve height is found through a Gaussian fit for each pixel. Three matrices are then built, containing:

- The gain.

- The std. of the 1.p.e. curve.

- The height of the 1.p.e. curve.

The data is placed within the matrices such that the rows and columns of the matrix corresponds to the rows and columns of the MPPC. This way the upper left pixel on the MPPC is has the matrix indexes [1,1].

The matrices are plotted in 2 dimensional histograms such that the height of the bars represent the value of the pixels. The bars are also color coded from blue to red, representing low to high value. Typical plots of both 25C and 50C MPPCs are shown in figure 6.3 and 6.4. Slices of the first and middle, rows and columns are these are shown in 6.5, 6.6 and 6.7. The mean, maximum and minimum of the data used in figures 6.3 and 6.4 are shown in table 6.1.
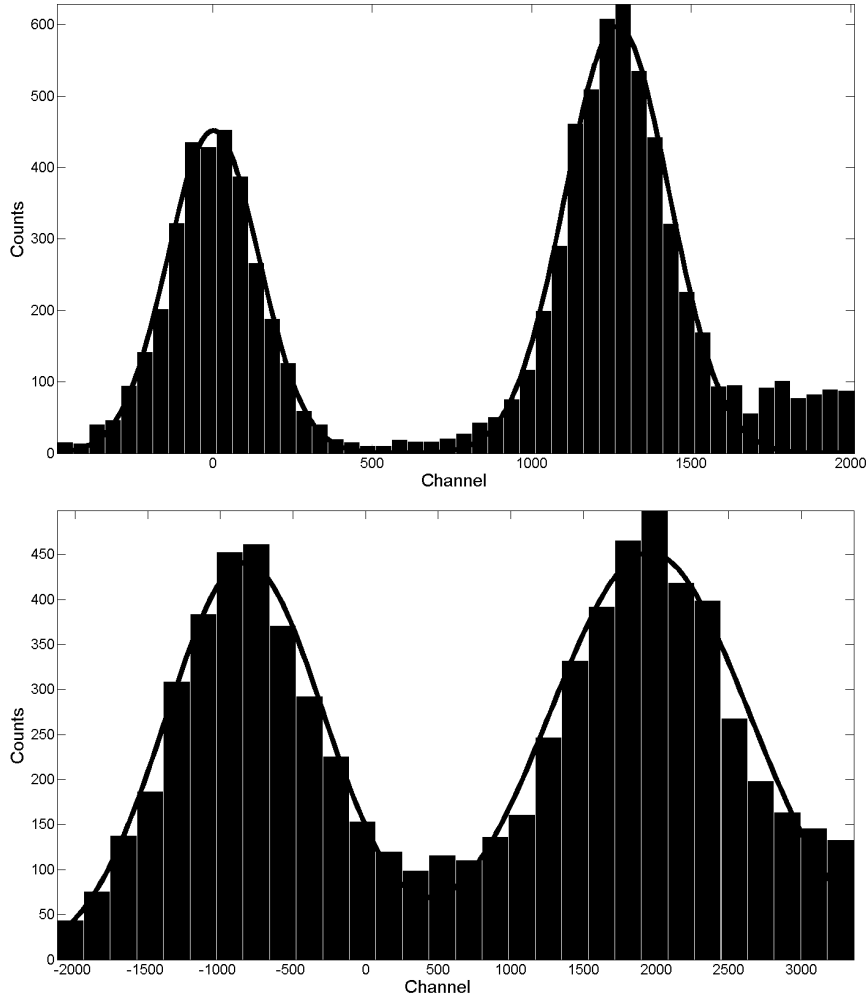
Figure 6.2: Gaussian fit of histogram from a 25C MPPC pixel (top) and a 50C MPPC pixel (bottom). Both are based on 10 000 measurements, and it is clear that the 25C MPPC experience less noise than the 50C MPPC.

Table 6.1: The values presented in figure 6.3 and 6.4. The mean is presented with a standard deviation.

25C	mean	max	min	50C	mean	max	min
Gain	1076 +/- 37	1258	1013	—	2764 +/- 57	2945	2510
1.p.e. Std.	189 +/- 9	226	166	—	720 +/- 25	829	643
1.p.e. Height	488 +/- 39	575	90	—	392 +/- 13	436	306
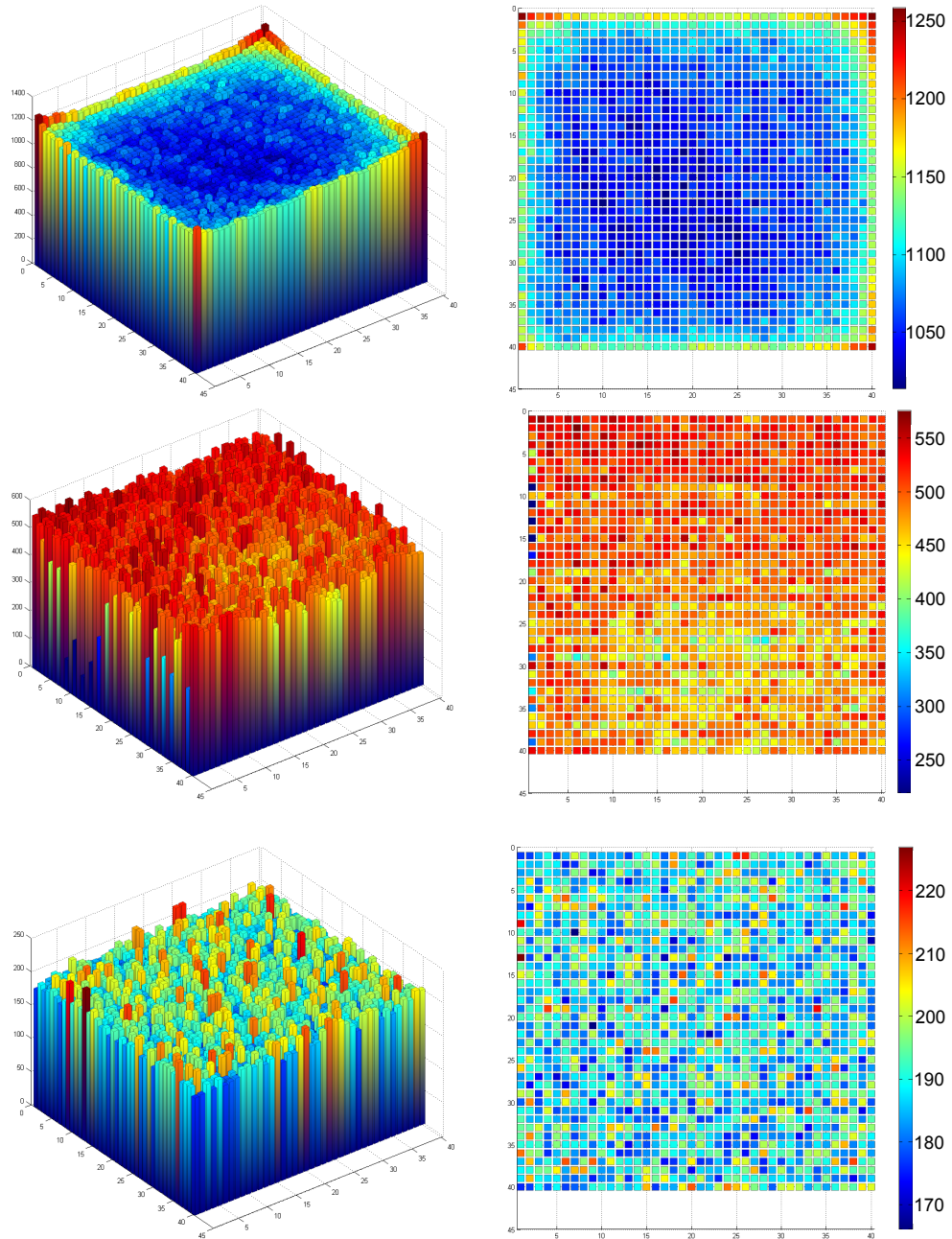
Figure 6.3: 2D histograms from the 25C showing gain (top), 1.p.e. std. (middle) and 1.p.e. curve height (bottom). The mean, maximum and minimum values from the plot are presented in table 6.1 25C.
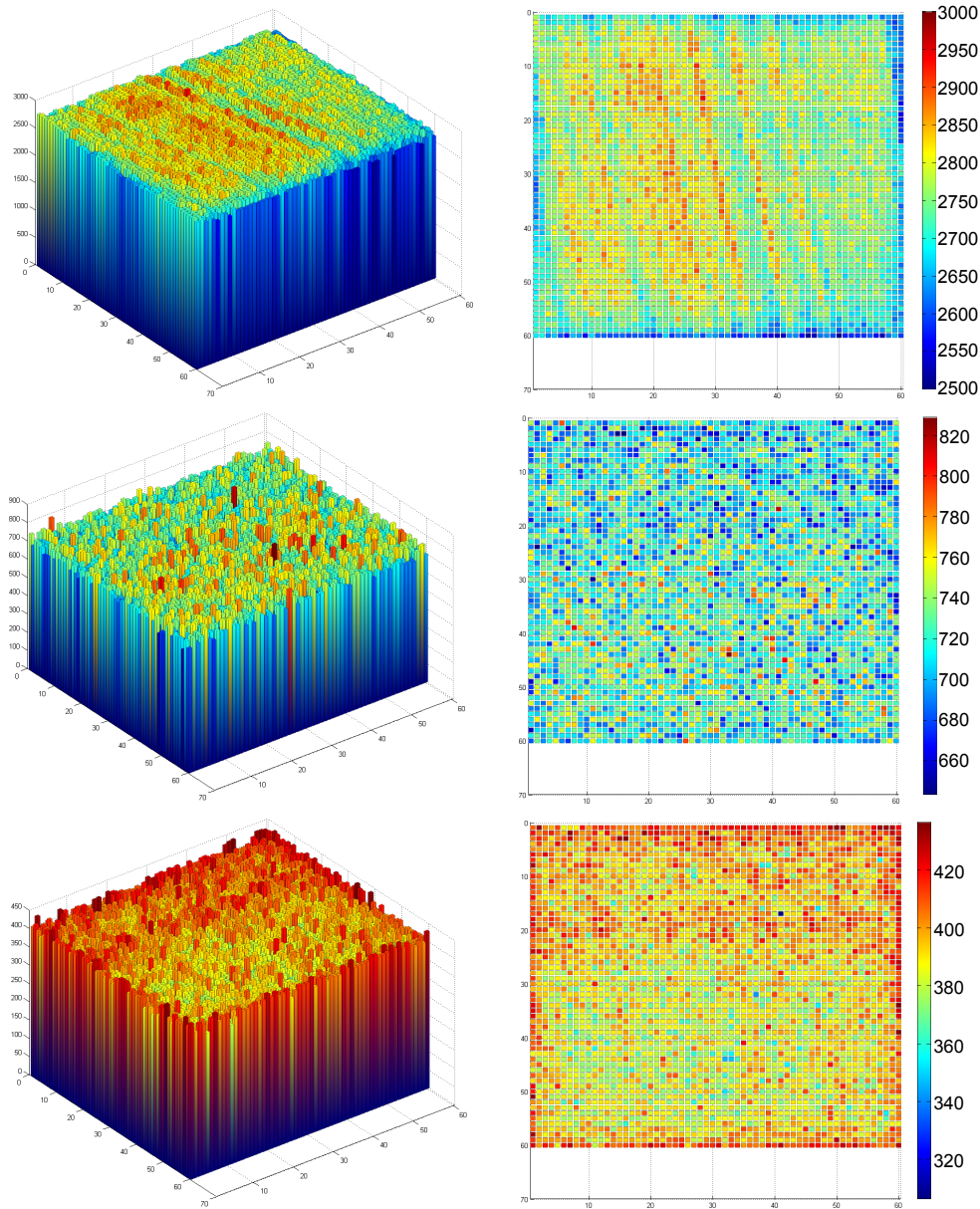
Figure 6.4: 2D histograms from the 50C showing gain (top), 1.p.e. std. (middle) and 1.p.e. curve height (bottom). The mean, maximum and minimum values from the plot are presented in table 6.1 50C.
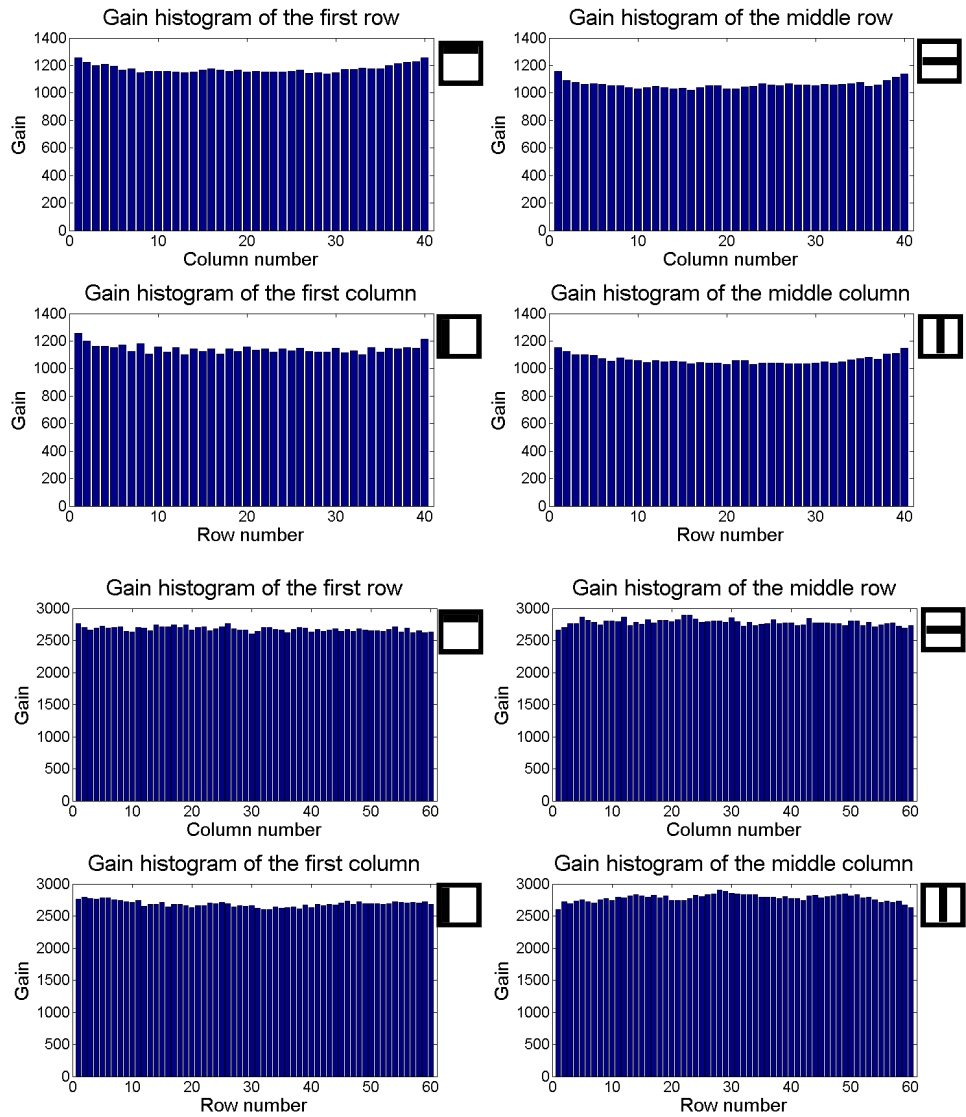
Figure 6.5: Slices of the gain histograms. The top four are from the 25C and the bottom four are from the 50C.
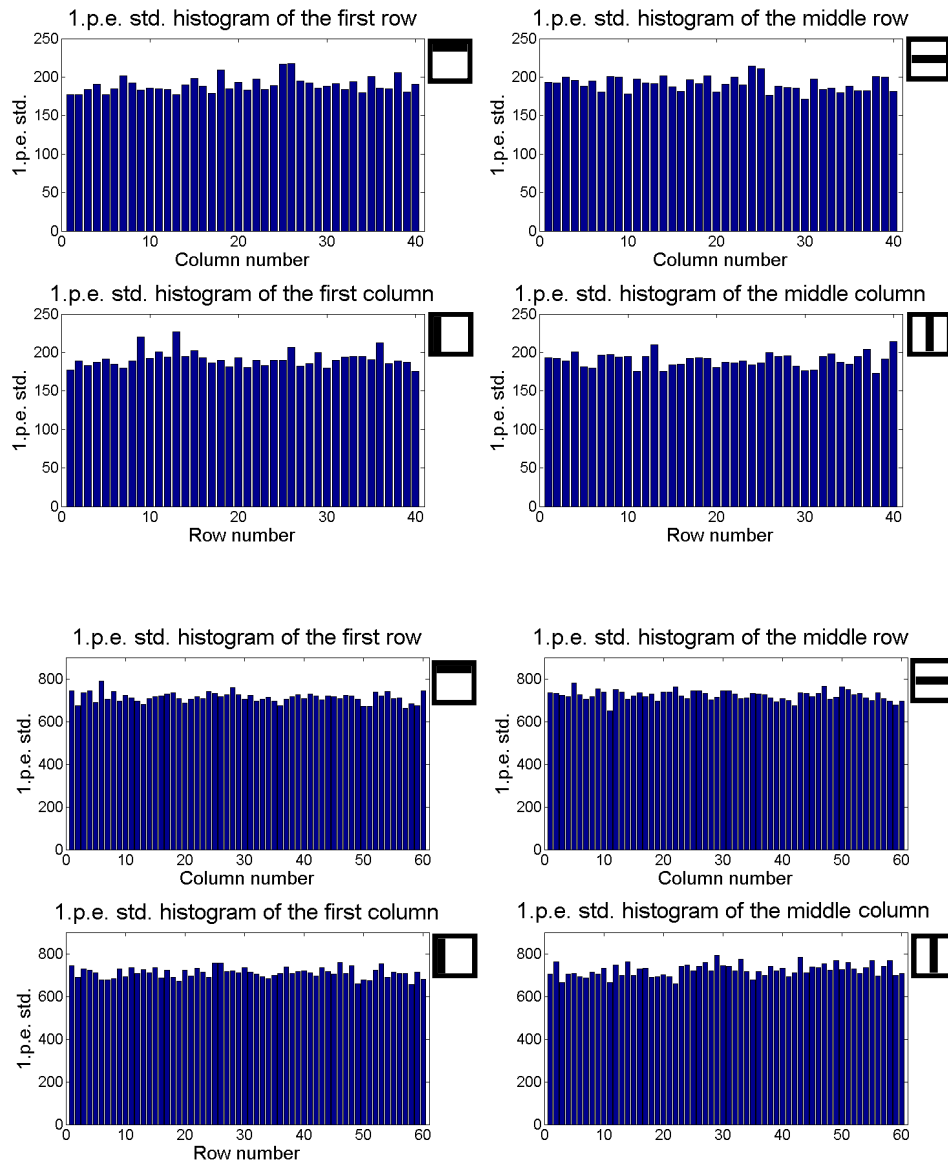
Figure 6.6: Slices of the 1.p.e. std. histograms. The top four are from the 25C and the bottom four are from the 50C.
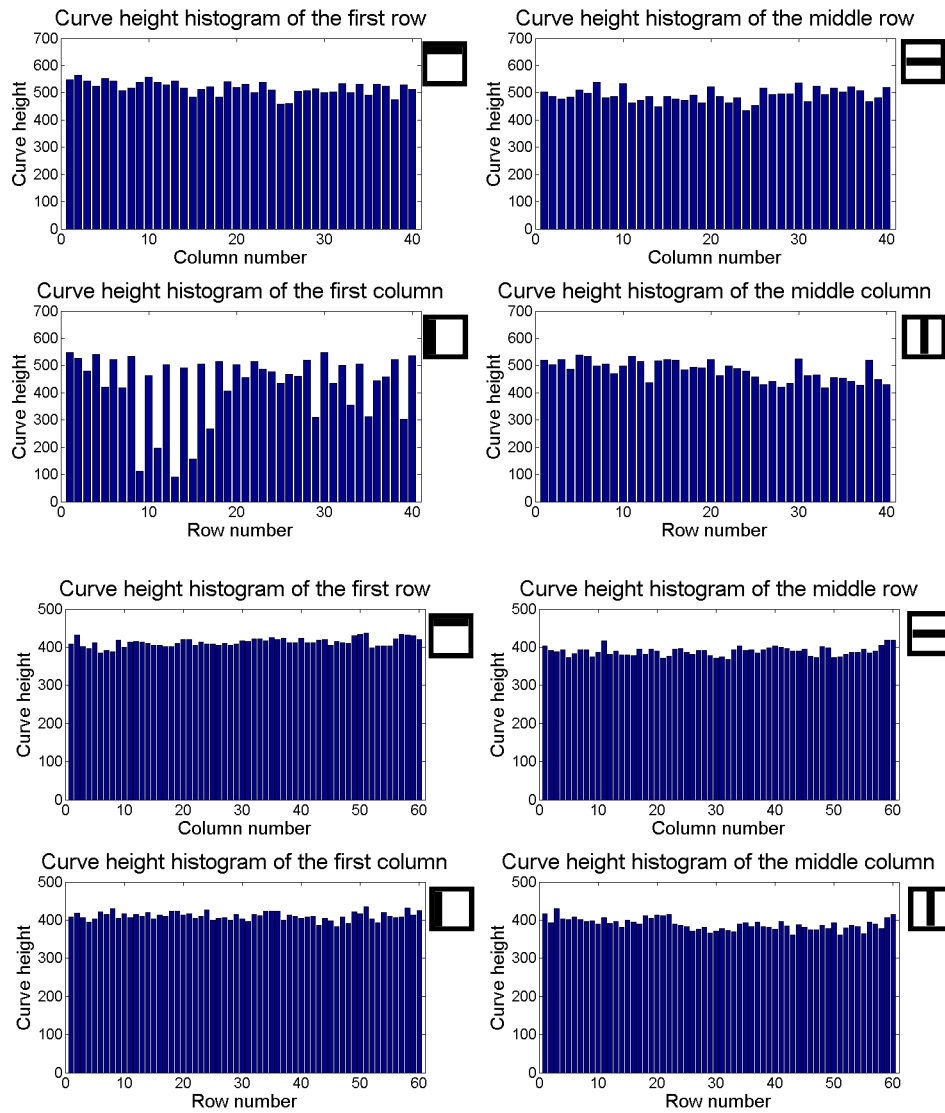
Figure 6.7: Slices of the height histograms. The top four are from the 25C and the bottom four are from the 50C.

Series nr. 1.

Series nr. 2.

Series nr. 3.
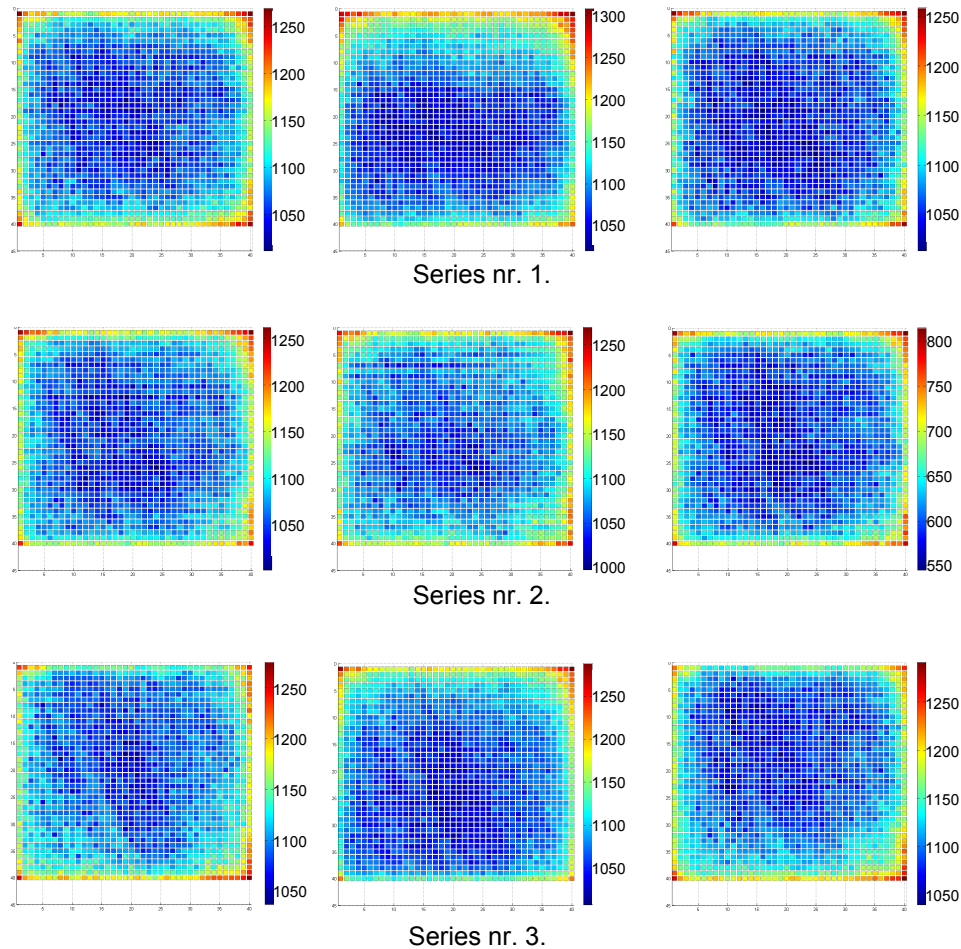
Figure 6.8: The gain plot of the 25C reproducibility measurements.

6.2   Reproducibility

A reproducibility test was done for both the 25C and the 50C. The 25C test involved the disassembly and reassembly of some component. This was only done for the 25C since it demands the most accurate stepping on account of its small pixels.

It is important to notice that color coding of the measurement matrices shown is not the same for all measurements. The color coding from blue to red is based on the minimum to maximum value in the given matrix. This is done in order to show any pattern as clearly as possible.

6.2.1   S10362-11-025C

The 25C reproducibility test was done by taking 3 series of measurements. Each series contain 3 measurements. In between each series the readout
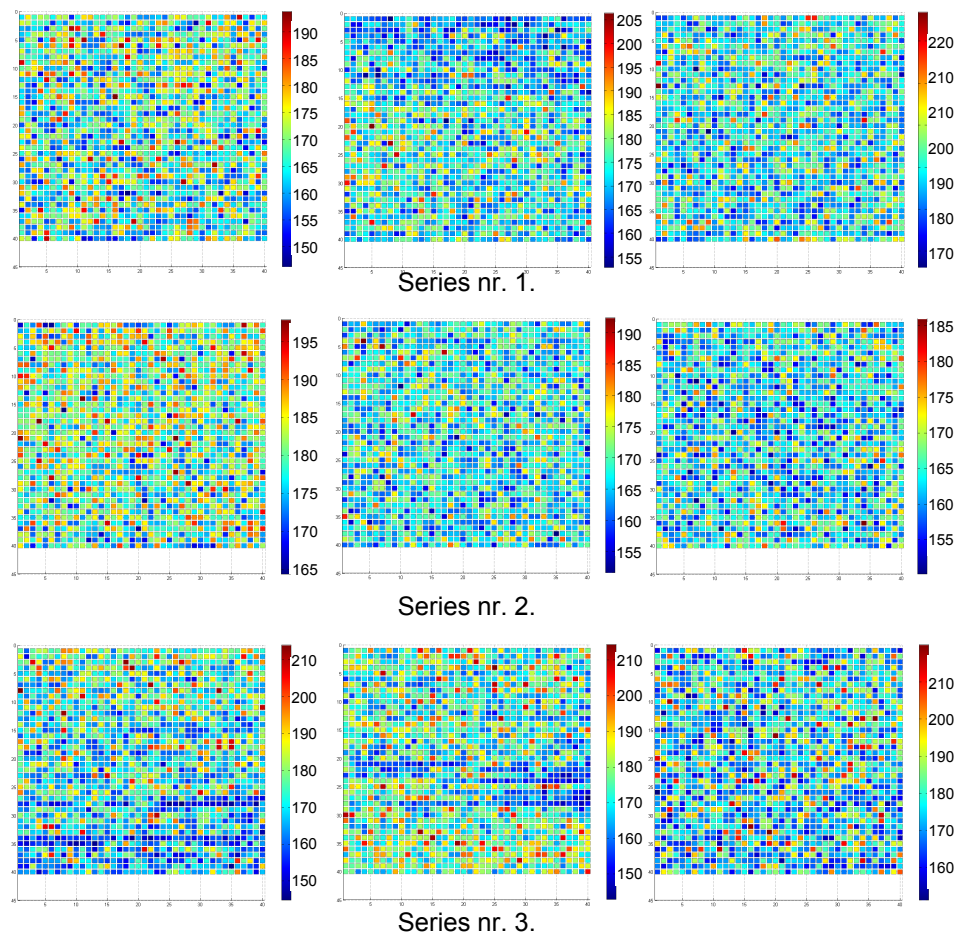
Figure 6.9: The 1.p.e std. plot of the 25C reproducibility measurements.
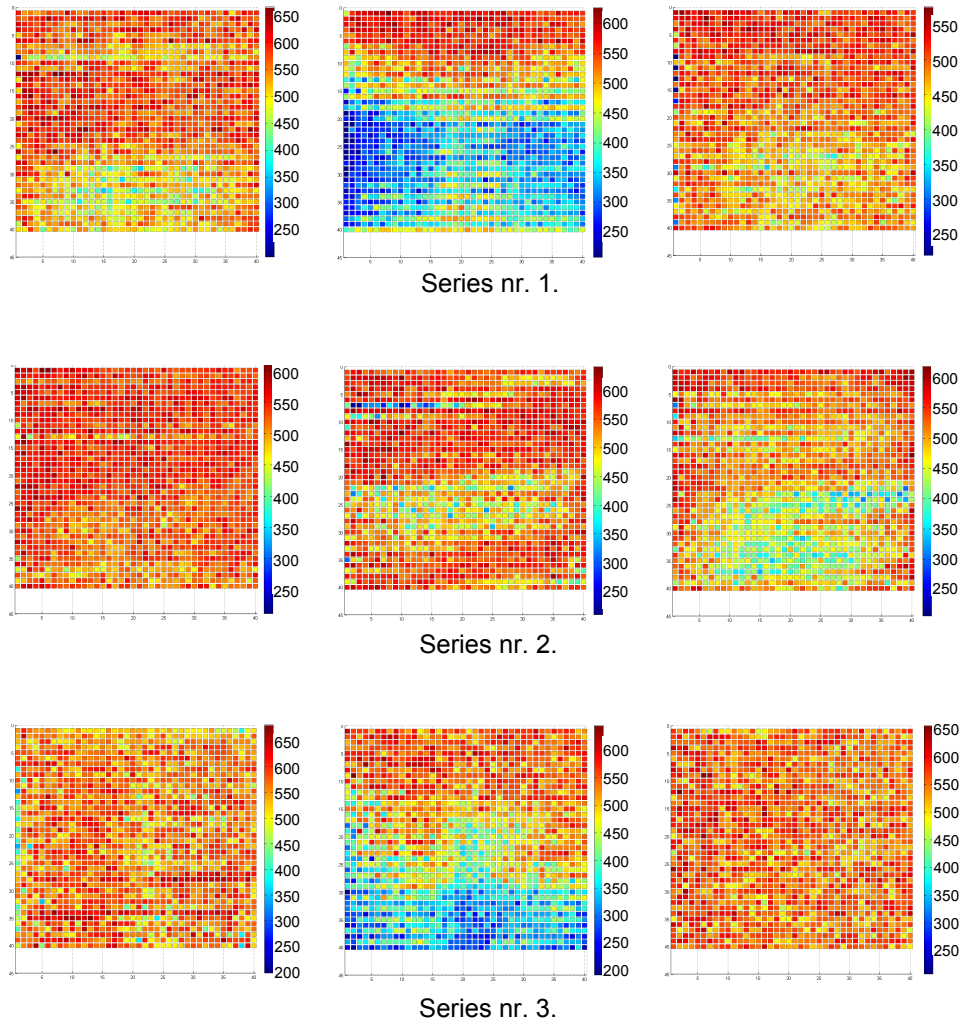
Figure 6.10: The 1.p.e. curve height plot of the 25C reproducibility measurements.

Table 6.2: The mean, maximum and minimum gain from the 25C reproducibility measurements. The mean gain of the 8 measurements was 1090, with a std. of 13. Measurement 3 in series 2, is not calculated into the overall mean since it probably had lower bias voltage than the others.

Series 1	mean gain	max. gain	min. gain
Measurement 1	1086	1269	1011
Measurement 2	1101	1307	1020
Measurement 3	1076	1258	1013
Series 2			
Measurement 1	1077	1261	1001
Measurement 2	1084	1268	997
Measurement 3	618	814	545
Series 3			
Measurement 1	1109	1275	1036
Measurement 2	1081	1287	1006
Measurement 3	1111	1291	1039

Table 6.3: The mean, maximum and minimum 1.p.e. std from the 25C reproducibility measurements. The mean 1.p.e. std. of the 9 measurements was 174, with a std. of 7.

Series 1	Mean 1.p.e. std.	max. 1.p.e. std.	min 1.p.e. std.
Measurement 1	167	193	146
Measurement 2	173	206	152
Measurement 3	189	226	166
Series 2			
Measurement 1	180	197	164
Measurement 2	167	192	151
Measurement 3	163	185	150
Series 3			
Measurement 1	172	214	144
Measurement 2	174	214	142
Measurement 3	177	220	151

Table 6.4: The mean, maximum and minimum 1.p.e. height from the 25C reproducibility measurements. The mean 1.p.e. height of the 9 measurements was 511, with a std. of 45.

Series 1	mean 1.p.e. height	max. 1.p.e. height	min. 1.p.e. height
Measurement 1	549	664	115
Measurement 2	422	626	173
Measurement 3	488	575	90
Series 2			
Measurement 1	534	609	418
Measurement 2	538	641	217
Measurement 3	492	618	301
Series 3			
Measurement 1	561	682	330
Measurement 2	458	643	198
Measurement 3	553	655	433

box was removed from the detector chuck, and the MPPC was removed from the readout box. After the removal they were placed back again. The fibre mount were also disassembled and reassembled in between each measurement series. The series gain, 1.p.e. std. and 1.p.e. curve height are shown in figure 6.8, 6.9 and 6.10 respectively, and their mean, maximum, minimum values are presented in table 6.2, 6.3 and 6.4. The std. of the pedestal peak varied from 148 to 159 across the measurements and its mean was 153.

There is a distinct pattern in the gain measurement which is consistent throughout the reproducibility measurements. The mean, maximum and minimum gain do not fluctuate much between measurements, except for the third measurement in the second series. This measurement shows the same gain pattern as the others, but has considerably lower gain. The most probable reason for this is that the bias voltage has been mistakenly set to low. Temperature can also influence the gain, but it would require an unlikely low temperature throughout the measurement to explain the deviance.

There is no clear pattern in the 1.p.e. height plots. The plots shows that the curve heights sometimes become lower at higher row numbers; lower values in the lower half of the matrices. This is probably because the MPPC has had a small absolute movement in one direction during the measurement making the LED light partly miss the last pixels. After any measurement has finished the program "Find Coordinates.vi" checks how well the LED light hit the MPPC pixels. It often finds that all the pixels has been moved in one direction relative to the LED.

The 1.p.e. std. does not show any distinct pattern. The fluctuations in

Table 6.5: The mean, maximum and minimum gain from the 50C reproducibility measurements. The mean gain of the 6 measurements was 2715, with a std. of 62.

	mean gain	max. gain	min. gain
Measurement 1	2648	2793	2431
Measurement 2	2764	2945	2510
Measurement 3	2658	2834	2481
Measurement 4	2654	2814	2428
Measurement 5	2779	2941	2514
Measurement 6	2787	2950	2543

Table 6.6: The mean, maximum and minimum 1.p.e. std. from the 50C reproducibility measurements. The mean 1.p.e. std. of the 6 measurements was 718, with a std. of 35.

	mean 1.p.e. Std.	max. 1.p.e. std.	min 1.p.e. std.
Measurement 1	666	749	599
Measurement 2	720	829	643
Measurement 3	758	883	668
Measurement 4	757	865	667
Measurement 5	682	813	592
Measurement 6	725	935	629

the 1.p.e. std deviation is low and seems to be random. If there had been done more measurements per pixel the fluctuations might be even lower.

6.2.2   S10362-33-050C

In the reproducibility test of the 50C MPPC the readout box and the fibre mount were not disassembled and reassembled between measurements. It was not considered necessary since the reproducibility measurement of the smaller 25C pixels showed very little difference between series. Six measurements of the 50C MPPC were done. The gain is show in figure 6.11, while the 1.p.e. curve height and std. have been left out since they seem to be random like the 25C. The mean, maximum and minimum of these measurements are shown in table 6.2, 6.6 and 6.7. The std. of the pedestal peak varied from 505 to 561 through the measurements, and its mean was 534. The variation is probably because of temperature differences during the measurements that will affect the dark rate, and possibly the DAQ. Some days have been considerably warmer then others, and the sun shines through the windows of the lab a large portion of the day.

There is a distinct pattern in the gain plots, although not quite as clear as in the 25C. The gain does not fluctuate much within one matrix and not
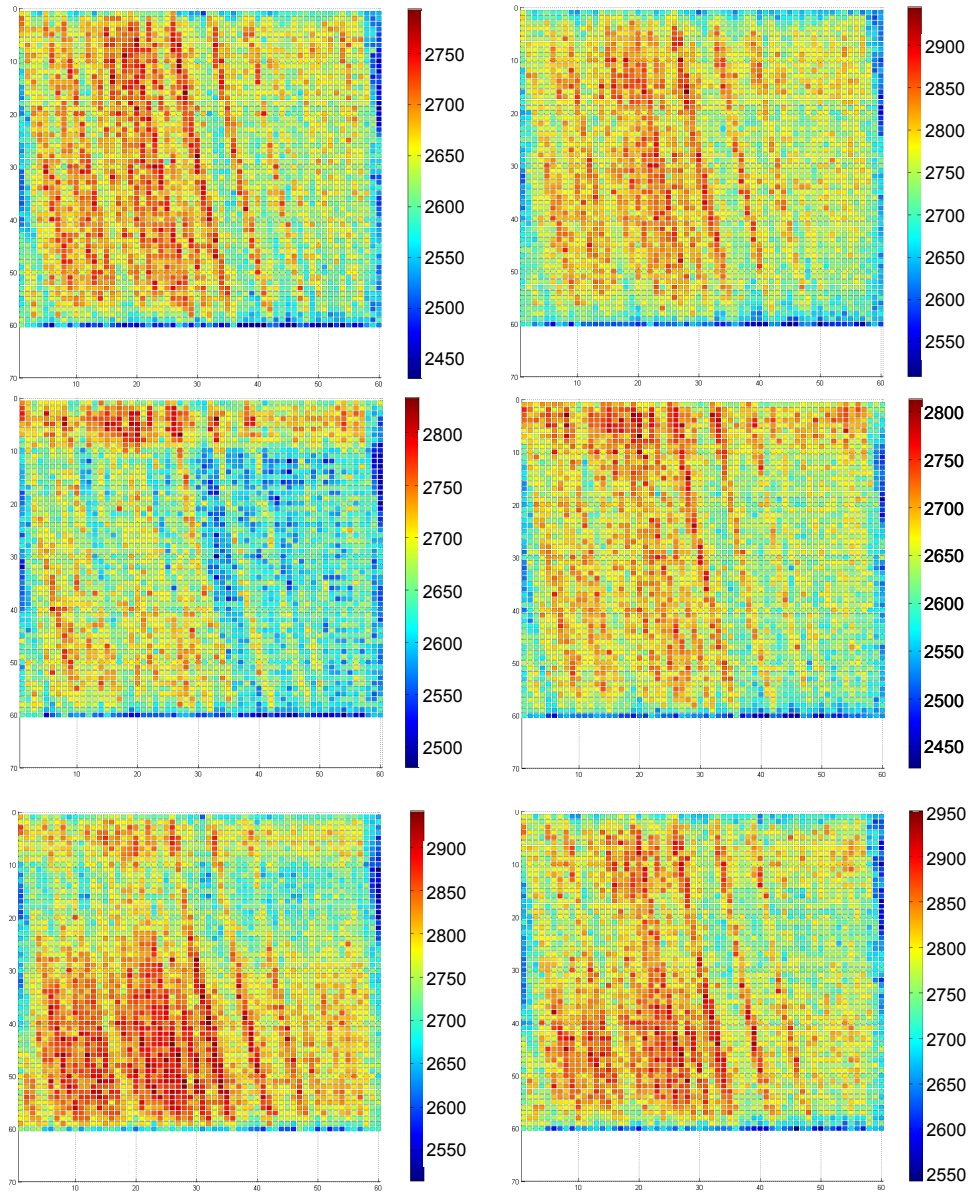
Figure 6.11: The gain plots of the 50C reproducibility measurements.

Table 6.7: The mean, maximum and minimum 1.p.e. curve height from the 50C reproducibility measurements. The mean 1.p.e. height of the 6 measurements was 406, with a std. of 40.

	mean 1.p.e. height	max. 1.p.e. height	min. 1.p.e. height
Measurement 1	461	518	375
Measurement 2	392	436	306
Measurement 3	357	407	312
Measurement 4	368	424	320
Measurement 5	454	514	382
Measurement 6	403	464	325

much between measurements either.

Similar to the 1.p.e curve height in the 25C measurements the curve height of the 50C seems to drop at higher row number. Although the drop is smaller than in the 25C. Curve height difference within one 25C measurement matrix can be as much as 500 counts while it is at most 150 within a 50C measurement matrix. If the explanation behind this height drop is an absolute shift of the MPPC it is consistent that this affect the 50C less than the 25C since it has larger pixels.

The 1.p.e. std. seems to fluctuate randomly, similar to the 25C. The fluctuations seem to be a bit larger in the 50C, but this is expected due to higher dark rate and longer integration window.

6.3 Discussion

The gain of the two detectors is reproducible, more detectors should be tested to see if this is representative for the two different types of detectors.

There are no dead pixels in neither of the MPPCs, and the gain distributions of the 25C MPPC is uniform with the exceptions of the rim of the array. The 50C gain distribution show lines running along the middle. These lines have currently no explanation. Even though the 50C show unexplained pattern the gain does not fluctuate much from pixel to pixel.

Chapter 7

Conclusion and outlook

The goal of this thesis has been to develop a system that can test the uniformity of an pixel array, i.e. the response of single pixels in pixel based detectors. The system has been specifically built to test G-APDs.

The setup was based on a probing station, which was built in 1999 to probe the electrical properties of silicon strip. The probing station has been renamed the XY-table, and most of the original equipment is still present, some with a few minor adjustments.

Most of the time has been used to develop programs that control the motor stages. Due to several problems with the stages there has been less time than planned to characterise the G-APDs. The work has however been successful, and the system does hit the smallest MPPC pixels precisely.

Time has also been used to find a way to trigger the pixels, and the fibre mount was built to send light flashes though the microscope. The diameter of the light flash that hits the pixels has been within satisfactory requirements to target the smallest MPPC pixels without triggering the neighbouring pixels.

The intrinsic performance of the XY-table has been measured through a calibration grid. Both the reproducibility and the actual distance the stages travel when given a position has been tested. This has shown that the stages cannot be trusted to move to a position precisely. Thus, a calibration procedure based on an optical pattern recognition has been developed.

The gain, standard deviation and the curve height from the 1.p.e. peak has been found and plotted. The gain of each pixel in a MPPC are reproducible. The gains standard deviation of each pixel has so far not followed any pattern and seems to be random. The curve height plots have indicated that the LED flash might start to miss the pixels at the end of the measurements. The gain of the 25C pixels are reproducible, and the 50C show some unexplained pattern.

Testing a MPPC detector is very time consuming; about 16 hours to complete one 50C MPPC. It can be done faster with fewer measurements

per pixel, but this would lead to poorer statistics. If a large quantity of G-APDs are going to be tested for building a larger detector system the procedure from this work might be too slow.

The slowest part of the DAQ is at present the ADC. If a faster ADC were provided the measurements could be achieved much faster, or more measurements could be taken to gain better statistics. If the motor stages were replaced with more accurate ones, or somehow repaired, there would be no need for a pattern matching program to find all the coordinates before testing. The program "Place Coordinates.vi" uses about 1 hour to find all the coordinates of the 50C MPPC. If the stages were accurate this would not be needed.

If the MAPD devices from Zecotek are to be tested thoroughly a few changes should be made on the account that they have no visible pixels and a very high density of pixels. Seeing that pattern matching is useless when testing the MAPD the motor stages should be precise. Improved motor stages should then be used. Considering the small size of each MAPD pixel the LED light that triggers the pixels might have to be narrower in order to avoid hitting several pixels at a time.

Bibliography

[1] H. A. Erdal. Characterization of multipixel avalanche photodiodes. Master's thesis, University of Bergen, Institute for physics and technology, 2009.

[2] W.R. Leo. *Techniques for nuclear and particle physics experiments*. Springer-Verlag, 2nd edition, 1982.

[3] C. Amsler and et.al. Passage of particles. `http://pdg.lbl.gov/2009/reviews/rpp2009-rev-passage-particles-matter.pdf`, 2008. [Online; accessed 6-January-2010].

[4] G.F. Knoll. *Radiation Detection and Measurements*. John Wiley & Sons, inc., 3rd edition, 2000.

[5] Konrad Kleinknecht. *Detectors for particle radiation*. Cambridge university press, 2nd edition, 1998.

[6] Helmuth Spieler. *Semiconductor Detector Systems*. Oxford University Press, 1st edition, 2005.

[7] I. Basile-Doelsch, J.D. Meunier, and C. Parron. Another continental pool in the terrestrial silicon cycle. *Nature*, 433(7024):399–402, 2005.

[8] S. Seidel. A review of design considerations for the sensor matrix in semiconductor pixel detectors for tracking in particle physics experiments. *Nuclear Inst. and Methods in Physics Research, A*, 465(2-3):267–296, 2001.

[9] S Takeda, T Takahashi, S. Watanabe, Tajima H., T Tanaka, Nakazawa K, and Y Fukazawa. Double-sided silicon strip detector for x-ray imaging. `http://spie.org/x20060.xml?highlight=x2410&ArticleID=x20060`, 2008. [Online; accessed 6-January-2010].

[10] P. Riedler, G. Anelli, F. Antinori, M. Burns, M. Campbell, M. Caselle, P. Chochula, R. Dinapoli, D. Elia, RA Fini, et al. The ALICE silicon pixel detector. In *Proceedings of the International Workshop on Semiconductor Pixel Detectors for Particles and X-rays (PIXEL2002), Monterey, CA*, 2003.

[11] G. Lindström. Radiation damage in silicon detectors. *Nuclear Inst. and Methods in Physics Research, A*, 512(1-2):30–43, 2003.

[12] M. Moll, E. Fretwurst, and G. Lindstr
”om. Investigation on the improved radiation hardness of silicon detectors with high oxygen concentration. *Nuclear Inst. and Methods in Physics Research, A*, 439(2-3):282–292, 2000.

[13] Y. Unno, H. Kitabayashi, B. Dick, T. Dubbs, A. Grillo, M. Ikeda, Y. Iwata, S. Kashigin, E. Kitayama, W. Kroeger, et al. Evaluation of P-stop Structures in the N-side of N-on-N Silicon Strip Detector. *IEEE Transactions on Nuclear Science*, 45(3):401–405, 1998.

[14] G. Pellegrini, C. Fleta, F. Campabadal, S. Díez, M. Lozano, JM Rafí, and M. Ullán. Technology development of p-type microstrip detectors with radiation hard p-spray isolation. *Nuclear Inst. and Methods in Physics Research, A*, 566(2):360–365, 2006.

[15] MS Alam, A. Ciocio, K. Einsweiler, J. Emes, M. Gilchriese, A. Joshi, S. Kleinfelder, R. Marchesini, F. McCormack, O. Milgrome, et al. The ATLAS silicon pixel sensors. *Nuclear Inst. and Methods in Physics Research, A*, 456(3):217–232, 2001.

[16] Y. Sugimoto. Fine Pixel CCD Option for the ILC Vertex Detector. In *Proceedings of International Linear Collider Workshop*, pages 18–22, 2005.

[17] CJS Damerell. CCD-based vertex detectors. *Nuclear Inst. and Methods in Physics Research, A*, 541(1-2):178–188, 2005.

[18] CJS Damerell. A CCD-based Vertex Detector for TESLA. *LCFI Collaboration: http://hep. ph. liv. ac. uk/˜ green/lcfi/home. html*, 2001.

[19] CERN. Pixels. `http://cms.web.cern.ch/cms/Detector/Tracker/Pixels.html`, 2008. [Online; accessed 6-January-2010].

[20] A. Kluge. The ALICE silicon pixel detector front-end and read-out electronics. *Nuclear Inst. and Methods in Physics Research, A*, 560(1):67–70, 2006.

[21] ALICE Collaboration, F Carminati, P Foka, P Giubellino, A Morsch, G Paic, J-P Revol, K Safarík1, Y Schutz, and U A Wiedemann (editors). ALICE: Physics performance report, Volume 1. *Journal of Physics G: Nuclear and Particle Physics*, 30:1517–1763, 2004.

[22] RH Richter, L. Andricek, P. Fischer, K. Heinzinger, P. Lechner, G. Lutz, I. Peric, M. Reiche, G. Schaller, M. Schnecke, et al. Design and technology of DEPFET pixel sensors for linear collider applications. *Nuclear Inst. and Methods in Physics Research, A*, 511(1-2):250–256, 2003.

[23] H.G. Moser, L. Andricek, X. Chen, A. Frey, G. Lutz, RH Richter, M. Schnecke, A. Raspereza, S. Rummel, L. Feld, et al. DEPFET Active Pixel Sensors. In *Proceedings of the The 16th International Workshop on Vertex detectors. September 23-28, 2007 Lake Placid, NY, USA. Editorial board: Marina Artuso (chairman), Eduardo Docutoesilva, Gianmario Bilei, Daniela Bortoletto, Richard Brenner, Massimo Caccia, David Christian, Paula Collins, Roland Horisberger, Els Koffeman, Bettina Mikulec, Sheldon Stone, Dong Su, Toru Tsuboyama, Stephen Watts., p. 22*, page 22, 2007.

[24] SI Parker, CJ Kenney, and J. Segal. 3D-A proposed new architecture for solid-state radiation detectors. *Nuclear Instruments and Methods in Physics Research-Section A Only*, 395(3):328–343, 1997.

[25] C. Da Via, J. Hasi, C. Kenney, V. Linhart, S. Parker, T. Slavicek, SJ Watts, P. Bem, T. Horazdovsky, and S. Pospisil. Radiation hardness properties of full-3D active edge silicon sensors. *Nuclear Inst. and Methods in Physics Research, A*, 587(2-3):243–249, 2008.

[26] C Da Via, E. Bolle, K. Einsweiler, M. Garcia-Sciveres, J. Hasi, C. Kenney, V Linhart, S. Parker, S Pospisil, O. Rohne, et al. Radiation hardness properties of full-3D active edge silicon sensors. *Nuclear Inst. and Methods in Physics Research, A*, 604(3):505–511, 2009.

[27] T.E. Hansen, A. Kok, T.A. Hansen, N. Lietaer, M. Mielnik, P. Storås, C. Da'Via, J. Hasi, C. Kenney, and S. Parker. First fabrication of full 3D-detectors at SINTEF. *Journal of Instrumentation*, 4:P03010, 2009.

[28] Y. Musienko, S. Reucroft, and J. Swain. A simple model of EG&G reverse reach-through APDs. *Nuclear Inst. and Methods in Physics Research, A*, 442(1-3):179–186, 2000.

[29] D. Renker and E. Lorenz. Advances in solid state photon detectors. *Journal of Instrumentation*, 4:P04004, 2009.

[30] I. WÊGRZECKA, M. WÊGRZECKI, M. Grynglas, J. BAR, A. USZYÑSKI, R. Grodecki, P. Grabiec, S. KRZEMIÑSKI, and T. BUDZYÑSKI. Design and properties of silicon avalanche photodiodes. *Opto-Electronics Review*, 12(1):95–104, 2004.

[31] B.F. Aull, A.H. Loomis, D.J. Young, R.M. Heinrichs, B.J. Felton, P.J. Daniels, and D.J. Landers. Geiger-mode avalanche photodiodes for three-dimensional imaging. *Lincoln Laboratory Journal*, 13(2):335–349, 2002.

[32] V. Andreev, V. Balagura, B. Bobchenko, P. Buzhan, J. Cvach, M. Danilov, E. Devitsin, V. Dodonov, B. Dolgoshein, G. Eigen, et al. A high-granularity scintillator calorimeter readout with silicon pho-

tomultipliers. *Nuclear Inst. and Methods in Physics Research, A*, 540(2-3):368–380, 2005.

[33] K. Yamamoto, K. Yamamura, K. Sato, T. Ota, H. Suzuki, and S. Ohsuka. Development of multi-pixel photon counter (MPPC). *analysis*, 1(2):3, 2006.

[34] P. Buzhan, B. Dolgoshein, A. Ilyin, V. Kantserov, V. Kaplin, A. Karakash, A. Pleshko, E. Popova, S. Smirnov, Y. Volkov, et al. An advanced study of silicon photomultiplier. *ICFA Instrum. Bull*, 23:28–41, 2001.

[35] N. Otte. The silicon photomultiplier–a new device for high energy physics, astroparticle physics, industrial and medical applications. In *Proceedings of the IX International Symposium on Detectors for Particle, Astroparticle and Synchrotron Radiation Experiments, SLAC*, volume 3, 2006.

[36] S. Gomi, H. Hano, T. Iijima, S. Itoh, K. Kawagoe, SH Kim, T. Kubota, T. Maeda, T. Matsumura, Y. Mazuka, et al. Development and study of the multi pixel photon counter. *Nuclear Inst. and Methods in Physics Research, A*, 581(1-2):427–432, 2007.

[37] Z. Sadygov, AF Zerrouk, A. Ariffin, S. Khorev, J. Sasam, V. Zhezher, N. Anphimov, A. Dovlatov, M. Musaev, R. Muxtarov, et al. Performance of new Micro-pixel Avalanche Photodiodes from Zecotek Photonics. *Nuclear Inst. and Methods in Physics Research, A*, 2009.

[38] H.G. Moser. Silicon detector systems in high energy physics. *Progress in Particle and Nuclear Physics*, 63(1):186–237, 2009.

[39] GAM Hurkx, HC de Graaff, WJ Kloosterman, and MPG Knuvers. A new analytical diode model including tunneling and avalanche breakdown. *IEEE Transactions on Electron Devices*, 39(9):2090–2098, 1992.

[40] GAM Hurkx, DBM Klaassen, and MPG Knuvers. A new recombination model for device simulation including tunneling. *IEEE Transactions on Electron Devices*, 39(2):331–338, 1992.

[41] A.L. Lacaita, F. Zappa, S. Bigliardi, and M. Manfredi. On the bremsstrahlung origin of hot-carrier-induced photons in silicon devices. *IEEE Transactions on electron devices*, 40(3):577–582, 1993.

[42] H. Oide, H. Otonoa, S. Yamashitab, T. Yoshiokab, H. Hanoa, and T. Suehiroa. Study of afterpulsing of MPPC with waveform analysis. *PoS(PD07)008*, 2007.

[43] J. G. Johansen. Probing p+ and n+ -type silicon microstrip detectors for the atlas semiconductor tracker. Master's thesis, University of Bergen, Institute for physics and technology, 1999.